Università Politecnica delle Marche
Scuola di Dottorato di Ricerca in Scienze dell'Ingegneria
Corso di Dottorato in Ingegneria Civile, Ambientale, Edile e Architettura

---

Nonlinear Transformation of Waves over a submerged bar

Ph.D. Dissertation of:
Stefania Rocchi

Supervisor:
Prof. Ing. Alessandro Mancinelli

Assistant Supervisors:
Prof. Ing. Sara Corvaro

Ph.D. Course coordinator:
Prof. Ing. Francesco Fatone

XXXIV Cycle

A mio padre e mia madre

Abstract

The growing demand to both utilise and preserve our coastal zones causes the need to better understand the coastal dynamics and to improve the capability to model these processes. In the study of wave propagation towards the shore, it is necessary to take into account the presence of coastal structures that strongly modify the wave field. Along the Italian coast, submerged and emerged breakwaters are the main coastal structures used to protect beaches from erosion processes. Their efficiency in terms of coastal defence is subject to adequate knowledge of the non-linear processes due to the wave-structure interaction. This knowledge is required for the correct design of new structures but it is also important for the adaptation of existing structures that may be necessary especially in view of the future expected climate changes. The 2021 Special Report of IPCC (Masson-Delmotte et al., 2021) shows different scenarios of Sea Level Rise (SLR) depending on the mean increase of global temperatures and on the assumed environmental policies. The sea level could rise up to 1.01cm in 2100 if no climate change mitigation policy will be adopted, while the minimum attended increase is 28cm with the most stringent mitigation scenario. As a consequence, the actual structures could become less effective and they need to be adapted, according to the change in environmental conditions.

The objective of this thesis is to increase the knowledge and the physical insight on the mechanisms of non-linear interaction between waves and coastal structures. A better understanding of the physical processes can be implemented in numerical models to improve their predictive capabilities.

Laboratory experiments have been carried out to study the transformations of both monochromatic and random waves during the propagation over a submerged obstacle. The submerged bar had a longer berm width with respect to those typical of a submerged breakwater in order to analyse, over longer distances, the energy exchange that occurs between the various harmonic components of waves. At first, the monochromatic waves have been studied because they are easier to analyse and they provide quite valuable information about the generation of super-harmonics. Monochromatic waves are useful to simulate narrow-banded spectra, which are typical of sea swell conditions. Their study is also the starting point to better understand the more complex mechanisms related to the propagation of random waves.

The free surface measurements have been elaborated by means of spectral and bispectral analyses and the influence of different wave parameters on the non-linear wave interactions has been evaluated, in particular the effects of the wave period and the wave breaking. It has been observed that the increase in the wave period causes a greater transfer of energy at high frequencies and, in some cases, the secondary harmonic components become prevalent. The wave breaking acts by mainly reducing the energy of the primary component and it involves a redistribution of energy over a wider high-frequency range, with less pronounced peaks at the secondary harmonics.

For breaking waves, more energy is also shifted towards low frequencies due to the mechanism of generation of infragravity waves proposed by Symonds et al. (1982). This mechanism is referred to as the *breakpoint mechanism* and it is attributed to the time-varying displacement of the breakpoint location in presence of wave spectra or wave groups.
The bispectral analysis is used to examine the spatial variation in intensity of the non-linear couplings between harmonic components in a wave field propagating over and beyond the bar. The observed spatial variations of the nonlinearity parameters (such as bicoherence, skewness and asymmetry) indicate strong phase couplings between the primary component and its harmonics over the bar due to the non-linear triad interactions. In the deepening region beyond the bar, a different behaviour for random and monochromatic waves is observed. For random waves the bound harmonics are released and the wave field can still be described as a superposition of statistically independent waves, without memory of the phase locks which existed over the bar. Unlike irregular waves, the harmonic components of monochromatic waves continue to interact in the protected area and the asymmetry parameters vary significantly as a result of the varying phase lags between the freely propagating component waves.
The evolution of the biphase has been found to be consistent with visual observation that waves evolve from a slightly peaked, nearly sinusoidal shape offshore of the structure (with biphase equal to zero) to a shape characterized by a steep front face over the berm of the structure (with biphase equal to $-\pi/2$).
The evolution of the wave spectrum behind submerged obstacles also affects the run-up on the beach. A second experimental campaign has been carried out to evaluate the wave run-up over a 1:20 impermeable slope in presence of the submerged bar. The observed run-up is better correlated to the incident wave characteristics for regular monochromatic waves and to the characteristics of the transmitted spectra for random waves. In fact, for random waves the non-linear interactions induced by the submerged bar also generate long waves that affect the infragravity band swash. This does not happen for regular monochromatic waves where the first harmonic remains the main forcing of the run-up.

La crescente necessità di utilizzare e preservare le aree costiere richiede una più approfondita conoscenza delle dinamiche costiere e una migliore capacità di modellare questi processi. Nello studio della propagazione delle onde verso riva occorre considerare la presenza di eventuali strutture di difesa della costa che modificano fortemente il campo di moto. Lungo le coste italiane, le scogliere sommerse ed emerse rappresentano le principali opere utilizzate per proteggere le spiagge dai processi di erosione. La loro efficacia in termini di difesa costiera è subordinata ad un'adeguata conoscenza dei processi non lineari dovuti all'interazione onda-struttura. Questa conoscenza è necessaria per la corretta progettazione di nuove strutture ma è importante anche per l'adeguamento delle strutture esistenti che potrebbe rendersi necessario soprattutto in vista dei futuri cambiamenti climatici. Il Report 2021 dell'IPCC (Masson-Delmotte et al., 2021) mostra diversi scenari di aumento del livello del mare (SLR) a seconda dell'aumento medio delle temperature del pianeta e delle politiche ambientali adottate dai vari Paesi. Il livello del mare potrebbe salire fino a 1.01cm nel 2100, se non verrà adottata alcuna politica di mitigazione del cambiamento climatico, mentre l'aumento minimo atteso è di 28cm con lo scenario di mitigazione più rigoroso. Di conseguenza, le strutture attuali possono diventare meno efficaci e necessitano di essere adattate, per far fronte alle nuove condizioni meteo-marine. Questa tesi ha l'obiettivo di ap-

profondire la conoscenza dei meccanismi fisici di interazione non lineare tra onde e strutture costiere. Una migliore comprensione dei processi fisici può essere implementata nei modelli numerici al fine di aumentare le loro capacità predittive. A tal fine sono stati condotti esperimenti di laboratorio per studiare la trasformazione sia di onde monocromatiche che di onde random nella propagazione su un ostacolo sommerso. La struttura sommersa in oggetto è stata realizzata con una lunghezza della berma maggiore rispetto a quella tipica di una scogliera sommersa per analizzare, su distanze maggiori, gli scambi di energia tra le varie componenti armoniche del moto ondoso. Sono state dapprima studiate le onde monocromatiche che risultano più semplici da analizzare e forniscono informazioni interessanti sulla generazione delle super-armoniche. Le onde monocromatiche sono utili per studiare il comportamento di spettri a banda stretta, tipici delle condizioni di swell. Il loro studio è anche il punto di partenza per comprendere meglio i meccanismi più complessi che sono alla base della propagazione delle onde irregolari. Le registrazioni della superficie libera sono state elaborate mediante analisi spettrali e bispettrali ed è stata valutata l'influenza di diversi parametri sulle interazioni non lineari delle onde, in particolare gli effetti del periodo ondoso e del frangimento. È stato osservato che l'aumento del periodo d'onda provoca un maggior trasferimento di energia alle alte frequenze e, in alcuni casi, le componenti armoniche secondarie diventano prevalenti. Il frangimento agisce principalmente riducendo l'energia della componente primaria e comporta una ridistribuzione dell'energia alle alte frequenze su un range più ampio, con picchi di energia meno pronunciati. Per le onde frangenti, è stato osservato anche un maggiore trasferimento di energia verso le basse frequenze, a causa del meccanismo di generazione delle onde lunghe proposto da Symonds et al. (1982). Secondo tale meccanismo, noto come *breakpoint mechanism*, la generazione di onde lunghe è dovuta allo spostamento del punto di frangimento in presenza di spettri ondosi o gruppi di onde. L'analisi bispettrale è stata utilizzata per esaminare la variazione spaziale dell'intensità degli accoppiamenti non lineari tra componenti armoniche nel campo d'onda che si propaga sopra e oltre la barra. Le variazioni spaziali dei parametri di non linearità (come la bicoerenza, la skewness e l'asymmetry) indicano forti accoppiamenti di fase tra la componente primaria e le sue armoniche al di sopra della barra a causa delle interazioni non lineari tra le triplette. Con l'aumento della profondità oltre la barra, si osserva un comportamento diverso per onde random e monocromatiche. Per le onde random le armoniche legate vengono rilasciate e il campo d'onda può ancora essere descritto come sovrapposizione di onde statisticamente indipendenti, senza memoria degli accoppiamenti di fase che esistevano sulla barra. A differenza delle onde irregolari, le componenti armoniche delle onde monocromatiche continuano ad interagire nell'area protetta e i parametri di asimmetria variano in modo significativo a causa delle differenze di fase variabili tra le onde componenti che si propagano liberamente. L'evoluzione della bifase è risultata coerente con l'osservazione visiva che le onde evolvono da una forma quasi sinusoidale, con creste leggermente appuntite, al largo della struttura (con bifase uguale a zero) a una forma caratterizzata da fronti ripidi sulla berma della struttura (con bifase uguale a $-\pi/2$).
L'evoluzione spettrale delle onde dietro ostacoli sommersi influisce anche sulla risalita ondosa in corrispondenza della spiaggia. Una seconda campagna sperimentale è stata condotta per valutare il run-up su una pendenza impermeabile 1:20 in presenza della struttura sommersa. Il run-up osservato si correla meglio alle caratteristiche dell'onda incidente per le onde monocromatiche regolari e alle caratteristiche degli spettri trasmessi per le onde irregolari. Infatti, per le onde random le interazioni non lineari indotte dalla barra sommersa generano anche onde lunghe che influenzano la

componente infragravitativa dello swash. Questo non accade per le onde monocromatiche regolari dove la prima armonica rimane la principale forzante del run-up.

Acknowledgements

Le prove sperimentali presentate in questo lavoro di tesi sono state condotte presso il Laboratorio di Idraulica e Costruzioni Marittime dell'Università Politecnica delle Marche.
Nel corso di questi tre anni ho avuto la fortuna di conoscere i Professori, i Ricercatori, i Dottorandi ed il personale tecnico dell'Istituto di Idraulica, che sono diventati amici oltre che colleghi. Mi sembra doveroso ringraziare in particolare alcuni di loro, che mi hanno aiutato a sviluppare e portare a termine questa ricerca.
Vorrei esprimere la mia più sincera gratitudine al mio supervisore, il Professor Alessandro Mancinelli, per le sue straordinarie conoscenze, i suoi consigli, la sua guida e, non per ultimo, per la sua incredibile umanità.
Non riuscirò mai a ringraziare abbastanza il mio secondo supervisore, la Professoressa Sara Corvaro, per aver creduto in me ed essere stata il mio punto di riferimento costante.
Un ringraziamento speciale al Dott. Ing. Francesco Marini per avermi supportato (ma soprattutto sopportato) e per aver dato un fondamentale contribuito a questo lavoro di tesi.
Vorrei ringraziare anche il Professor Carlo Lorenzoni, per il suo prezioso aiuto ed il suo continuo incoraggiamento.
Ringrazio inoltre i revisori, il Professor Mariano Buccino e la Professoressa Renata Archetti, che hanno contribuito con i loro utili consigli a migliorare significativamente la qualità di questa ricerca.
Un ringraziamento anche ai tesisti Luca, Luca e Altin che sono stati un aiuto indispensabile per lo svolgimento delle prove di laboratorio.
Infine vorrei ringraziare la mia famiglia, che mi è stata sempre accanto e mi ha sempre supportato in tutti questi anni di studio, come nella vita.

Contents

List of Symbols

a	wave amplitude
As	wave asymmetry
$B(\omega_1, \omega_2)$	bispectral energy density
b^2	bicoherence
c	wave velocity
C_p	complex Fourier amplitude
C_p^*	complex conjugate amplitude
c_g	wave group velocity
CFL	Courant-Friedrichs-Lewy number
$E(\omega)$	wave spectrum
$e.d.p.$	energy distribution parameter
K_t	transmission coefficient
K_r	reflection coefficient
f	wave frequency
f_n	frequency of the wave component n_i after the *fft*
f_N	Nyquist frequency
g	gravity acceleration
h	water depth at the structure toe
h'	water depth at the structure crest
h_{ef}	effective water depth
H	wave heigth
H_i	incident wave heigth
H_s	significant wave heigth for irregular wave train
$H_{1/3}$	average of the highest 1/3 waves in an irregular wave train
H_{m0}	spectral wave heigth computed from the zeroth-moment of the spectrum, $H_{m0} = 4\sqrt{m_0}$
H_{m0i}	spectral wave heigth computed from the zeroth-moment of the spectrum at station 1
H_{m0t}	spectral wave heigth computed from the zeroth-moment of the spectrum at station 15
k	wave number magnitude
k_n	wave number of the wave component n_i after the *fft*
k_p	wave number corresponding to the peak frequency
$\boldsymbol{k}$	vector wave number
K_s	shoaling coefficient
L	wave length at the structure toe

L'	wave length at the structure crest
L_p	wave length associated with peak spectral period T_p
L_o	deep-water wave length
L_{op}	deep-water wave length associated with peak spectral period T_p
L_{-10t}	wave length associated with the spectral period T_{-10} at station 15
L_{-20t}	wave length associated with the spectral period T_{-20} at station 15
M_F	depth-integrated wave momentum flux across a unit width
m_0	zero order spectral moment, $m_0 = \int_0^\infty E(f)df$
m_{0i}	zero order spectral moment computed at station 1
m_{0t}	zero order spectral moment computed at station 15
$m_{0i1.5}$	zero order spectral moment computed at station 1 for frequencies $f > 1.5f_p$
$m_{0t1.5}$	zero order spectral moment computed at station 15 for frequencies $f > 1.5f_p$
m_n	spectral moment, $m_n = \int_0^\infty f^n E(f)df$
p	structure porosity
r^2	squared correlation
R_u	regular wave run-up
$R_{u2\%}$	2% exceedence run-up
$R(\tau)$	second-order correlation function
R_c	structure freeboard
S	swash height
S_{inc}	swash height in the significant incident band $f > 0.05Hz$
S_{ig}	swash height in the infragravity-band $f < 0.05Hz$
Sk	skewness of the free surface elevation
s_{op}	deep-water wave steepness, $s_{op} = 2\pi H_{m0}/gT_p^2$
t	time
T	wave period
T_m	mean spectral wave period, $T_m = \sqrt{m_0/m_2}$
T_{-10}	spectral wave period, $T_{-10} = m_{-1}/m_0$
T_{-20}	spectral wave period, $T_{-20} = \sqrt{m_{-2}/m_0}$
T_p	wave peak period
U_r	Ursell number
x	flow direction
y	direction transversal to the flow
z	vertical coordinate: zero at s.w.l. and positive upwards
α	beach slope
α_f	beach foreshore slope
β	biphase
δ_k	normalized wave number mismatch
Δ_k	wave number mismatch
ϵ	wave nonlinearity parameter

ϵ'	wave nonlinearity parameter over the structure crest
$\eta(t)$	water surface elevation
λ	friction coefficient
ρ	water density
σ_η^2	variance of the surface elevation
ϕ	phase angle
ϕ_n	phase angle of the wave component n_i after the *fft*
ω	angular frequency
ω_p	peak angular frequency
ξ_o	deep-water Iribarren number, $\xi_o = tan\alpha/\sqrt{H/L_o}$
ξ_{op}	deep-water Iribarren number based on T_p and H_{m0}

List of Figures

List of Tables

Chapter 1

Introduction

As surface gravity waves propagate from deep-water (where $kh >> 1$, with k the wave number and h the water depth) toward the shore, non-linear processes become relevant in the nearshore zone ($kh << 1$). The non-linear processes act by altering the wave profile shape. Symmetric wave profiles and oscillatory velocities in deep waters become asymmetric and skewed when they are close to wave-breaking. The linear wave theory predicts well the refraction and the shoaling of the wave field in intermediate water depth ($kh = \mathcal{O}(1)$). The spectral representation of the wave field, widely used in the design of coastal structures, shows the non-linear transformations during the propagation toward the shore as changes in the initial spectral shape, with energy transfers to both higher and lower frequencies. The transformation of the wave profile and of the wave spectra is mainly due to the energy transfer between harmonic components of the wave field in a process called *non-linear triad interaction* (Phillips, 1960). Two harmonic components with frequencies f_1 e f_2 (for examples close to the peak frequency $f_p \approx f_1 \approx f_2$) transfer energy both to the sum frequency ($f_1 + f_2 = f_3$) and to lower frequencies due to difference interactions ($f_1 - f_2 = f_3$). In deep water ($kh >> 1$) until the limit of intermediate depths ($kh = \mathcal{O}(1)$) the nonlinearities generate *secondary waves* (bound waves) which remain small in amplitude, the interactions among triads of waves do not occur due to the form of the dispersion relation (Phillips, 1960; Hasselmann, 1962) and, if the wave steepness remains small, waves can be described by Stokes-type theory. For Longuet-Higgins and Stewart (1962) the wave components in a wave group can interact with each other through difference interactions to create bound long waves. This is known as the *bound wave mechanism* (BWM). These bound infragravity waves travel with the speed of the wave group and they are recognized to be responsible of the phenomenon of *surfbeat*. Bound IG waves are already generated in deep water, and, although they are small (on the order of 1 cm), they undergo a significant transformation and growth in height when propagating from deep water to the shoreline. Another mechanism for the generation of long waves is proposed by Symonds et al. (1982). It is referred to as the *breakpoint mechanism* (BKM) and it is attributed to the time-varying displacement of the breakpoint location in presence of waves with different heights as for wave spectra or wave groups. In this case a dynamic *set-up* is generated that propagates both offshore and onshore from the breakpoint. Both seaward and shoreward long waves generated by the BKM propagate with their own celerity given by the dispersion relationship and therefore can be considered free. These waves can be reflected by the coast and they could become *edge waves* or they could propagate offshore. A third mechanism

of generation of infragravity waves, proposed by Bertin et al. (2018), consists in the union of waves of the type *bore* and it is associated with amplitude dispersion in the *inner surf zone*. In shallow water depths ($kh << 1$), triad interactions are nearly resonant and the energy transfer process becomes more relevant. The finite amplitude wave models can only be applied when the Ursell number ($U_r = H/(2(k^2h^3))$ where H is the wave height) is small ($U_r = \mathcal{O}(1)$) and, therefore, it is necessary to use wave models based on Boussinesq equations (Peregrine, 1967) in which both the wave nonlinearity (a/h, $a = H/2$) and the dispersion ($(kh)^2$) are small and of the same order. Elgar and Guza (1985b) performed on field experiments in Santa Barbara (California). The authors verified the importance of non-linear phenomena on the shoaling process over a natural beach without bars or submerged obstacles. Narrow band spectra usually generates secondary peaks with respect to the main wave frequency. In broad band spectra, the energy is distributed over a wider frequency range larger than the peak frequency. In addition to the component amplitude evolution, the phases of the frequency components varies with a velocity which is different with respect to the velocity calculated by finite depth linear wave models. Therefore, the variation of the wave shape profile leads to a dispersion in wave amplitude. Waves in deep water depths are characterized by a symmetric profile. At smaller depths, the wave profile becomes steeper with more peaked crests and wider troughs. Such evolution to more asymmetric shapes is also highlighted by the evolution of the skewness of η (free surface elevation). Non-linear Boussinesq models are better able to describe wave propagation with respect to linear models. However, some doubts still remain, especially regarding the generation and the propagation of waves at lower frequencies. In Elgar and Guza (1986) non-linear wave evolution from offshore to the shoreline is studied by means of higher order spectral analysis (e.g. bispectrum). The bicoherence obtained from the water level η increases toward the coast as a consequence of large non-linear interactions between Fourier components. Biphase, skewness and asymmetry with respect to the vertical axis changes substantially with the wave profile evolution that changes from the quasi-sinusoidal offshore shape to the sawtooth shape in breaking conditions and peaked shape after the breaking occurs. Elgar et al. (1997) performed field measurements (Duck 94, North Carolina) to study the evolution of a gravity wave spectrum that propagates over a natural beach profile with sandy bars. Waves that pass over a submerged obstacle, bar or breakwater, are partially reflected and partially transmitted in the inshore side. The transmission process is very complicated because it depends both from the obstacle shape parameters (slopes, submergence, width) and from the hydrodynamic characteristics of the wave trains (wave height, period, frequency distribution). Non-linear processes are activated in the shoaling area at the outer slope of the bar. They are responsible for the behaviour of the transmitted waves that show a space and time varying free surface profile. Linear wave models usually neglect, or parametrize with empirical equations, non-linear terms, reflection and dissipation contribution from the wave action balance equations. Non-linear interactions causes energy transfers among triads with frequencies f_1, f_2 and f_3 with $f_1 \pm f_2 = f_3$. For this evaluations, higher order statistical tools are needed, such as bispectral analysis. For intense wave sea stats, both the breaking and non-linear interactions influence the spectral evolution of waves over a bar/obstacle. It is still not clear the role of breaking in such process. According to Mase and Kirby (1993) the dissipation, normalized by the spectral density, increases with the frequency. On the contrary, Beji and Battjes (1993, 1994) studied by both laboratory experiments and numerical simulations, the wave propagation process over a submerged bar. They found that relative dissipation does not

depend on the frequency. The differences between the Boussinesq model and the observations are given by the breaking dissipation that was not correctly reproduced in the numerical model. With regards to non-linear interactions, the authors observed a large energy transfers from the peak frequency to its first harmonics in the case of very narrow band spectra (swell) during the wave evolution from offshore to the bar. In particular, over the horizontal crest of the bar the peak frequency and its superharmonics are characterized by similar energies. As a consequence, over the bar twice the wave crests are observed, in agreement also with Byrne (1969). Such drift of energy to higher frequency is not so evident when the wave propagates over a monotonic beach profile. Elgar et al. (1997) studied the spectral evolution over a natural barred beach profile. They obtained that the skewness and asymmetry increases from the offshore value of 0 (symmetric waves) to values of about 0.5 over the bar. In the horizontal part the skewness keeps constant while asymmetry goes to 0. The employed Boussinesq models describe in a fairly good manner the spectral evolution but they under estimate wave breaking over the bar crests and the reflection. For more intense sea state conditions ($H_s > 1m$) wave reflection can be neglected and the propagation only depends on dissipation and non-linear interactions. Close to the crest, the ratio $D(f)/E(f)$ ($D(f)$ is the dissipation and $E(f)$ is the spectral density energy) increases proportionally with the frequency according to f^2. Local variations of spectral levels due to non-linear interactions are of the same order of those given by the dissipation process. Non-linear energy transfers are able to double the wave crests number close to the shoreline as it also happens to a narrow band spectrum that propagates over a constant slope profile. Low frequency and low energy sea states are reflected by the beach and they give a partially stationary wave field without leading to resonance processes. Goda et al. (1999) studied the effects of an abrupt bathymetry change, given by a submerged reef or a horizontal shelf with a steep offshore slope, on the propagation of third order Stokes' waves. The authors find out that the shape of the transmitted waves becomes complicated, the crests are given by multiple peaks and the η varies in space and time. Secondary, tertiary and higher order harmonics are hence generated over the obstacles and their amplitudes are not constant.
In the present thesis, the sea wave propagation over a submerged obstacle has been studied by means of experimental tests performed in the wave flume of the Laboratorio di Idraulica e Costruzioni Marittime of DICEA Department of Università Politecnica delle Marche and by means of numerical analysis performed with the XBeach solver. The submerged obstacle is similar in size to the experiments of Beji and Battjes (1993) and Liberatore and Petti (1992). Here, a wide range of regular and random wave characteristics and two different values of submergence are studied. The main aim of this study is to better understand spectral evolution due to non-linear interaction by means of bispectral analysis. The energy transfer of the incident spectrum to higher frequencies and the presence of long waves (free and bound) strongly modify the free surface evolution in the inner zone and, therefore, the run-up process on the protected beach. Run-up measurements over the beach highlight some aspects of the phenomenon which is of great relevance for engineering purposes because it influences the beach flooding for extreme wave conditions or sea level rise. Several experimental campaigns have been carried out over natural beaches without sandbars. The main empirical formulas (Stockdon et al., 2006; Vousdoukas et al., 2011) use the Iribarren parameter ($\xi_0 = \tan(\beta)/(H_0/L_0)^{0.5}$ where $\tan(\beta)$ is the slope of the beach in the final part of the swash zone, H_0 and L_0 are the offshore wave height and wave length) and two asymptotic values are found for $\xi_0 < 0.3$ (saturated beaches) and $\xi_0 > 1.25$ (reflective beaches). Such approach is not easy to be applied for barred beaches or

beaches protected by breakwaters that highly influence both H_0 and L_0. A deeper understanding of the hydrodynamics induced by the obstacle is hence necessary. In the experimental tests of the present thesis, the effect of spectral period variation and the influence of infragravity waves on the run-up is evaluated. In addition, the role of breaking on wave propagation is further studied to clarify some aspects that were not highlighted in the previous experimental works.

Chapter 2

Review and Theory

The experimental campaign of this study allowed to shed light to different phenomena that act during the wave propagation towards the shore. First of all, the non-linear transformations of wave profiles and spectra over a submerged bar were studied. The evolution of waves over an obstacle gives rise to the generation of higher and lower harmonic components of the waves. Since a spectral analysis is not sufficient to tell if these frequency components are bound or free, the application of a higher order spectrum (bispectrum) is more suitable to examine wave non-linearity. Finally, after the wave propagated behind the bar, the effect of the bar on the wave run-up was also studied. Each of these individual phenomena are widely studied in the literature, so in this chapter a brief overview on the main theories and on the state of the art about these topics is reported. The arrangement of this chapter is as follows. In Section 2.1 the harmonic generation in waves propagating over submerged obstacles is described. Section 2.2 describes the application of the bispectral analysis to investigate some aspects of the non-linear dynamics of waves propagating in shallow water. In Section 2.3 the main studies and formulations for the evaluation of the wave run-up are reported.

2.1 Harmonic generation past a submerged bar

In this chapter, the main topic of this research is addressed, namely the interaction between waves and submerged bars. It is known that submerged structures, in addition of reducing the incident wave energy, strongly modify the transmitted wave field, both in breaking and non-breaking conditions, leading to the generation of secondary waves that interfere, in the protected area, with the primary wave component.

2.1.1 Literature review

The generation of higher and lower frequency waves, due to non-linearity in a wave field propagating over a shallow region, has long been known both experimentally and theoretically.

From a theoretical point of view the problem was first addressed by Massel (1983) and Goda et al. (1999), who studied the propagation of Stokes waves over a submerged rectangular and impermeable step with second order and third order theories, respectively. They addressed the topic as an extension of the propagation problem

in which the wave field presents strong discontinuities, represented in this case by a sudden variation in the bottom topography due to the presence of the bar. By following a perturbative approach to solve the system of equations of motion, they proposed solutions of fundamental importance to understand the complex mechanism of wave-structure interaction from a qualitative point of view. In the presence of the submerged obstacle, the wave motion is partly reflected and partly transmitted behind the obstacle. The presence of the discontinuity in the wave field due to the submerged bar causes the decomposition of the incident primary wave (with frequency f) into different harmonics of multiple frequencies with respect to the main one. A part of these super-harmonics is linked to the fundamental (*bound waves*) while the other part travels as free oscillations with frequency $2f$ and celerity independent from the previous ones (*free waves*). In the offshore area (Region 1 of Figure 2.1) the wave field results from the superimposition of the incident wave and the reflected wave. Both waves have first order components and, depending on the relative depth, bounded second order components. The reflected one will have a free component of the second order. Above the crest of the structure (Region 2), the wave motion will result from the superposition of transmitted waves, with first and higher order harmonic components, the latter ones are both bound and free. Behind the barrier (Region 3), there will be a transmitted wave motion with higher order harmonics of the free type and of the bound type, where the latter ones are more or less large depending on the relative depth.

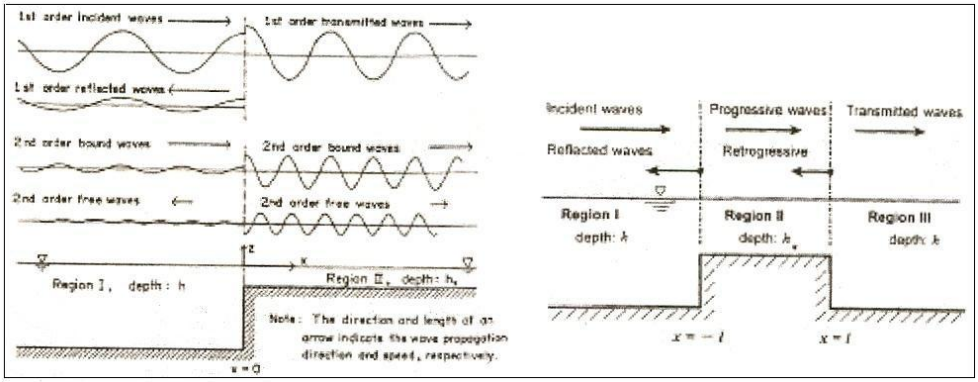

Figure 2.1: Sketch of the spatial domain and of the harmonic components of waves for the cases of an infinite step and a finite one. Adapted from Goda et al. (1999).

The solution proposed by Goda et al. (1999) is developed to the third order of approximation and it includes also the effect of the third order due to the non-linear interaction between the primary wave and the free harmonic of the second order. The interaction between the two free harmonics (f and $2f$) gives rise to two further interference waves of the third order with frequency equal, respectively, to the difference (f) and the sum ($3f$) of the two frequencies of the free harmonics. The mechanism of the interaction between triplets (known as triad interaction) was first addressed by Phillips (1960). More details about this mechanism are described in Section 2.1.2. It should be remembered that the free waves of the second order travel with lower celerity than the Stokes wave of the second order; this fact produces a spatial variation of the wave profile giving rise to a non-permanent wave field. Furthermore, the interaction between bound waves and free waves generates a spatial oscillation of the

total harmonic with frequency $2f$.

The problem of frequency generation over a submerged obstacle was also studied experimentally by many researchers. The experiments of Beji and Battjes (1993) and Liberatore and Petti (1992) are particularly significant for the study objected of this thesis. They both examined the transformation of waves passing over a submerged trapezoidal bar with offshore slope 1:20, inshore slope 1:10 and top width of 2m, built on a horizontal bottom. Liberatore and Petti (1992) studied the propagation of random waves for two offshore water depths of 40cm and 50cm, so water depth above the bar was 10cm and 20cm respectively. Waves were measured at thirteen measuring stations in the flume using eight parallel wire resistance wave gauges in two shifts (Figure 2.2).

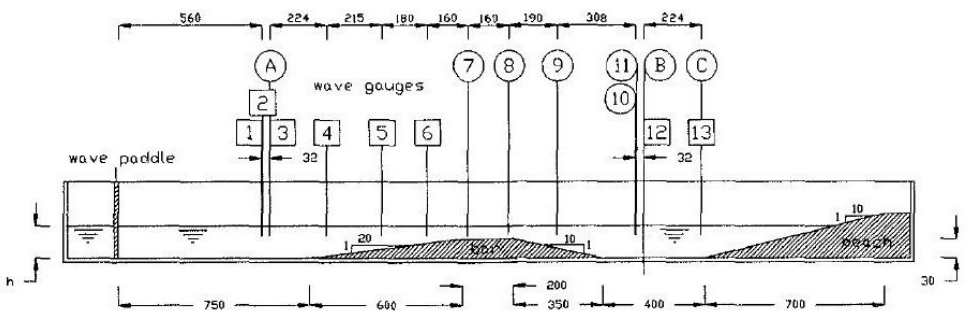

Figure 2.2: Experimental set-up and location of wave gauges for the experimental investigation of Liberatore and Petti (1992). Adapted from Liberatore and Petti (1992).

In Figure 2.2 squared numbers correspond to group 1 (8 gauges, first shift) and circled numbers and letters to group 2 (second shift). For each water depth, three different random wave trains were generated. Both short and long waves were analysed by filtering the signal and, considering the frequencies respectively higher and lower than $0.5f_p$ (where f_p is the peak frequency of the wave spectra), reconstructing the time domain signal using the Inverse Fourier Transforms. This allowed in particular investigation of transformations of long waves passing over the bar. A second order analytical method was also applied to the data in order to calculate first and second-order contributions from measured spectra. Beji and Battjes (1993) found that the dominant physical mechanism was the amplification of bound harmonics in the shoaling region and their release in the deeper region, resulting in the decomposition of the wave field. They found that the phenomenon of harmonic decoupling, which takes place as the waves propagate in the deepening water, resulting from the de-shoaling, plays a major role in the wave decomposition and thus determining the final spectral shape. They also concluded that the generation of high frequency energy and its transfer among nearly harmonic wave components, due to the non-linear interactions taking place during the passage over the bar, was hardly influenced by wave breaking which acts as a secondary effect by simply reducing the wave energy spectrum through energy dissipation. The practical implication of this observation was the apparent possibility of combining a weakly non-linear non-dissipative model, such as a Boussinesq model, to simulate the harmonics generation and release in

breaking waves with a semi-empirical model for the dissipation of the total energy due to breaking. The feasibility of Boussinesq modelling for the non-breaking wave condition was demonstrated by Beji and Battjes (1994).
Grue (1992) investigated the characteristics of the wave field propagating over a submerged circular cylinder and a rectangular shelf, both experimentally and theoretically. He tried to describe the generation of super-harmonics in detail and he proposed a non-linear method to separate the harmonic components of the transmitted wave field. The graphs in Figure 2.3 show the results of the tests performed in the presence of the rectangular barrier with two levels of submergence and for two slightly different periods of the fundamental harmonic. Grue (1992) observed that the generation of the higher-harmonic waves was more powerful for the rectangular obstacle than for the cylinder and a pronounced third-harmonic wave was also present. From both graphs it is evident that the generation of the higher-harmonic waves at the lee side of the obstacle becomes more and more powerful with increasing incoming wave amplitude, up to the occurrence of breaking at the obstacle. At the breaking limit the amplitudes of the second and third-harmonic waves attain maximum values compared to the incoming wave amplitude and, in some cases, they are found to be of the same order of magnitude of the first-harmonic transmitted waves. For the lower submergence (R_c=3.75cm, left panel) Grue (1992) found that the second and third-harmonic wave amplitudes are about 60% of the incoming wave amplitude in the vicinity of the spilling limit.

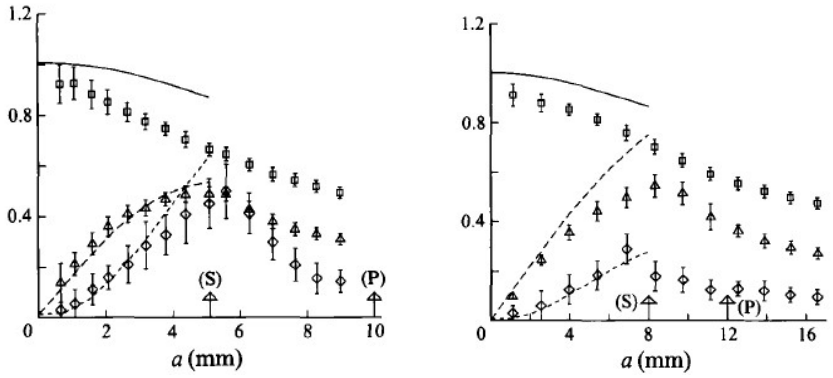

Figure 2.3: First ($a_{FT}^{(1)}$), second ($a_{FT}^{(2)}$) and third ($a_{FT}^{(3)}$) harmonic free wave amplitudes at the lee side of the rectangular shelf with respect to the incoming amplitude a. R_c=-3.75cm and T=1.05s (left panel); R_c=-5.0cm and T=0.952s (right panel). ($\Box$) $a_{FT}^{(1)}/a$; ($\triangle$) $a_{FT}^{(2)}/a$; ($\diamond$) $a_{FT}^{(3)}/a$. The arrows denote respectively spilling (S) and plunging (P) limits. Adapted from Grue (1992).

The effect due to the permeability of a submerged structure on the process of generation of super-harmonics was investigated in laboratory by Losada et al. (1997). The authors carried out experiments in a wave flume to study the difference between harmonic evolution of monochromatic waves as they propagate over a submerged impermeable or porous step under non-breaking conditions. All breakwaters had similar dimensions with a length of 0.80m, height 0.385m and width 1.0m. A constant water depth, h=0.475m, was kept in the flume for all tests so the water depth reduced over the obstacle to 9.0cm. Three models were tested; the first was an impermeable ply-

wood structure sealed to the bottom of the flume, while the two permeable structures were formed using an external structure of steel wires filled with permeable materials of varying sizes. The least permeable structure (*fine permeable*) had a porosity of p=0.521 and was made by gravel with D_{50}=2.09cm, the more permeable structure (*coarse permeable*) was constructed of concrete blocks of 30x30x30mm and it had a porosity of p=0.62. Seven resistance-wire wave gauges were used in the testing. The gauges were positioned in two separate ways: firstly, four stationary gauges were placed at specified positions along the flume and the reflection and transmission coefficient were calculated from the data gathered by these gauges (R/T runs). The other three gauges were positioned on a moving cart and they were used to record the water surface profiles at varying positions along the flume (MC runs). This second set of data allowed to examine the growth of harmonics above each structure. Figure 2.4 shows the reflection (K_r) and transmission (K_t) coefficients for the three structures as a function of the relative water depth kh (k is the wave number).

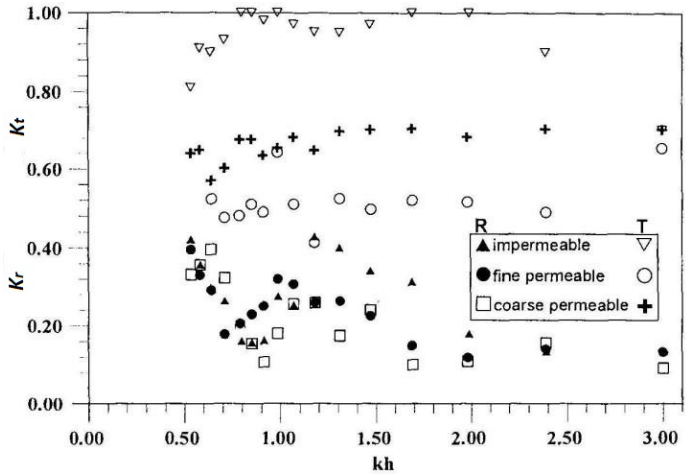

Figure 2.4: Reflection (K_r) and transmission (K_t) coefficients measured by Losada et al. (1997). Adapted from Losada et al. (1997).

The reflection from the structures was determined by applying both the Mansard and Funke (1980) and the Goda and Suzuki (1976) algorithms to the records of the three upwave gauges. From the figure it is evident that the reflection is maximum for the impermeable step and it decreases slightly with increasing porosity. Maximum transmission is also achieved for the impermeable case while, for the porous structures, transmission increases with increasing porosity. For a given material and geometry, transmission is little affected by the relative depth. The moving cart runs were carried out to examine the generation of harmonics when a wave train propagates over structures with different porosity. For each run the cart was moved giving a total of eighteen measuring points, with a spacing of 8cm above the step and a spacing of 24cm downwave of it. The generation and growth of harmonics over the structure and their progression leewards were obtained by analysing all the gauge records for all the moving cart positions, both in the time and in the frequency domains. Figure 2.5 presents time series plots and amplitude spectra for some gauge locations for the case with wave height H=4.29cm and wave period T=1.8s for the impermeable structure. The positions of Figure 2.5 are relative to the offshore edge of the structure that is

considered to be located at x=0m. Figure 2.6 shows the same results for the coarse permeable structure.

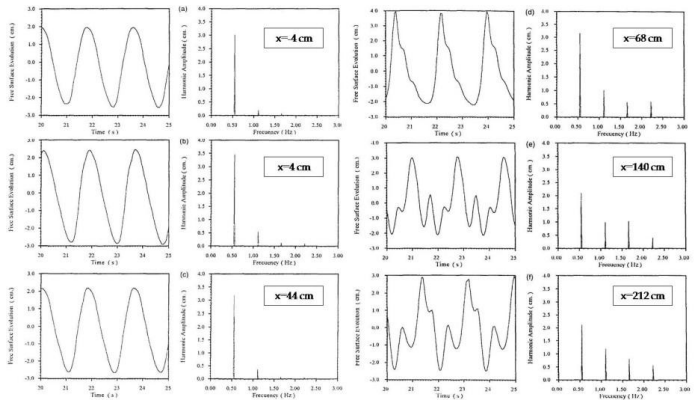

Figure 2.5: Evolution of waveform and corresponding amplitudes at different positions along the flume for the impermeable structure. Adapted from Losada et al. (1997).

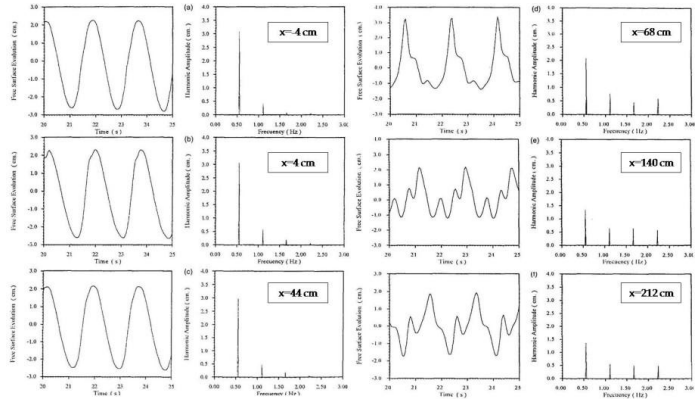

Figure 2.6: Evolution of waveform and corresponding amplitudes at different positions along the flume for the coarse permeable structure. Adapted from Losada et al. (1997).

The incident wave upstream of the step propagates at a single frequency. As progression onto the step is observed, a strongly non-linear waveform develops, with a transference of energy to the higher harmonics. In the case of the impermeable structure, where there are no dissipative effects due to friction with the porous material, the varying harmonic modes are observed to have larger amplitudes than the case with the permeable structures, where dissipation occurs. This includes a considerable growth of the first harmonic over the first portion of the structure, which is in turn transferred to the higher frequency components as the wave continues over the step. For the permeable cases (Figure 2.6), the evolution of the wave profile is similar but there is a continuous loss of energy carried at the first harmonic, unlike what happens for the impermeable structure. These trends can be better observed from Figures 2.7 and 2.8, where the spatial evolution of the amplitudes of the first four harmonics are plotted for the impermeable and the coarse permeable structures, respectively.

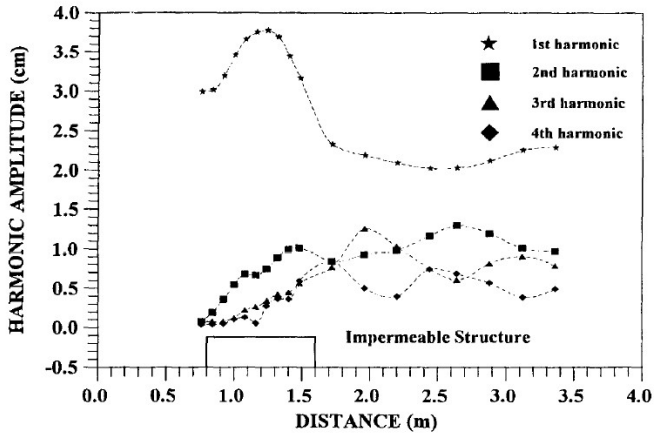

Figure 2.7: Spatial evolution of amplitude of the first four harmonics for the impermeable structure. Adapted from Losada et al. (1997).

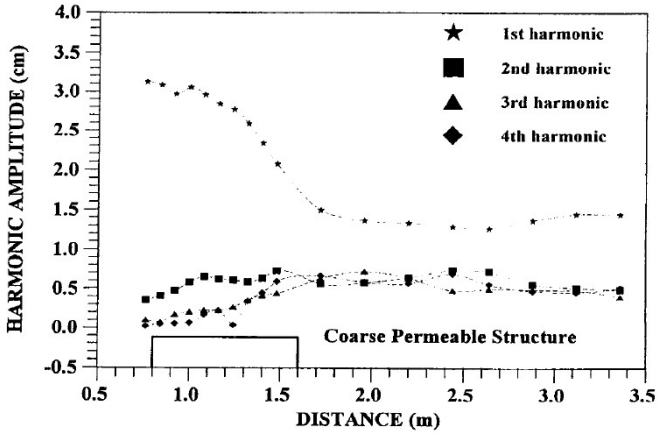

Figure 2.8: Spatial evolution of amplitude of the first four harmonics for the coarse permeable structure. Adapted from Losada et al. (1997).

The permeability of the structure reduces the amplitude of all the harmonic modes considerably. However, this effect is greater on the energy transmitted at the first and the second harmonic amplitudes than at the higher harmonics. An examination of the harmonics leeward of the structure indicates that the permeable structures, not only greatly dissipate the first harmonic, but also reduce the variation in the amplitude of the secondary harmonics. An interesting aspect of the work of Losada et al. (1997) is the definition of the effective water depth, h_{ef}, as a useful parameter to quantify the influence of structure permeability on the potential harmonic generation. In fact, it is well known that the relative wave height, H/h, and the relative water depth, kh, are two important dimensionless parameter that affect the potential harmonic generation when waves propagate over a submerged structure. For a wave propagating over a porous step, the variation of the wavelength is affected by the depth variation as well as by the permeable characteristics of the structure and both aspects have to

be considered. So Losada et al. (1997) proposed a method to evaluate h_{ef} which substitutes h when calculating the relative water depth and the relative wave height in order to take into account the effects of structure porosity. In Figure 2.9 the effective water depth is plotted versus the friction coefficient λ, for h=10m, T=10s, structure height a=4m and varying porosities p. For an extremely porous structure (λ=0 and p=1), h_{ef} is 10m. Conversely, for high values of λ and porosity close to 0, the step is almost impermeable and the wave 'feels' an effective water depth of h_{ef}=6m.

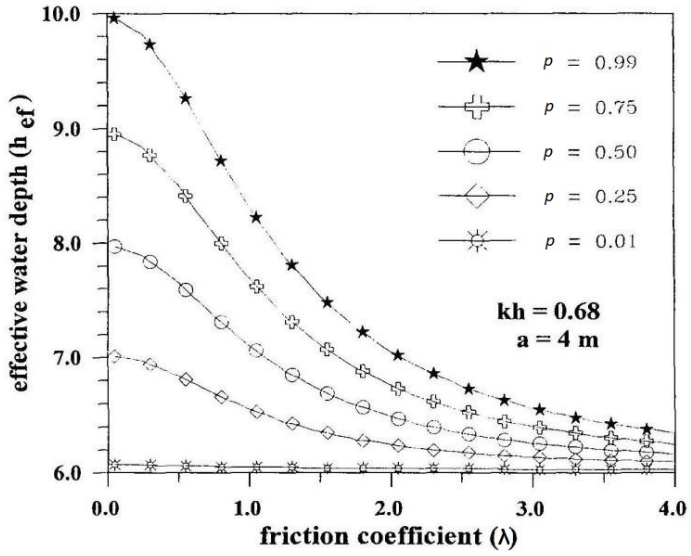

Figure 2.9: Effective depth h_{ef} versus friction coefficient λ for different porosities, h=10m, T=10s, a=4m . Adapted from Losada et al. (1997).

Therefore, for a given period and step height, increasing porosity and reducing friction, increases kh_{ef}. The Authors concluded that the porous medium tends to reduce the chance of harmonic generation due to the reduction in the relative wave height H/h_{ef} and to the increase in kh_{ef}.

2.1.2 Phenomenological description of harmonic generation

Harmonic generation in shallow water is described in this section from a phenomenological point of view. As surface gravity waves propagate toward the shore in shoaling waters, they are strongly modified with respect to their deep-water state. In shallow water, linear and non-linear dynamical processes act simultaneously to change the characteristics of the wave field. Refraction, shoaling, non-linear interactions and breaking are the typical phenomena which cause spatial variations in the wave amplitudes and directions. Although linear theory predicts the observed increasing wave amplitude and narrowing directional distributions of sea waves in a qualitative sense, non-linear effects become important in shallow water and they can not be neglected. Non-linear evolution alter the directional spectra (frequencies and directions) of the wave field as well as the wave profiles. The waves evolve from a nearly sinusoidal shape with oscillatory velocities in deep water to a shape characterized by sharp crests, flat troughs and steep shoreward faces. In addition, phase speeds substantially differ from

those predicted by the linear dispersion relationship. As waves travel from deep to shallow water, the mechanism of the non-linear wave interactions is strongly influenced by the dispersion characteristics of the wave field. Three regions of different dispersion characteristics can be distinguished:

- In deep water (relative depth $kh \gg O(1)$), the wave field undergoes strong frequency dispersion. Strong frequency dispersion is the dependency of the phase speed c on the frequency f (for deep water waves $c = g/\omega$ where g is the gravitational acceleration and $\omega = 2\pi f$ is the radian frequency). In this region, the dispersion characteristics permit resonant interactions among quartets of waves to occur, resulting in slow cross-spectral energy transfers. Although energy exchanges due to these nonlinearities are very small on wavelength scales, the wave spectrum is substantially modified over hundreds of wavelengths (Hasselmann (1962)).

- In very shallow water ($kh \ll 1$, within the surf zone for example), waves are almost nondispersive ($c = \sqrt{gh}$, that is, the phase speed is independent of the frequency). Near-resonant interactions among triads of waves are possible, resulting in rapid spectral evolution.

- In intermediate depths ($kh = O(1)$), between the deep-water region with strongly dispersive waves and the shallow-water region with nondispersive waves, waves are weakly dispersive ($c = (g/\omega)\tanh kh$) and undergo substantial changes caused by the off-resonant energetic triad interactions. Triad interactions drive rapid spectral evolution over several wavelengths.

2.1.3 Non-linear triad wave interactions

In the shoaling region, the short evolution distance and moderate dispersion suggest that second-order nonlinearities involiving triad of waves are important. Triad interactions occur among waves with frequencies and wavenumbers such that:

$$f_1 \pm f_2 = f_3 \tag{2.1}$$

and

$$\boldsymbol{k_1} \pm \boldsymbol{k_2} = \boldsymbol{k_3} \tag{2.2}$$

where f and $\boldsymbol{k}$ are the scalar frequency and vector wavenumber, respectively. The wave components (f_1,$\boldsymbol{k_1}$) and (f_2,$\boldsymbol{k_2}$) each satisfy the linear dispersion relation:

$$\omega^2 = gk\tanh(kh) \tag{2.3}$$

in which k is the wavenumber magnitude. The physical meaning of (2.1) and (2.2) is that the sum (or difference) interaction between wave components 1 and 2 forces motions with the scalar-sum (or difference) frequency and the vector-sum (or difference) wavenumber. If component 3 satisfies the linear dispersion relation (2.3) then the interaction is resonant (Armstrong et al., 1962) implying a continued one-way transfer of energy to component 3. Note that for gravity surface waves this is only possible in very shallow water where the waves are nondispersive. If component 3 does not satisfy the linear dispersion relation (2.3) then the interaction is non-resonant (in intermediate depths were waves are weakly dispersive) and the transfer is back-and-forth because of the mismatch in the phase speed. The intensity of the triad interactions is mainly controlled by the phase mismatch. The difference between the so-called

bound wavenumber given by $|\boldsymbol{k_1} \pm \boldsymbol{k_2}|$ and the free wavenumber obtained from the linear dispersion relation $|\boldsymbol{k}(f_3)|$ represents the wavenumber mismatch:

$$\Delta_k = |\boldsymbol{k_1} \pm \boldsymbol{k_2}| - |\boldsymbol{k}(f_3)| \tag{2.4}$$

The normalized wavenumber mismatch

$$\delta_k = \Delta_k / |\boldsymbol{k}(f_3)| \tag{2.5}$$

is a measure of the departure from exact resonance (Freilich and Guza, 1984). Its magnitude determines the intensity of energy exchanges between the interacting waves. Zero mismatch (non dispersive shallow-water waves) represents the limiting case in the interaction process, in which the interacting waves remain intact and in phase (resonant interaction) during evolution. Thus, the magnitude of energy transfer is maximum and a continued one-way transfer takes place to the harmonics over relatively short evolution distance. When the mismatch is small ($\delta_k \ll 1$, in weakly dispersive shoaling waves), phase relations between the interacting waves vary only slightly over a wavelength. Consequently the magnitudes and the sign of energy transfers between the interacting waves allowing significant net energy transfers over several wavelengths. Large values of the mismatch (strongly dispersive deep-water waves), imply that phase relations between interacting waves vary rapidly over a wavelength, not allowing for significant energy transfer. It is common practice to distinguish between the sum and the difference interactions. In shallow water, the sum interactions between the primary waves at the energetic part of the spectrum (with peak frequency f_p) lead to the generation of harmonics around a frequency $2f$ (first harmonic of the primary). Eventually, the sum interactions between the primary waves near f_p and the first harmonics at $2f_p$ give rise to harmonics near $3f_p$. The difference interactions between primary waves within the energetic part of the spectrum lead to the generation of bound long waves.

2.2 Bispectral Analysis of shallow water waves

2.2.1 The bispectrum

The bispectrum was introduced by Hasselmann et al. (1963) to examine wave nonlinearity in intermediate water depths. Since its introduction, bispectral analysis has been used by many investigators to study nonlinear phenomena in a wide variety of fields. Elgar and Guza (1985a) used the bispectral analysis to examine the skewness and asymmetry of shoaling nonbreaking surface gravity waves. The sea surface elevation can be represented using spatially varying Fourier components, in which the time variation can be factored out (assuming time periodicity) as follows:

$$\eta(x,t) = \sum_{p=-\infty}^{\infty} C_p(x) exp[-i(\omega_p t)] \tag{2.6}$$

where ω is the radian frequency ($= 2\pi f$), p is the rank of the harmonic, C_p is the complex Fourier amplitude varying with position x. For a Gaussian sea, the sea surface can be represented as a superposition of statistically independent waves in which the phases are random. Consequently the sea surface can be fully described by the continuous energy spectrum, which is defined as the Fourier transform of the second-order correlation function $R(\tau)$ of the time series,

$$E(\omega) = \frac{1}{2\pi} \int_{-\infty}^{+\infty} R(\tau) exp(-i\omega\tau) d\tau \tag{2.7}$$

where $R(\tau)$ is given by

$$R(\tau) =< \eta(t)\eta(t+\tau) > \tag{2.8}$$

in which τ is a time lag and $< . >$ denotes the expected-value, or average, operator. For discretely sampled data, the discrete energy spectrum E_p can be represented in terms of Fourier amplitudes,

$$E_p =< C_p C_p^* > \tag{2.9}$$

Here C_p^* is the complex conjugate amplitude of C_p. The discrete energy spectrum E_p is related to the continuous one by $E_p = E(\omega)\Delta\omega$ for $\omega \cong \omega_p$, in which $\Delta\omega = 2\pi\Delta f$ is the angular frequency-band. The energy spectrum (2.9) is independent of the phases. If the phases of Fourier components are not random and statistically correlated, the sea surface is not Gaussian (Hasselmann et al., 1963). Departure from a Gaussian form cannot be detected by the energy spectrum. Higher-order spectra such as the bispectrum can be used to investigate nonlinearity in shallow-water waves. It is a complex quantity, formally defined as the Fourier transform of the third-order correlation function of the time series:

$$B(\omega_1,\omega_2) = (\frac{1}{2\pi})^2 \int_{-\infty}^{+\infty} \int R(\tau_1,\tau_2) exp[-i(\omega_1\tau_1 + \omega_2\tau_2)] d\tau_1 d\tau_2 \tag{2.10}$$

in which

$$R(\tau_1,\tau_2) =< \eta(t)\eta(t+\tau_1)\eta(t+\tau_2) > \tag{2.11}$$

The digital (discrete) bispectrum, for discretely sampled data, is

$$B_{l,m} =< C_l C_m C_{l+m}^* > \tag{2.12}$$

in which l and m are the frequency indices. The digital bispectrum for discretely sampled data can be estimated from (2.12) by ensemble averaging. It relates to a triad of waves with frequency indices l, m and $l+m$. The bispectrum $B_{l,m}$ vanishes if:

1. There is no energy present at frequencies l or m or $l+m$ (i.e., zero Fourier amplitude of any component participating in the triad interactions);

2. There is no phase relation (coherence) between the waves forming the triad (i.e., statistically independent free waves).

On the other hand, if the wave at $n = l + m$ is generated through the interaction between l and m, then a phase coherence will exist and the expected value of the bispectrum will be nonzero. The bispectrum can be efficiently computed using symmetry properties, in which it can be uniquely described by its values in a bi-frequency octant. For a digital time series with Nyquist frequency f_N, the bispectrum is uniquely defined within a triangle in (f_1, f_2)-space (bi-frequency plan) with vertices at ($l = 0$, $m = 0$), ($l = f_N$, $m = 0$), and ($l = f_{N/2}$, $m = f_{N/2}$). The relation between the continuous bispectrum $B(\omega_1, \omega_2)$ and the discrete $B_{l,m}$ is

$$B(\omega_1, \omega_2) = (\frac{1}{\Delta\omega})^2 B_{l,m} \tag{2.13}$$

in which $\Delta\omega$ is the frequency-band, $\omega_1 = l\Delta\omega$ and $\omega_2 = m\Delta\omega$.

The bispectrum can be used to identify coupled modes, however it does not give a qualitative measure of the intensity of non-linear interactions cince its value depends on the amplitudes of the three waves involved in the interaction. So, it is convenient to cast the bispectrum into its normalized magnitude and phase, the so-called bicoherence and biphase, given respectively by (Kim and Powers, 1979):

$$b^2_{l,m} = \frac{|B_{l,m}|^2}{< |C_l C_m|^2 >< |C_{l+m}|^2 >} \tag{2.14}$$

$$\beta_{l,m} = \arctan(\frac{Im\{B_{l,m}\}}{Re\{B_{l,m}\}}) \tag{2.15}$$

In a random wave field with statistically independent components, the phases are randomly distributed between $-\pi$ and π, and thus the biphase-values tende to be scattered between $-\pi$ and π. The bicoherence is independent of the wave amplitude, unlike the bispectrum. For the bicoherence normalization given by (2.14), the bicoherence value is bounded by zero and 1 ($0 \leq b^2 \leq 1$). Zero-value of the bicoherence indicates statistically uncorrelated waves. On the other hand, the maximum value of the bicoherence is unity, implying fully coupled waves. For a three-wave system, Kim and Powers (1979) showed that $b^2(l, m)$ represents the fraction of the total energy at the sum-frequency ($n = l + m$) due to the non-linear interaction.

2.2.2 Skewness and asymmetry

The so-called skewness and asymmetry of the sea surface are two important coefficients for the evaluation of the wave nonlinearity. They are a measure of the profile distortions caused by the presence of bound harmonics due to non-linear interactions. In particular, the skewness is the lack of symmetry with respect to the horizontal axis. Skewed profiles of gravity waves are those of the Stokes-type waves characterized by sharp crests and flat troughs, in which the harmonics are phase-locked and in

phase with the primary. On the other hand, the asymmetry is the lack of symmetry with respect to the vertical. Asymmetric profiles usually have steep forward fronts and mild rear faces (the so called saw-toothed shape), in which the harmonics are phase-locked and leading the primary.
The skewness of a random variable (x) is conventionally defined as its normalized third central moment:

$$Sk = \frac{< (x - \overline{x})^3 >}{\sigma_x^3} \tag{2.16}$$

where $\overline{x}$ and σ_x are the mean and the standard deviation of x. The skewness of the free surface elevation can be written as:

$$Sk = \frac{< (\eta - \overline{\eta})^3 >}{\sigma_\eta^3} \tag{2.17}$$

where $< . >$ is the time-averaging operator, $\overline{\eta}$ and σ_η are the mean and the standard deviation of the free surface elevation. The mean square, or the variance of the surface elevation σ_η^2, can be determined from the integral of the energy spectrum. In a discrete form:

$$\sigma_\eta^2 = \sum_{p=-\infty}^{\infty} E_p \tag{2.18}$$

Hasselmann et al. (1963) showed that the integral over the real part of the bispectrum was equal to the mean cube, or third-order moment of the surface elevation

$$< (\eta - \overline{\eta})^3 >= \sum_{l=-\infty}^{\infty} \sum_{m=-\infty}^{\infty} Re\{B_{l,m}\} \tag{2.19}$$

Using symmetry properties, the bispectrum can be uniquely defined by its values in a bi-frequency octant. For a digital time series with Nyquist frequency f_N, the bispectrum is uniquely defined within a triangle in (f_1, f_2)-space with vertices at (f_1=0, f_2=0), (f_1=$f_{N/2}$,f_2=$f_{N/2}$) and (f_1=f_N,f_2=0). The result that the mean cube of the time series is related to the real part of the bispectrum (Eq. 2.19) can be rewritten as (Elgar and Guza, 1985a):

$$< (\eta - \overline{\eta})^3 >= 6 \sum_{l=l_{min}}^{N/2} Re\{B_{l,l}\} + 12 \sum_{m=l_{min}}^{N/2} \sum_{l=m+1}^{N-m} Re\{B_{l,m}\} \tag{2.20}$$

where $l > m$ and l_{min} corresponds to the index of the first discrete frequency in the sea-swell range. The factors 6 and 12 arise from the fact that the previously introduced bispectrum triangle covers 1/6 of the bispectrum diagonals and 1/12 of the remaining bispectral area. The skewness or the non-dimensional mean cube of the surface elevation can be obtained by normalizing (2.20) by the variance to the power 3/2:

$$Sk = \frac{6 \sum_{l=l_{min}}^{N/2} Re\{B_{l,l}\} + 12 \sum_{m=l_{min}}^{N/2} \sum_{l=m+1}^{N-m} Re\{B_{l,m}\}}{(\sum_{l=l_{min}}^{N} 2E_l)^{3/2}} \tag{2.21}$$

The factor 2 in the denominator arises from the fact that the double-sided variance spectrum is only summed over the positive frequency range.

The asymmetry can be defined as the skewness of the Hilbert transform of the time series, according to Elgar and Guza (1985a):

$$As = \frac{< \mathcal{H}(\eta - \overline{\eta})^3 >}{\sigma_\eta^3} \tag{2.22}$$

where $\mathcal{H}$ is the imaginary part of the Hilbert transform. Similarly to the skewness, the asymmetry of the surface elevation can be obtained from the bispectrum as the integral over the imaginary part after normalization with the variance to the power 3/2:

$$As = \frac{\sum_{l=-\infty}^{\infty} \sum_{m=-\infty}^{\infty} Im\{B_{l,m}\}}{(\sum_{l=l_{min}}^{N} 2E_l)^{3/2}} \tag{2.23}$$

The skewness and asymmetry represent overall measures of nonlinearity and indicate the deviation of the wave profile statistics from the Gaussian distribution. These parameters are used in the analysis of the experimental data presented in the following sections.

The transformation of wave skewness and asymmetry when waves propagate over a smooth and a rubble mound low-crested breakwater (LCB) has been described by Peng et al. (2009) based on measurements collected in the DELOS project. With the presence of low-crested structures, Peng et al. (2009) observed that wave skewness retains a positive sign on both sides of LCBs but asymmetry changes from negative on the incident side to positive on the transmission side. To better understand the transformation of wave asymmetries, Peng et al. (2009) applied bispectral analysis to study the contributions to the wave skewness and asymmetry from the interactions of different wave frequencies, as done Elgar and Guza (1985a). Bispectral analysis showed that positive skewness and negative asymmetry arises from self–self and sum interactions but positive asymmetry is due to difference interactions between frequencies.

2.3 Wave-induced run-up

The swash zone is a transition zone that separates the emerged and the submerged beach. This zone is of particular interest because it includes the processes that result in coastal inundation (Stockdon et al. (2006)). The still water level that would exist in the absence of wind and wind-generated waves is the astronomical tide level. The storm action that makes the sea level rise above the mean tide level is known as storm surge and it is made of two main components: the wind setup, i.e., the water piling up as a result of wind that blow in the onshore direction over the sea surface; and the barometric setup, i.e., the water piling up induced by low atmospheric pressure events. Wave setup is the super-elevation of the mean water surface (MWS) in the surf zone due to the cross-shore radiation stress gradient produced by wave breaking (Longuet-Higgins and Stewart, 1964). On natural beaches the setup level varies on time scales of the order of 100s in response to wave groups and the resulting time-varying breakpoint (Symonds et al., 1982). These contributions add to the oscillating motion of waves along the beach face, the so called swash, which has the time scale of individual wind waves and it is caused by the fact that waves still have energy when reaching the shoreline.
The wave run-up is defined as the set of discrete water level elevation maxima, measured on the foreshore, with respect to the still water level SWL (the water level that would occur in the absence of wind and waves). So the run-up can be divided into two dynamically different processes: the maximum setup, $\bar{\eta}$, the time-averaged water-level elevation at the shoreline, and the swash, S, the time-varying, vertical fluctuation about the mean (Stockdon et al., 2006), as shown in Figure 2.10.

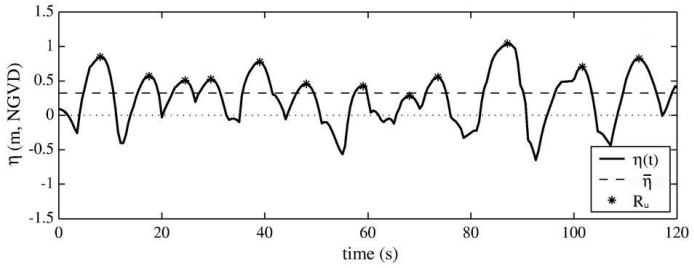

Figure 2.10: Water level elevation at the shoreline, subdivided into setup and swash. The water level elevation is in vertical direction, relative to NGVD. Adapted from Stockdon et al. (2006).

In an idealised scenario with normally incident waves breaking on a smooth, impermeable and plane slope, the main parameters that influence the wave run-up are the incident wave parameters (wave height and wave length) and the slope angle. These parameters are often combined to form dimensionless parameters that are included in theoretical and empirical design formulae attempting to predict wave run-up. This section reviews previous formulae designed to predict run-up from breaking and non-breaking waves on smooth-impermeable plane slopes, from both regular and irregular wave trains.

2.3.1 Regular wave run-up

Several parametric formulae have been proposed attempting to predict the wave run-up on smooth-impermeable slopes from regular waves. One of the first attempts to derive a theoretical run-up formula was shown by Miche (1944) and was aimed to predict wave run-up from non-breaking waves. Miche's equation was based on the linear Lagrangian equation of motion for shallow water and was given as:

$$\frac{R_u}{H} = \sqrt{\pi/2\alpha} \tag{2.24}$$

where R_u is the maximum run-up height above SWL, H is the wave height and α is the slope angle. Hunt (1959) proposed practical formulae based on previous laboratory experiments for smooth and rough plane and composite slopes. He proposed two different formulae for breaking and non-breaking waves. For non-breaking (surging) waves on plane, impermeable slopes he suggested that:

$$\frac{R_u}{H} = 3 \tag{2.25}$$

For breaking waves, he suggested that the non-dimensional run-up R_u/H was proportional to the deep-water Iribarren number ξ_o:

$$\frac{R_u}{H} = \xi_o \tag{2.26}$$

The deep-water Iribarren number is defined as:

$$\xi_o = \frac{\tan\alpha}{\sqrt{H/L_o}} \tag{2.27}$$

where $L_o = gT^2/2\pi$ is the deep-water wavelength. Often the parameter ξ_o is calculated using a finite-depth local wave height in the vicinity of the slope toe rather than a true deep-water H_o. For example, in laboratory experiments, it is common to specify H as the wave height measured over the flat-bottom portion of the wave facility before significant wave transformation occurs due to shoaling. Archetti and Brocchini (2002) showed a strong correlation between depth-integrated mass flux and wave run-up. Based on their observations, Hughes (2004) presented a new approach for predicting the run-up from non-breaking waves. He proposed a run-up formula which was not based on ξ_o. Instead, his formula was given in terms of the wave momentum flux parameter ($M_F/\rho g h^2$). This parameter represents the maximum depth-integrated wave momentum flux before reaching a slope. Hughes (2004) derived the following equation:

$$\frac{R_u}{h} = 3.84\tan\alpha\left(\frac{M_F}{\rho g h^2}\right)^{\frac{1}{2}} \tag{2.28}$$

2.3.2 Irregular wave run-up

Two main methods have been used to derive run-up formulae for irregular waves. The first method is based on the theory of equivalence, which means considering irregular wave run-up as the result of many, independent, regular waves. In this method, a typical run-up level for irregular waves, for example the significant run-up, R_{us}, is determined using a run-up formula for regular waves, and other run-up levels such as the $R_{u2\%}$ are then estimated using a Rayleigh distribution of run-up levels. The $R_{u2\%}$

parameter is defined as the vertical run-up elevation exceeded by 2% of the incoming waves at the toe of the structure. $R_{u2\%}$ is said to be a representative parameter of the wave run-up distribution of irregular wave trains and has been commonly used in existing formulae proposed to predict wave run-up.
However, formulae following this method might not be entirely realistic due to the character of natural sea states. The random nature of the incoming waves causes each wave to have a different run-up level. Unlike the case of regular waves that result in a single value of maximum wave run-up, irregular waves produce a run-up distribution. For this reason, a second method has been used to derive run-up formulae for irregular waves. This method is based on the measurements and description of the probability distribution of wave run-up under irregular or random wave conditions. This approach consists of fitting standard probability distributions to measured random wave run-up results.
One of the first formulae attempting to estimate irregular wave run-up was proposed by Wassing (1957), which was valid for milder slopes ($\tan\alpha \leq 1/3$), and was given by:

$$R_{u2\%} = 8H_{1/3}\tan\alpha \tag{2.29}$$

where $H_{1/3}$ is the significant wave height (average of the highest 1/3 waves) at the toe of the structure slope. Battjes (1974) showed the applicability of the Hunt formula (Equation 2.26) for irregular waves breaking as plungers and included reduction factors to account for various rough slopes such as rock and concrete armour. After this, most formulae proposed to predict wave run-up from irregular waves have also been based on the Iribarren number ξ_o.
Ahrens (1981) analysed previous studies which had reported measurements of irregular wave run-up on smooth-impermeable slopes with slope angles ranging from $\tan\alpha = 1/4$ to $\tan\alpha = 1/1$. For breaking waves on a slope of $\tan\alpha = 1/4$ he suggested that the elevation exceeded by 2% of the run-ups could be estimated by a slightly modified Hunt formula:

$$\frac{R_{u2\%}}{H_{m0}} = 1.6\xi_{op} \tag{2.30}$$

where

$$\xi_{op} = \frac{\tan\alpha}{\sqrt{H_{m0}/L_{op}}} \tag{2.31}$$

where H_{m0} is the energy-based zeroth-moment wave height and L_{op} is the deep-water wavelength, which is calculated with the peak spectral wave period T_p. This formula was valid for $\xi_{op} \leq 2.5$. For steeper slopes and non-breaking waves, Ahrens (1981) proposed to use the following formula:

$$\frac{R_x}{H_{m0}} = C_1 + C_2\frac{H_{m0}}{gT_p^2} + C_3(\frac{H_{m0}}{gT_p^2})^2 \tag{2.32}$$

where C_1, C_2, C_3 are empirical coefficients and R_x is a place-holder for run-up exceedence levels (2%, significant and mean).
Hughes (2004) proposed empirical equations to estimate irregular waves based on the momentum flux parameter. He proposed the following empirical equations: For non-breaking waves with $H_{m0}/L_p < 0.0225$ and $1/4 \leq \tan\alpha \leq 1/1$:

$$\frac{R_{u2\%}}{h} = 1.75(1 - e^{-(1.3\cot\alpha)})(\frac{M_F}{\rho g h^2})^2 \tag{2.33}$$

For breaking waves with $H_{m0}/L_p > 0.0225$ and $1/5 \leq \tan\alpha \leq 2/3$:

$$\frac{R_{u2\%}}{h} = 4.4(\tan\alpha)^{0.7}(\frac{M_F}{\rho g h^2})^2 \tag{2.34}$$

For breaking waves with any value of H_{m0}/L_p and $1/30 \leq \tan\alpha \leq 1/5$:

$$\frac{R_{u2\%}}{h} = 4.4(\tan\alpha)^{0.7}(\frac{M_F}{\rho g h^2})^2 \tag{2.35}$$

Experiments on natural beaches have confirmed the usefulness of the surf similarity parameter for the scaling of run-up under different wave conditions and for a wide range of natural beach types (Nielsen and Hanslow, 1991). Nielsen and Hanslow (1991) showed that there was a proportionality between the run-up and the beach face slope $\tan\alpha_f$ for steeper beaches ($\tan\alpha_f \geq 1/10$). For flatter beaches ($\tan\alpha_f \leq 1/10$) the slope becomes largely unimportant. Thus, for dissipative beaches the run-up scales directly with $(H_o L_o)^{0.5}$.
The wave run-up on beaches has also been studied using field measurements with video techniques and several formulae have been proposed. The most recent formulas are those suggested by Stockdon et al. (2006) and Vousdoukas et al. (2011). Stockdon et al. (2006) obtained the following parametrization for the 2% exceedence value of run-up peaks on all natural beaches:

$$R_{u2\%} = 1.1\left(0.35\tan\alpha_f(H_o L_o)^{1/2} + \frac{[H_o L_o(0.563\tan^2\alpha_f + 0.004)]^{1/2}}{2}\right) \tag{2.36}$$

$\tan\alpha_f$ is defined as the average slope over a region $\pm 2\sigma_\eta$ around $\bar{\eta}$, where σ_η is the standard deviation of the continuous water level record, $\eta(t)$. For Iribarren numbers less than 0.3 Stockdon et al. (2006) found that the setup and the total swash were best parametrized using only offshore wave height and wavelength. Therefore, under extremely dissipative conditions ($\xi_o < 0.3$), estimates of $R_{u2\%}$ were improved using the dissipative parametrization:

$$R_{u2\%} = 0.043(H_o L_o)^{1/2} \tag{2.37}$$

Along the Italian coast, video monitoring systems have been applied by Archetti and Zanuttigh (2010) for estimating run-up and flooding on the emerged beach. In addition to provide run-up measurements, monitoring systems allows to evaluate the beach evolution and the performance of coastal defences during storm events.

Chapter 3

Experimental investigation and Analysis

In this chapter laboratory experiments, which are the basis of this study, are described in details. The experiments were carried out in the wave-flume of the Hydraulics and Maritime Construction Laboratory of the Università Politecnica delle Marche (Ancona, Italy). The general description of the flume and of the laboratory facilities, as well as the tested wave conditions are reported in the following sections. Two different experimental campaigns were performed to fully understand how the presence of a submerged obstacle influences the hydro-dynamics induced by the wave action:

- the first experimental campaign consisted in a rigid bed model with a submerged trapezoidal bar built over the horizontal bottom of the wave-flume. At the end of the flume, at the opposite side to the wave generator, an absorbing mildly sloping beach (with a 1:20 slope) made of coarse gravel was used to reduce the wave reflection and to guarantee undisturbed flow conditions in the measuring area. Measurements of the free surface elevations were recorded at fifteen different locations along the flume using eight parallel wire resistance wave gauges in two shifts. Both breaking and non-breaking wave conditions were tested and wave data were analysed in order to elucidate the phenomenon of frequency energy generation observed in the power spectra of waves passing over the bar.

- in the second experimental campaign the beach was covered with metal plates in order to assure a smooth bottom (impermeable beach slope). The beach was then equipped with a run-up gauge and the same wave conditions of the first campaign were tested in order to have also measurements of the maximum wave run-up in the presence of the submerged obstacle.

3.1 Experimental setup

The experiments were carried out in the wave-flume of the Hydraulics and Maritime Construction Laboratory of the Università Politecnica delle Marche (Ancona, Italy). The wave-flume (Figure 3.1) has an overall length of 50m, width 1.0m and height 1.3m. The wave motion was forced by a piston-type wave-maker that operates up to a maximum run of 0.5m (semi-stroke) and a maximum velocity of 0.8m/s. The control signal is provided via a dedicated personal computer, which is connected to

a DA-AD converter that supplies the voltage input for the amplifier which in turns sends the amplified signal to the driver. The time series signals used as input for the wave-maker were generated by a software named *WaveMaker* developed by *HR Wallingford*. The software can generate random-phase time series corresponding to JONSWAP type spectra for different peak enhancement factors as well as monochromatic waves.

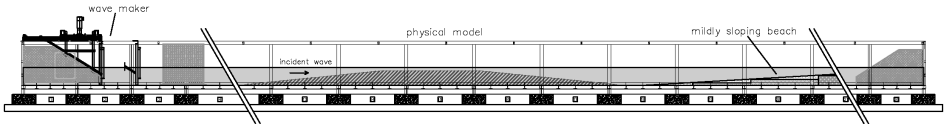

Figure 3.1: Global sketch of the wave-flume for the physical model realized in the Hydraulics and Maritime Construction Laboratory of the Università Politecnica delle Marche (Ancona, Italy).

The bottom profile selected for the experiments is shown in Figure 3.2. A smooth submerged trapezoidal bar was constructed, consisting of upslope and downslope ramps of 1:10 and a 3m horizontal crest. The height of the bar crest was 0.41m above the bottom of the flume. Aluminium plates was used to realize the obstacle and they were reinforced with longitudinal bars in order to minimize lifting and displacement forces induced by the wave motion. For the first experimental campaign, waves were measured at fifteen stations in the flume using eight *HR Wallingford* parallel wire resistance wave gauges in two shifts, as sketched in Figure 3.2. In Figure 3.2 stations 1 to 8 correspond to group 1 (8 gauges, first shift) while stations 9 to 15 to group 2. The first measuring point (station 1) was common to the two shifts, enabling the repeatability of the two experiments to be checked. This gauge served also as the reference gauge for the incident waves. Wave gauges 2 to 5 were set up in the horizontal part of the flume so as to permit measurements of wave reflection from the bar by applying the nonlinear method proposed by Lin and Huang (2004). The other gauges were arranged symmetrically with respect to the bar at about 1m intervals to evaluate the transformations of waves passing the obstacle. The gauge 15 at the last station was used as reference for the transmitted waves.

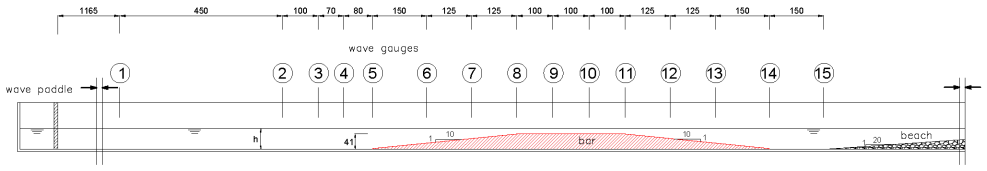

Figure 3.2: Experimental set-up and location of wave gauges for the first experimental campaign.

The wave probe operates by measuring the current that flows between two stain-

less steel wires that are immersed in the water. This current is converted to an output voltage that is directly proportional to the immersed depth. The relationship between the voltage and the immersed depth is linear and it is evaluated by means of the instrument calibration. The wave gauges were calibrated before each set of experimental tests, on a daily basis, and every time there was some modification in the calibration parameters for the different electric conductibility of water due to the environmental conditions. The acquisition of the gauge signals was made by means of a home made software named *WaveLogger*. In each run, data were recorded simultaneously from 8 separated channels at a sampling frequency of 35Hz. For the first experimental campaign, at the end of the flume a beach with a 1:20 slope made of coarse gravel served as a wave absorber. The wave reflection of the beach was estimated from previous experiments and it was lower than about 4-5%. For the second experimental campaign, the gravel beach was covered with metal plates in order to assure a smooth bottom with a 1:20 slope. The wave gauges 1 and 15 were left in the same locations of the first experimental campaign while the other gauges were displaced over the downslope of the submerged bar at 0.40m intervals. One wave gauge was replaced by a 3m long wave gauge that was placed along the smooth beach in order to measure the maximum wave run-up. The calibration of this wave gauge was made by varying the water depth in the wave flume at three different water levels.

3.2 Experimental program

During this experimental investigation different wave conditions were tested. The transformation of waves passing over the submerged structure was evaluated for both regular and random waves. In order to evaluate also the effect of the sea level rise, two offshore water depths h=0.51m and h=0.56m were considered and the submergence of the bar was therefore 0.10 and 0.15cm respectively. For each water depth, thirty-six monochromatic waves were generated by combining four different wave periods (T=1.0s, T=1.5s, T=2.0s and T=2.5s) and nine different wave heights from a minimum value of 2cm to a maximum value of 15cm (Tables 3.1 and 3.2). In Tables 3.1 and 3.2 the wave length L has been evaluated from T by applying the linear wave theory at the water depth h. In these cases the runs lasted 300s.
It is worthwhile to note that higher and longer waves show greater deviation from the linear wave theory and they are generated with a second-order component. In fact, most of the tested waves of these experiments are correctly described by the second-order Stokes theory, according to the graph of Le Méhauté.
A number of papers have described how to avoid the unintentional release of spurious free waves in connection with the reproduction of regular and irregular waves in physical wave flumes (Goda, 1967; Hansen et al., 1980 among others) and the following three types of problems have been identified:

- Boundary conditions based on first order wave theory leads to the release of the so-called *parasitic free waves*;
- The moving boundary of the paddle generator will generate the so-called *free displacement waves*;
- The mismatch between the vertical distribution of the horizontal particle velocity in progressive waves and the uniform profile imposed at the paddle will generate the so-called *local disturbance waves*.

However, as suggested by Goda (1967), the appearance of secondary free waves is limited to the relatively shallow water waves with large wave heights. If a test is carried out in a region where the relative water depth h/L is greater than 0.15, no secondary wave are observed. Figure 3.3 shows the limit for the appearance of secondary wave crests in a wave channel with the experimental data (white and black dots) of Goda (1967). The theoretical curve in the figure was given by Miche (1944) expressed in the form:

$$(H/L)_{critical} = \frac{1}{3\pi} \sinh^2(2\pi h/L) \tanh(2\pi h/L) \tag{3.1}$$

For the experiments of this work, the generation of secondary waves is avoided for waves with T=1.0s and T=1.5s because $h/L > 0.15$ (Tables 3.1 and 3.2). For the longer waves, the appearance of secondary waves has been verified with the graph in Figure 3.3, where the red dots are relative to the tested cases with T=2.0s and T=2.5s and both the water depths h=0.51m and h=0.56m. From Figure 3.3, the formation of secondary wave crests is mainly expected for three waves having T=2.5s, which exceed or are close to the limit identified by Miche (1944). In particular the highest two waves H=15.0cm and H=12.0cm for the lower water depth h=0.51m and the wave with H=15.0cm for h=0.56m. For these waves, the travelling of secondary wave crests was actually observed by comparing the time series of the first five wave gauges located along the horizontal part of the wave flume. These three cases were not considered for the study of the wave transformation over the bar.

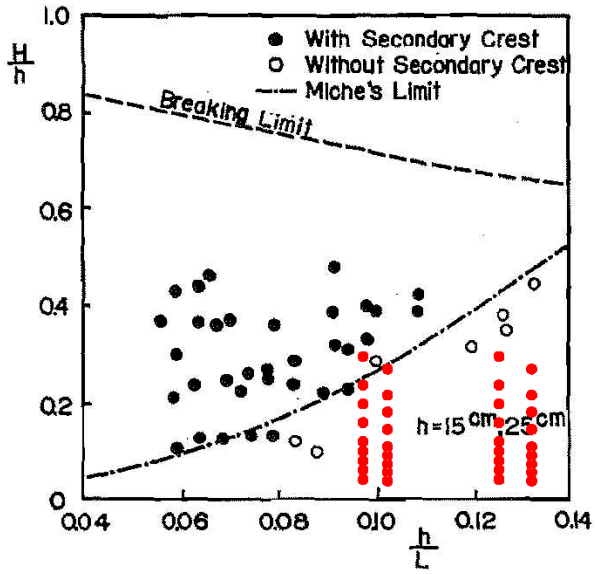

Figure 3.3: Appearance limit of secondary wave crests in a test channel, adapted from Goda (1967).

Table 3.1: Characteristics of monochromatic waves for h=0.51m.

Name	h (m)	H (cm)	T (s)	f (Hz)	L (m)	H/h	h/L
H2T10h51	0.51	2.0	1.0	1.0	1.52	0.04	0.34
H3T10h51	0.51	3.0	1.0	1.0	1.52	0.06	0.34
H4T10h51	0.51	4.0	1.0	1.0	1.52	0.08	0.34
H5T10h51	0.51	5.0	1.0	1.0	1.52	0.10	0.34
H6T10h51	0.51	6.0	1.0	1.0	1.52	0.12	0.34
H8T10h51	0.51	8.0	1.0	1.0	1.52	0.16	0.34
H10T10h51	0.51	10.0	1.0	1.0	1.52	0.20	0.34
H12T10h51	0.51	12.0	1.0	1.0	1.52	0.24	0.34
H15T10h51	0.51	15.0	1.0	1.0	1.52	0.29	0.34
H2T15h51	0.51	2.0	1.5	0.67	2.84	0.04	0.18
H3T15h51	0.51	3.0	1.5	0.67	2.84	0.06	0.18
H4T15h51	0.51	4.0	1.5	0.67	2.84	0.08	0.18
H5T15h51	0.51	5.0	1.5	0.67	2.84	0.10	0.18
H6T15h51	0.51	6.0	1.5	0.67	2.84	0.12	0.18
H8T15h51	0.51	8.0	1.5	0.67	2.84	0.16	0.18
H10T15h51	0.51	10.0	1.5	0.67	2.84	0.20	0.18
H12T15h51	0.51	12.0	1.5	0.67	2.84	0.24	0.18
H15T15h51	0.51	15.0	1.5	0.67	2.84	0.29	0.18
H2T20h51	0.51	2.0	2.0	0.5	4.09	0.04	0.13
H3T20h51	0.51	3.0	2.0	0.5	4.09	0.06	0.13
H4T20h51	0.51	4.0	2.0	0.5	4.09	0.08	0.13
H5T20h51	0.51	5.0	2.0	0.5	4.09	0.10	0.13
H6T20h51	0.51	6.0	2.0	0.5	4.09	0.12	0.13
H8T20h51	0.51	8.0	2.0	0.5	4.09	0.16	0.13
H10T20h51	0.51	10.0	2.0	0.5	4.09	0.20	0.13
H12T20h51	0.51	12.0	2.0	0.5	4.09	0.24	0.13
H15T20h51	0.51	15.0	2.0	0.5	4.09	0.29	0.13
H2T25h51	0.51	2.0	2.5	0.4	5.28	0.04	0.10
H3T25h51	0.51	3.0	2.5	0.4	5.28	0.06	0.10
H4T25h51	0.51	4.0	2.5	0.4	5.28	0.08	0.10
H5T25h51	0.51	5.0	2.5	0.4	5.28	0.10	0.10
H6T25h51	0.51	6.0	2.5	0.4	5.28	0.12	0.10
H8T25h51	0.51	8.0	2.5	0.4	5.28	0.16	0.10
H10T25h51	0.51	10.0	2.5	0.4	5.28	0.20	0.10
H12T25h51	0.51	12.0	2.5	0.4	5.28	0.24	0.10
H15T25h51	0.51	15.0	2.5	0.4	5.28	0.29	0.10

Table 3.2: Characteristics of monochromatic waves for h=0.56m.

Name	h (m)	H (cm)	T (s)	f (Hz)	L (m)	H/h	h/L
H2T10h56	0.56	2.0	1.0	1.0	1.53	0.04	0.37
H3T10h56	0.56	3.0	1.0	1.0	1.53	0.05	0.37
H4T10h56	0.56	4.0	1.0	1.0	1.53	0.07	0.37
H5T10h56	0.56	5.0	1.0	1.0	1.53	0.09	0.37
H6T10h56	0.56	6.0	1.0	1.0	1.53	0.11	0.37
H8T10h56	0.56	8.0	1.0	1.0	1.53	0.14	0.37
H10T10h56	0.56	10.0	1.0	1.0	1.53	0.18	0.37
H12T10h56	0.56	12.0	1.0	1.0	1.53	0.21	0.37
H15T10h56	0.56	15.0	1.0	1.0	1.53	0.27	0.37
H2T15h56	0.56	2.0	1.5	0.67	2.93	0.04	0.19
H3T15h56	0.56	3.0	1.5	0.67	2.93	0.05	0.19
H4T15h56	0.56	3.0	1.5	0.67	2.93	0.07	0.19
H5T15h56	0.56	5.0	1.5	0.67	2.93	0.09	0.19
H6T15h56	0.56	6.0	1.5	0.67	2.93	0.11	0.19
H8T15h56	0.56	8.0	1.5	0.67	2.93	0.14	0.19
H10T15h56	0.56	10.0	1.5	0.67	2.93	0.18	0.19
H12T15h56	0.56	12.0	1.5	0.67	2.93	0.21	0.19
H15T15h56	0.56	15.0	1.5	0.67	2.93	0.27	0.19
H2T20h56	0.56	2.0	2.0	0.5	4.25	0.04	0.13
H3T20h56	0.56	3.0	2.0	0.5	4.25	0.05	0.13
H4T20h56	0.56	4.0	2.0	0.5	4.25	0.07	0.13
H5T20h56	0.56	5.0	2.0	0.5	4.25	0.09	0.13
H6T20h56	0.56	6.0	2.0	0.5	4.25	0.11	0.13
H8T20h56	0.56	8.0	2.0	0.5	4.25	0.14	0.13
H10T20h56	0.56	10.0	2.0	0.5	4.25	0.18	0.13
H12T20h56	0.56	12.0	2.0	0.5	4.25	0.21	0.13
H15T20h56	0.56	15.0	2.0	0.5	4.25	0.27	0.13
H2T25h56	0.56	2.0	2.5	0.4	5.51	0.04	0.10
H3T25h56	0.56	3.0	2.5	0.4	5.51	0.05	0.10
H4T25h56	0.56	4.0	2.5	0.4	5.51	0.07	0.10
H5T25h56	0.56	5.0	2.5	0.4	5.51	0.09	0.10
H6T25h56	0.56	6.0	2.5	0.4	5.51	0.11	0.10
H8T25h56	0.56	8.0	2.5	0.4	5.51	0.14	0.10
H10T25h56	0.56	10.0	2.5	0.4	5.51	0.18	0.10
H12T25h56	0.56	12.0	2.5	0.4	5.51	0.21	0.10
H15T25h56	0.56	15.0	2.5	0.4	5.51	0.27	0.10

Irregular waves were generated as JONSWAP spectra with a peak enhancement factor equal to 3.3. The random seed number was left fixed for all the tests. For each peak period (T_p=1.0s, T_p=1.5s, T_p=2.0s and T_p=2.5s) three significant wave heights were selected in order to have different wave conditions: non-breaking waves, spilling breakers and plunging breakers. For larger periods, the initial wave heights at the paddle were smaller because it was attempted to keep the nonlinearity parameter, ϵ=a/h (where a is the wave amplitude), nearly the same in the shallowest part of the flume for the four cases. Such a constant parameter is particularly useful for the comparison. The characteristics of the random waves are shown in Table 3.3. For random waves, the duration of the experimental tests depends on the peak period to ensure the generation of at least 500 waves during each test. So, the runs lasted 600s for T_p=1.0s, 900s for T_p=1.5s, 1200s for T_p=2.0s and 1500s for T_p=2.5s.

Table 3.3: Characteristics of random waves.

Name	h (m)	H_s (cm)	T_p (s)	f_p (Hz)
SpH5T10h51	0.51	5.0	1.0	1.0
SpH8T10h51	0.51	8.0	1.0	1.0
SpH12T10h51	0.51	12.0	1.0	1.0
SpH4T15h51	0.51	4.0	1.5	0.67
SpH6T15h51	0.51	6.0	1.5	0.67
SpH10T15h51	0.51	10.0	1.5	0.67
SpH3T20h51	0.51	3.0	2.0	0.5
SpH5T20h51	0.51	5.0	2.0	0.5
SpH8T20h51	0.51	8.0	2.0	0.5
SpH3T25h51	0.51	3.0	2.5	0.4
SpH5T25h51	0.51	5.0	2.5	0.4
SpH8T25h51	0.51	8.0	2.5	0.4
SpH5T10h56	0.56	5.0	1.0	1.0
SpH8T10h56	0.56	8.0	1.0	1.0
SpH12T10h56	0.56	12.0	1.0	1.0
SpH4T15h56	0.56	4.0	1.5	0.67
SpH6T15h56	0.56	6.0	1.5	0.67
SpH10T15h56	0.56	10.0	1.5	0.67
SpH3T20h56	0.56	3.0	2.0	0.5
SpH5T20h56	0.56	5.0	2.0	0.5
SpH8T20h56	0.56	8.0	2.0	0.5
SpH3T25h56	0.56	3.0	2.5	0.4
SpH5T25h56	0.56	5.0	2.5	0.4
SpH8T25h56	0.56	8.0	2.5	0.4

3.3 Signal processing and analysis

The measurements recorded by the wave gauges have been processed and analysed both in the time and in the frequency domains to obtain spectral and bispectral estimates.
During the first experimental campaign, each test was repeated twice to measure the free surface in 15 different locations. In the second experimental campaign, the same wave conditions were generated again to measure the run-up over the impermeable slope. The repeatability of the runs was checked by comparing the three recordings of the wave gauge at station 1, that was left fixed.
The signals recorded by the second and the third configurations of wave gauges have been synchronized with those recorded during the same tests carried out in the first configuration. The synchronization has been done using the recordings of the first wave gauge.
The time series of the wave gauges have been processed by removing the first part of each signal, having a duration equal to the sum of the time it takes for the first wave to reach the probe and of the ramping-up time, which was equal to 10s for all the tests. The time average over the entire recording period was removed from each signal to have zero average signals.
The spectral analysis of the collected data was carried out with the use of a standard FFT package.
The signal was sampled at discrete intervals in the time domain (dt=1/35Hz=0.0286s), so it can be described as a finite sequence of N equally-spaced samples $\boldsymbol{x_n} = \{x_0, x_1, .., x_{N-1}\}$. The harmonic components of the signal have been evaluated by applying the *Discrete Fourier Transform* (DFT), which is the equivalent of the continuos Fourier Transform for signals known only at N instants. The Discrete Fourier

Transform transforms a sequence of N complex numbers $\boldsymbol{x_n}$ into another sequence of complex numbers, $\boldsymbol{X_k} = \{X_0, X_1, .., X_{N-1}\}$, which is defined by:

$$X_k = \sum_{n=0}^{N-1} x_n \cdot e^{-\frac{i2\pi}{N} kn} \tag{3.2}$$

The interval at which X_k are sampled is the reciprocal of the duration of the input sequence.
The power spectra of the signals have been computed by applying the Welch's method. The Welch's method is an improvement of the standard periodogram spectrum estimating method, in that it reduces noise in the estimated power spectra in exchange for reducing the frequency resolution. The method is based on the Bartlett's approach, which consists in a procedure to estimate the power spectrum by performing multiple DFTs. It consists in the following steps:

1. The original N point data segment is split up into K overlapping segments, each of length M.

2. After the data are split up into overlapping segments, the individual K data segments are windowed in the time domain with a *Hamming* window to reduce the effect of spectral leakage.

3. For each segment, the periodogram is calculated by computing the discrete Fourier transform, and then computing the squared magnitude of the result.

4. The individual periodograms are then averaged for the K data segments, which reduces the variance of the individual power measurements.

For monochromatic waves, data were recorded for 300s at a sampling frequency of 35Hz, for a total of 10500 data points per channel. Each record was divided into eight 50% overlapped parts, each part containing 2048 data points.
For random waves, data were recorded at a sampling frequency of 35Hz for different durations depending on the peak period. This involved that signals had different numbers of data. In order to maintain the same degree of freedom in the spectral estimates, the number of segments into which to divide the original signals was left fixed and equal to 24 for all the tests. The percentage of window overlapping was set equal to 50%. The 24 segments allow to obtain smooth PSD estimates because the random effects of noise is averaged out. However, by fixing the number of segments, the window size depends on the entire length of the signal, so the spectral estimates are obtained with different frequency resolutions.
The Welch's method has been also applied to obtain the bispectral estimates. The bispectra of monochromatic waves are computed by ensemble averaging over 8 50% overlapped segments. For random waves, the ensemble averaging was computed over 24 50% overlapped segments.

Chapter 4

Experimental Results

In the present chapter the main results of the two experimental campaigns are reported. The results are arranged in the order that better explain the obtained achievements in relation with the objectives of the thesis. In Section 4.1 the results about the transformation of waves passing over the submerged bar are presented. The analysis of the free surface data from the wave gauges has been carried out both in the time domain and in the frequency domain. At first, the monochromatic waves have been studied because they are easier to analyse and they provide quite valuable information about the generation of super-harmonics. Monochromatic waves are useful to simulate narrow-banded spectra, which are typical of sea swell conditions. Their study is also the starting point to better understand the more complex mechanisms related to the propagation of random waves. Then, random waves have been considered, where the interactions between frequency components within the spectra cause also the generation of sub-harmonics. Since the presence of the structure induces non-linear interactions between waves, their phases are not statistically independent. The deviation from a Gaussian distribution requires the application of higher order spectra, such as the bispectrum. Therefore, in this Section bispectral analyses have been also applied to the free surface records to better understand the exchange of energy between frequency components.
Finally, in Section 4.3 the data recorded by the run-up wave gauge have been analysed in order to understand how the submerged bar influences the run-up over the 1:20 impermeable slope.

4.1 Wave propagation over the submerged bar

4.1.1 Monochromatic waves

During the first experimental campaign 36 monochromatic waves were generated, by combining 9 different wave heights and 4 different wave periods.
In order to distinguish the individual effects of conservative (non-dissipative) non-linear wave interactions from those of wave breaking, it was essential to perform tests for both breaking and non-breaking waves. For each wave period, the wide range of wave heights allows to investigate three different conditions: non-breaking waves, spilling breakers and plunging breakers. The criteria for the type of breaking are to some extent subjective and based on visual observations. Generally, the type of breaking is determined with the Iribarren parameter $\xi_o = \frac{\tan\alpha}{\sqrt{H_o/L_o}}$, where $\tan\alpha$ is the

bottom slope and H_o/L_o the offshore wave steepness. Here, the distinction based on ξ_o was found not valid because the slope of the submerged bar is not uniform but it is composed by a first slope equal to 1:10 followed by a horizontal crest. Conversely to what it would be expected from the Iribarren parameter, the spilling breaking was associated to lower heights because it happened over the horizontal crest of the bar. Higher waves broke along the 1:10 slope of the bar and plunging breakers were observed.
The relative water depth (h/L) of the incident waves is another important parameter, especially when the combined effects of nonlinearity and dispersion are considered. To explore the different behaviours of shorter and longer waves, monochromatic waves with 4 different periods were tested. For the water depth of 0.51m, the waves with periods equal to 1.0s, 1.5s and 2.0s passed over the bar crest in condition of intermediate water depth ($0.05 \leq h/L \leq 0.5$). Conditions of shallow water depth ($h/L < 0.05$) were verified for the wave with period T=2.5s. For the increased water level, h=0.56m, the longest waves (with T=2.5s) are close to the shallow water limit ($h/L \approx 0.05$), while the others verified the conditions of intermediate water depth.

In order to understand the influence of wave height and wave period on the harmonic generation over the bar, six representative waves are selected from the entire dataset: two extreme periods (T=1s and T=2.5s) and three wave heights for each period. For the higher period, the chosen wave heights are lower because it was attempted to keep the nonlinearity parameter ϵ nearly the same above the bar for both cases. These six wave conditions are studied with both the tested water depths, h=0.51m and h=0.56m, to take into account also the effect of the bar submergence. The characteristics of the selected waves are reported in Table 4.1 for the water depth h=0.51m and in Table 4.2 for h=0.56m. The wave parameters are evaluated at the paddle and over the submerged bar (denoted in the Tables by $'$). The values of H and T are those imposed at the wave generator, while the wave lengths L and L' derive from the linear theory. In the shallower region characterised by the water depth h', the wave height has been evaluated as $H' = HK_s$, where K_s is the shoaling coefficient of the linear wave theory. The nonlinearity parameter has been estimated over the bar crest as $\epsilon' = a'/h'$ (where $a' = H'/2$).

Table 4.1: Characteristics of the selected waves for h=0.51m.

Name	h (m)	H (cm)	T (s)	f (Hz)	L (m)	h' (m)	L' (m)	h'/L'	ϵ'
H5T10h51	0.51	5.0	1.0	1.0	1.52	0.10	0.92	0.11	0.25
H8T10h51	0.51	8.0	1.0	1.0	1.52	0.10	0.92	0.11	0.39
H12T10h51	0.51	12.0	1.0	1.0	1.52	0.10	0.92	0.11	0.39
H3T25h51	0.51	3.0	2.5	0.4	5.28	0.10	2.45	0.04	0.21
H5T25h51	0.51	5.0	2.5	0.4	5.28	0.10	2.45	0.04	0.36
H8T25h51	0.51	8.0	2.5	0.4	5.28	0.10	2.45	0.04	0.39

Table 4.2: Characteristics of the selected waves for h=0.56m.

Name	h (m)	H (cm)	T (s)	f (Hz)	L (m)	h' (m)	L' (m)	h'/L'	ϵ'
H5T10h56	0.56	5.0	1.0	1.0	1.53	0.15	1.09	0.14	0.16
H8T10h56	0.56	8.0	1.0	1.0	1.53	0.15	1.09	0.14	0.25
H12T10h56	0.56	12.0	1.0	1.0	1.53	0.15	1.09	0.14	0.37
H3T25h56	0.56	3.0	2.5	0.4	5.51	0.15	2.98	0.05	0.13
H5T25h56	0.56	5.0	2.5	0.4	5.51	0.15	2.98	0.05	0.22
H8T25h56	0.56	8.0	2.5	0.4	5.51	0.15	2.98	0.05	0.35

First of all, it is interesting to show the quite different features of the selected monochromatic waves in the time domain. For the water depth equal to 0.51m, the shorter waves with T=1s (Figure 4.1) propagate over the bar in intermediate water depth. Their crests become steeper and their troughs flatten out as they travel upslope from station 1 to station 8, hence, they appear as higher order Stokes waves. The harmonic components remain lock in phase because the shape of the wave does not change significantly during the propagation over the obstacle. Waves with H=8cm and H=12cm break over the crest, as a consequence, they become smaller at station 10. Contrary to the shorter waves, the longer waves characterised by T=2.5s (Figure 4.2) travel over the bar in shallow water conditions for h=0.51m and they show strongly non-linear waveforms. During the propagation along the upslope, they lose their vertical symmetry and assume a saw-toothed shape at station 8. This behaviour becomes more evident for higher waves (H=5cm and H=8cm). Over the horizontal extension, where the waves are in a rather non-dispersive medium, the triplet resonance conditions are nearly satisfied (Phillips, 1960) and a very rapid flow of energy moves from the primary component to the higher harmonics. This rapid energy flow coupled with the effects of amplitude dispersion generates the so-called dispersive tail waves travelling at nearly the same celerity as the primary waves (Beji and Battjes, 1993). The dispersive tail waves appear in the wave profiles as secondary peaks behind the higher peak of the first component (station 10). These secondary peaks are bound to the primary waves but their celerity also depends on their amplitude, due to the effects of the amplitude dispersion. This explains their gradually increasing phase lag behind the primary component, that still has a larger amplitude. As waves move into the deeper water (station 13), they decompose into several smaller amplitude waves of nearly harmonic frequencies. It is evident in Figures 4.1 and 4.2 that the wave breaking does not alter the characteristic waveform drastically.

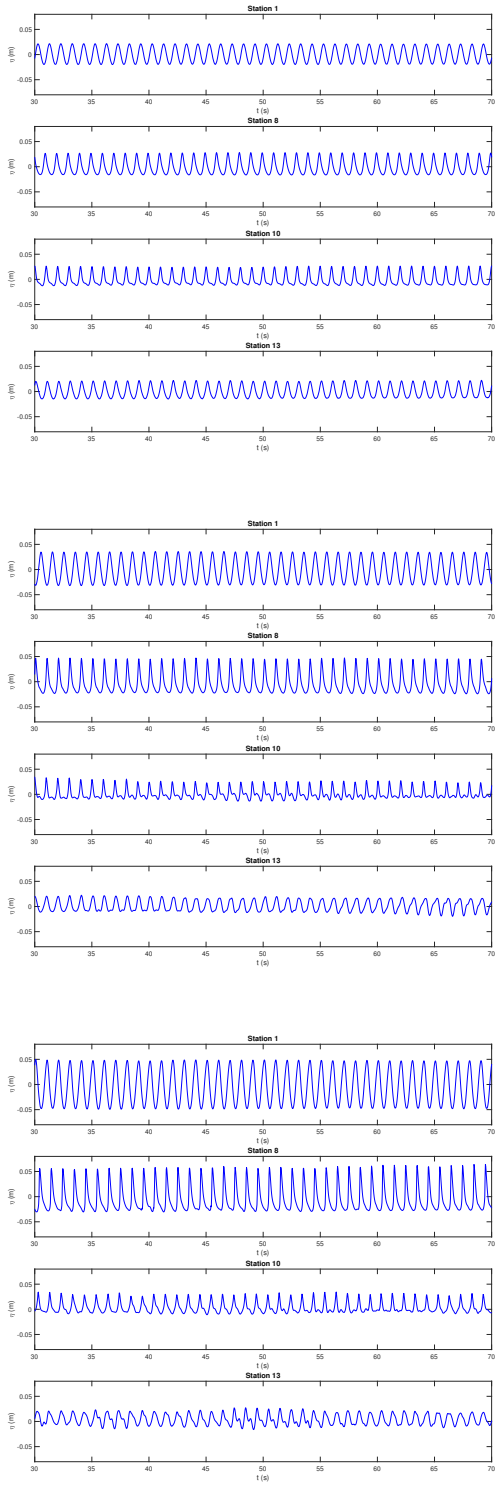

Figure 4.1: Surface elevation records of monochromatic waves with h=0.51m and T=1.0s; H=5cm (upper panels), H=8cm (middle panels), H=12cm (bottom panels).

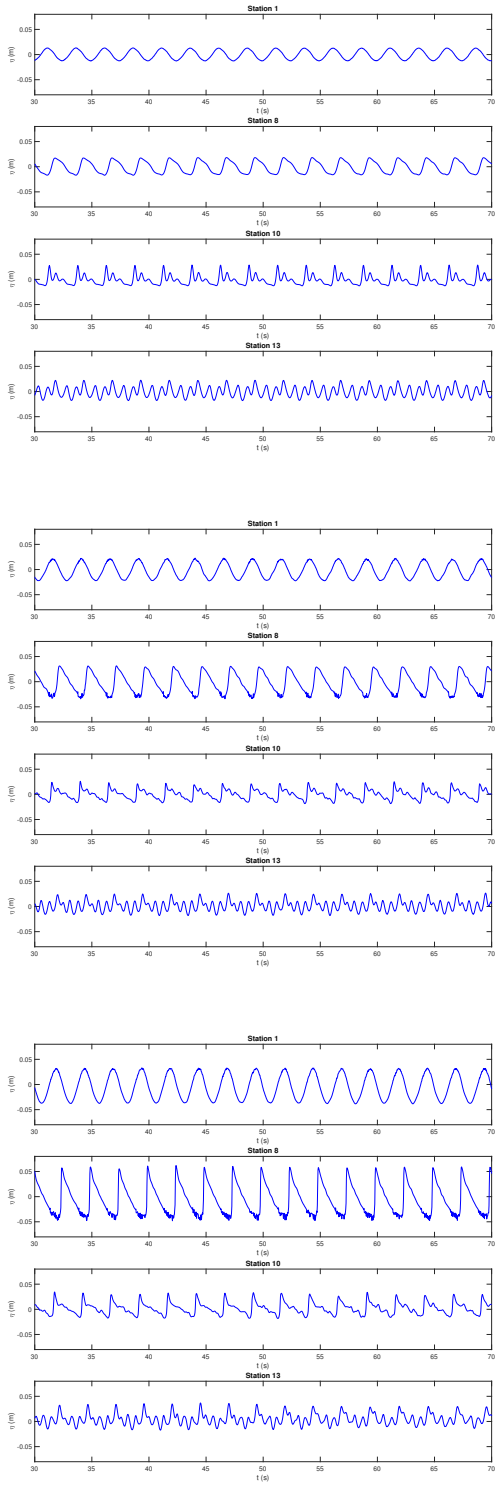

Figure 4.2: Surface elevation records of monochromatic waves with h=0.51m and T=2.5s; H=3cm (upper panels), H=5cm (middle panels), H=8cm (bottom panels).

The generation and growth of harmonics over the structure and their progression leewards can be obtained by analysing all the gauge records in the frequency domain. Amplitude spectra, spectral density of the gauge records and the associated spectral parameters are calculated. The amplitude spectra are given by $c_n = \sqrt{a_n^2 + b_n^2}$, where a_n and b_n are the Fourier coefficients corresponding to each frequency, n. Figures 4.3 and 4.4 present time series plots and amplitude spectra for the gauge locations 1, 8, 10 and 13 for the selected non-breaking waves with $\epsilon \approx 0.20$ and h=0.51m. Figure 4.3 are relative to T=1s and Figure 4.4 to T=2.5s. In both cases, the growth of higher harmonics is observed as waves propagate over the structure but this effect is more evident for the longer wave (T=2.5s), where the amplitudes of the higher frequency components become similar to that of the first harmonic. At station 10, for the wave with T=1s some energy is transmitted from the first harmonic to the second one and to a much lesser extent to the third one. At the same station, the energy of the wave with T=2.5s is distributed between a greater number of frequencies up to the fifth harmonic and all frequency components have similar amplitudes. At station 13, the third harmonic becomes dominant.

The amplitudes of the five recorded harmonics may also be traced over the structure and leewards by an examination of the spatial amplitude modulation from gauges 1 to 15. Figures 4.5 and 4.6 show the amplitudes of the individual harmonics against distance for the waves H=5cm and T=1s and H=3cm and T=2.5s, respectively. The evolution of the harmonic amplitude shows clearly how the wave period affects the generation of higher order components. During the propagation of the shorter wave (Figure 4.5), the first component remains prevalent and its amplitude is slightly reduced behind the structure. The dominant secondary component that carries energy is the second harmonic. It increases on the upslope and it reaches a maximum over the horizontal crest, where some energy is transmitted to the third and to the fourth harmonics. The wave with T=2.5s (Figure 4.6) shows a considerable growth of the first harmonic at station 8, due to the stronger effect of shoaling for longer waves. On the horizontal crest the energy carried at the first harmonic decreases because an increasing amount of energy is transmitted to the higher harmonics. In the deepening water (downslope) the amplitudes of the first, second and fourth harmonics are similar while the amplitude of the third component is almost double.

The behaviour of the breaking waves is similar to the previous ones for the same periods, with some differences due to the dissipation induced by wave breaking. Figures 4.7 and 4.9 are relative to the wave period T=1s while Figures 4.8 and 4.10 show the results for T=2.5s. On the upslope the non-linear interactions increase the amplitudes of the higher harmonics, especially that of the second harmonic. Then, since wave breaking acts by reducing proportionally the energy carried by each harmonic, it has a lesser effect on the amplitudes of the higher harmonics than on those of the first and second harmonics. This implies that the energy of the first and the second harmonics is more strongly reduced by wave breaking, hence less energy can be in turn transferred to higher frequency components as the wave continues over the bar. For the case with T=1s the result is that only the first and the second harmonics are still present leeward of the structure while the third component is negligible. Instead, for the longer waves (T=2.5s), wave breaking results in a much closer banding of energy between the varying harmonics.

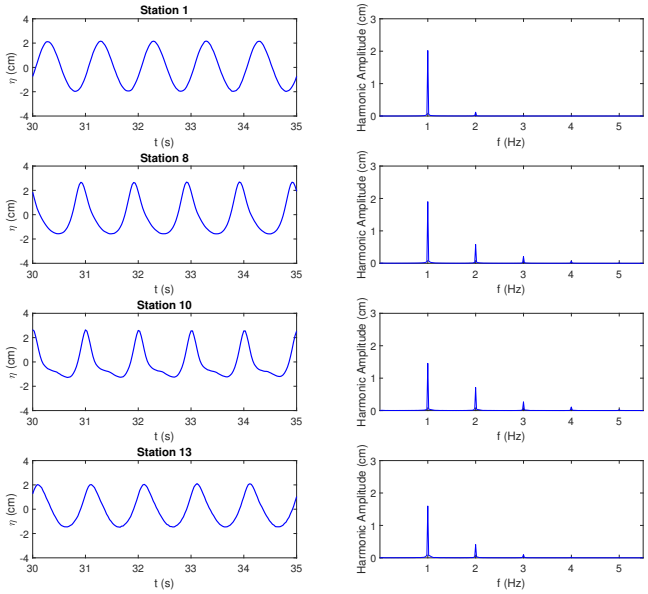

Figure 4.3: Evolution of the waveform and the corresponding amplitudes at stations 1, 8, 10 and 13; h=0.51m, H=5cm, T=1.0s.

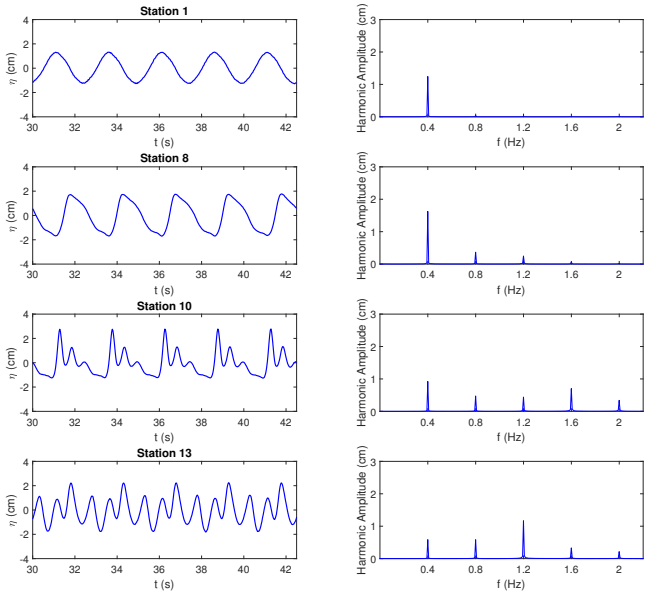

Figure 4.4: Evolution of the waveform and the corresponding amplitudes at stations 1, 8, 10 and 13;, h=0.51m, H=3cm, T=2.5s.

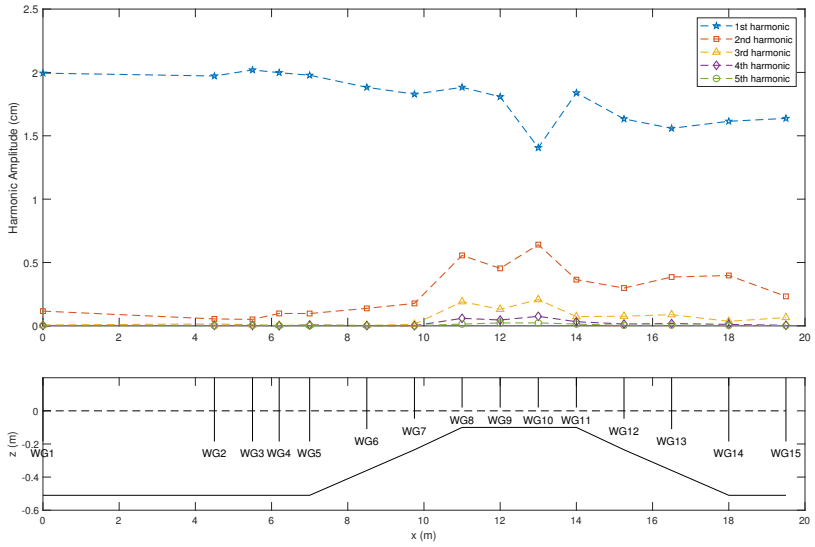

Figure 4.5: Spatial evolution of the amplitude of the first fifth harmonics; h=0.51m. H=5cm, T=1.0s.

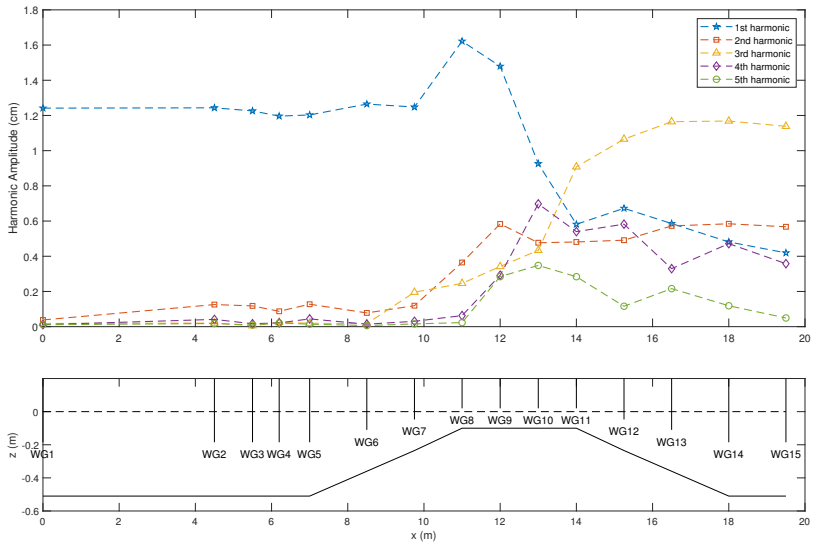

Figure 4.6: Spatial evolution of the amplitude of the first fifth harmonics; h=0.51m. H=3cm, T=2.5s.

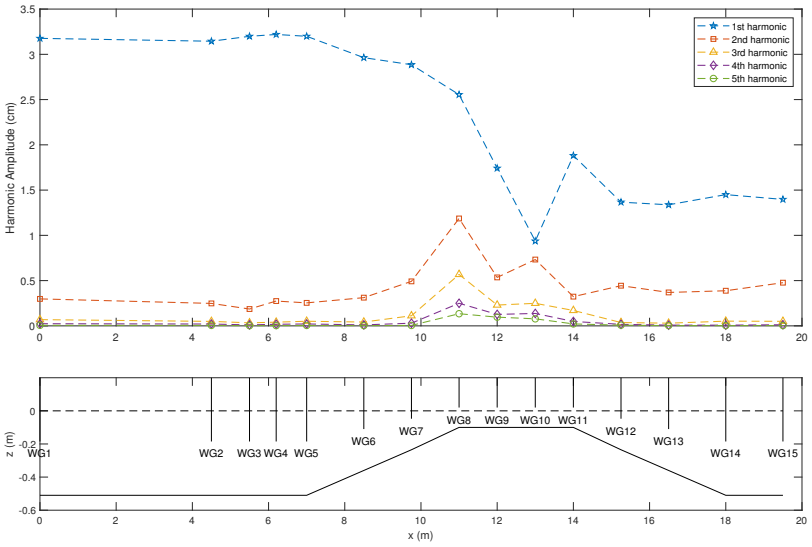

Figure 4.7: Spatial evolution of the amplitude of the first fifth harmonics; h=0.51m. H=8cm, T=1.0s.

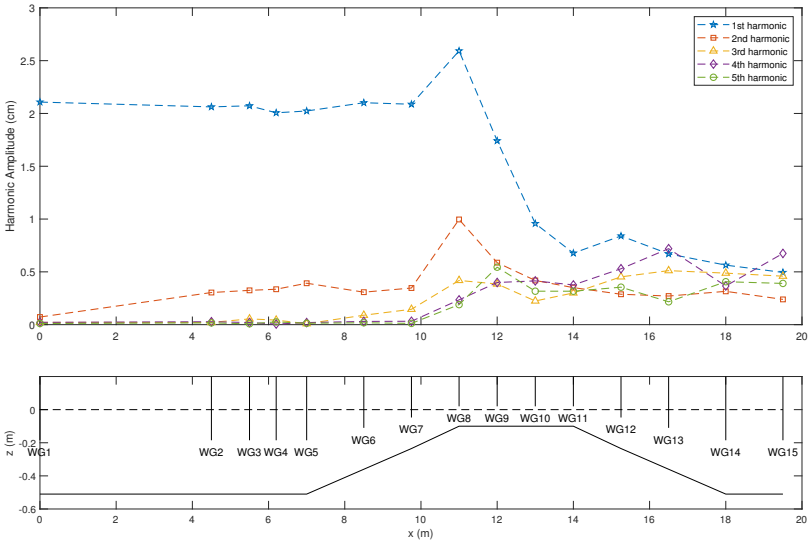

Figure 4.8: Spatial evolution of the amplitude of the first fifth harmonics; h=0.51m. H=5cm, T=2.5s.

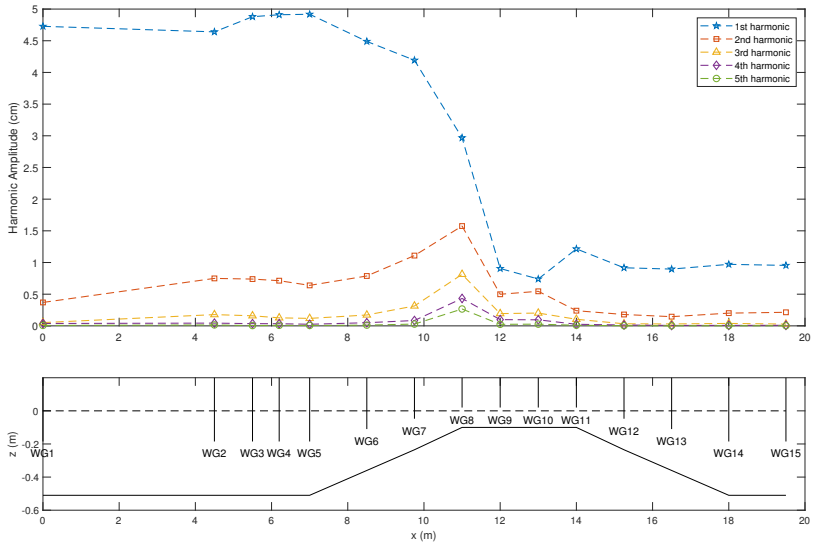

Figure 4.9: Spatial evolution of the amplitude of the first fifth harmonics; h=0.51m. H=12cm, T=1.0s.

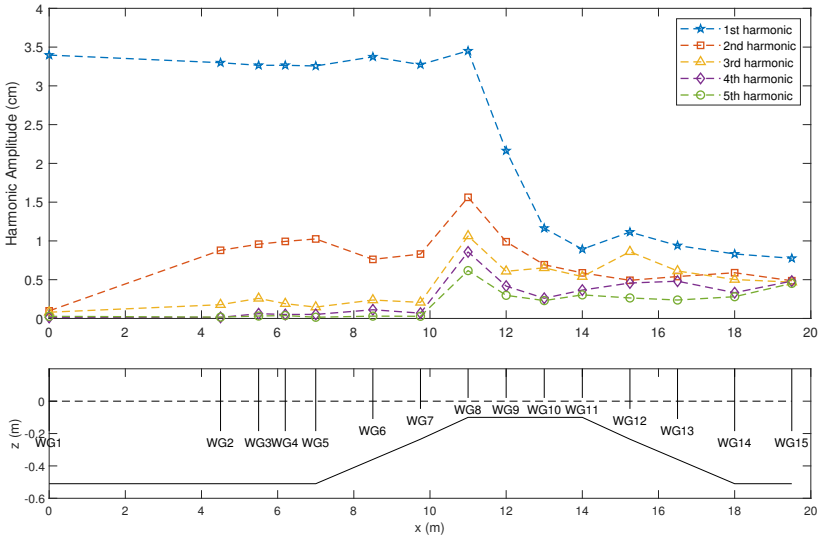

Figure 4.10: Spatial evolution of the amplitude of the first fifth harmonics; h=0.51m. H=8cm, T=2.5s.

It is noted that higher waves show greater deviation from the linear wave theory and they are generated at the wave paddle with higher second order and third order components. This effect is even more evident for the longer wave in Figure 4.10. The amplitudes of the second and third order components, which are generated at the wave paddle and develop along the first portion of the wave flume, are comparable with those of the second and third order Stokes components.
The evolution of the harmonic amplitudes is also studied for the experimental tests conducted with the increased water level. The results are reported in Figures 4.11 and 4.12 for the cases of shorter waves with H=5cm and H=12cm. For the non-breaking wave (H=5cm), the increased water level reduces the potential of harmonic generation with respect to the case with h=0.51m, so that higher components have lower harmonic amplitudes above the bar crest and leewards. The wave with H=12cm propagates over the structure in breaking conditions even with the submergence of 15cm. As the submergence of the bar increases, the energy dissipation due to wave breaking is less intense. By making a comparison with the case of lower submergence, more energy is transferred above the bar from the first harmonic to the higher components, but the first component remains prevalent. Figures 4.13 and 4.14 show the results for the longer waves with H=3cm and H=8cm. In both cases, the wave reflection from the structure produces an oscillation of the first component in front of the bar, with a wave length which is approximately half of the incident wavelength. The application of the Lin and Huang (2004) method for the evaluation of the incident and the reflected waves shows that the wave reflection increases by 9.50 times for H=3cm and by 17 times for H=8cm, when the water depth passes from 0.51m to 0.56m. For the non-breaking wave (Figure 4.13) less energy is transferred from the first harmonic to the third, fourth and fifth components during the propagation over the bar. The first and the second harmonics remain prevalent leewards. For the breaking wave (Figure 4.14), the mechanism of the harmonic generation is mainly governed by the dissipation due to wave breaking. The higher water depth reduces the intensity of wave breaking and more energy is carried by the first harmonic over the bar. The greater energy content of the first component favours the generation of harmonics, so the amplitudes of the higher components increase with respect to the previous configuration with h=0.51m. The mechanism of energy transfer between harmonic components can be better explained by the application of the bispectral analysis to the record of the free surface in Section 4.1.2.

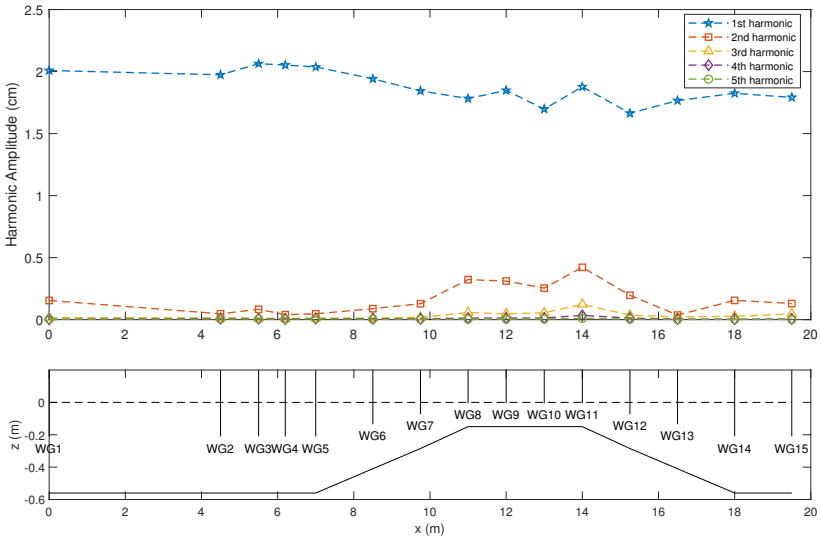

Figure 4.11: Spatial evolution of the amplitude of the first fifth harmonics; h=0.56m, H=5cm, T=1.0s.

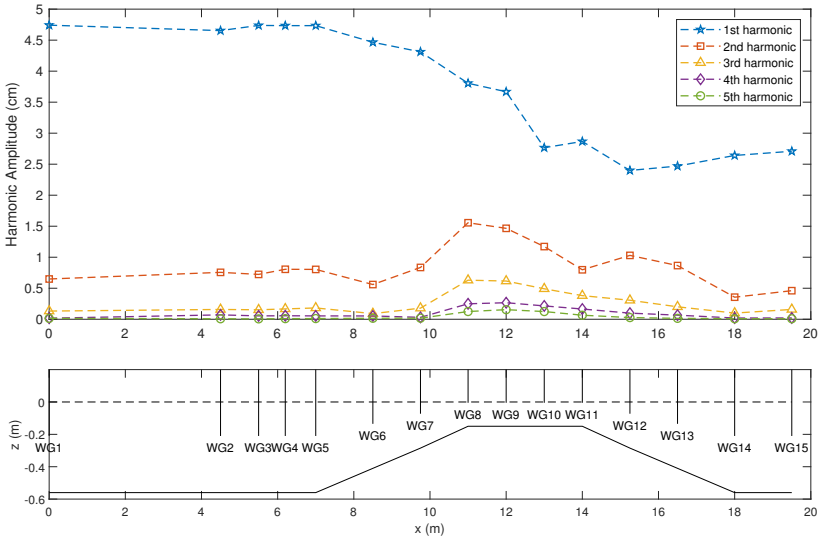

Figure 4.12: Spatial evolution of the amplitude of the first fifth harmonics; h=0.56m, H=12cm, T=1.0s.

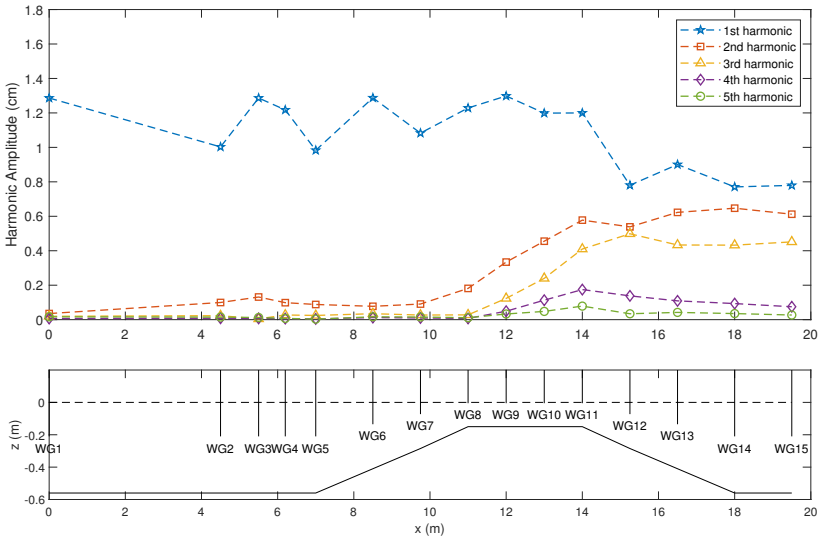

Figure 4.13: Spatial evolution of the amplitude of the first fifth harmonics; h=0.56m, H=3cm, T=2.5s.

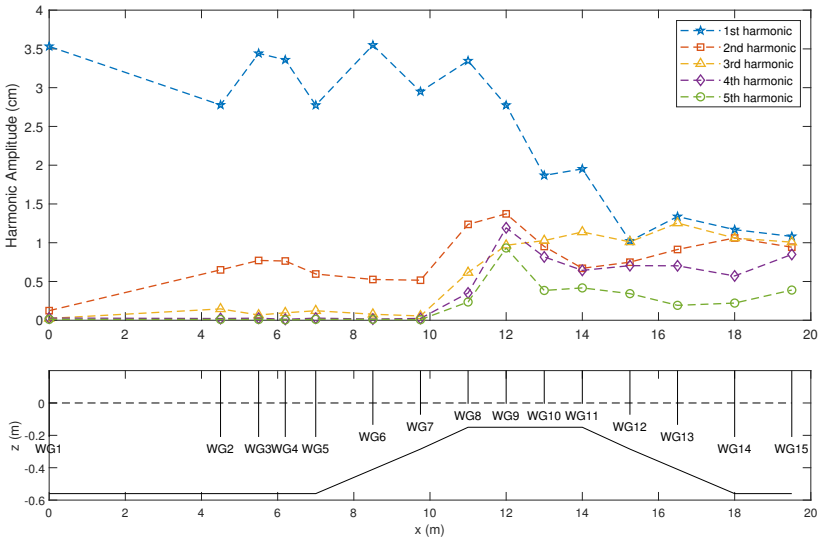

Figure 4.14: Spatial evolution of the amplitude of the first fifth harmonics; h=0.56m, H=8cm, T=2.5s.

4.1.2 Bispectral evolution of monochromatic waves

The conventional viewpoint is that on the seaside, the harmonics, bound to the primary, are amplified because of the increasing nonlinearity in the shoaling region and that they are released on the shoreside, at least partially, because of the decreasing nonlinearity in the deepening region. However, even in the shoaling region free components are generated as a result of the discontinuity in the bottom topography (Massel, 1983; Goda et al., 1999), whereas conversely some degree of phase lock may remain in the deepening region. If bound harmonic components are still present behind the structure, then the wavefield beyond the bar is statistically inhomogeneous and it cannot be fully described by the energy density spectrum without additional information about the phases.
The experimental study of Ciardulli (2009) demonstrated that the interaction between monochromatic incident waves and a submerged structure results in spatially periodic variations of the harmonic amplitudes in the protected area. This, in turn, leads to a spatial variation of the transmission coefficient. In this work, the nonlinear coupling between harmonic components is examined with the bispectral analysis as the monochromatic waves evolve while passing over the submerged bar and in the following deeper region.
Time series of surface elevation at various locations are analysed in the frequency domain to determine the bispectrum, bicoherence, biphase, skewness and asymmetry. The spatial variations of these nonlinearity indicators over and beyond the bar are of special interest also for the design practice. In fact, the asymmetry coefficients are directly related to the direction of fluid velocities and, as a consequence, with the main direction of the cross-shore solid transport.

First of all, the measured surface elevations of the non-breaking wave with H=3cm and T=2.5s are analysed to show the results of the evolution of the bispectrum during the propagation of the wave over the obstacle. The amplitude spectra for this wave (Figure 4.4) indicate significant transfers of energy from the first harmonic to higher frequencies. The bispectra are computed according to equations 2.12 and 2.13, in which the complex Fourier amplitudes C_p where determined from the time records with a standard FFT-algorithm. The data were processed by dividing the record into equal segments, each of 2048 data points resulting in a frequency resolution for the raw data of 0.0185Hz. The bispectral estimates are obtained by ensemble averaging over 8 segments, with an overlapping of 50%. Figures 4.15 and 4.16 show the amplitude spectrum (a), the absolute values of the bispectrum (b), the value of the bicoherence (c) and the imaginary part of the bispectrum (d) at four stations along the wave flume. Only the positive quadrants ($f_1,\ f_2 > 0$) are shown. Note that the bispectra are symmetric around the diagonal $f_1 = f_2$. The bicoherence is computed from the records using equation 2.14. Noisy and spiky results have been suppressed by limiting the calculations to those frequency pairs for which the absolute value of the bispectral density exceeded 5% of the maximum value in the same bispectrum. The bispectrum $B(f_1, f_2)$ describes statistically the phase relationship and energy exchange within the $(f_1, f_2, f_1 + f_2)$ triad. The imaginary part of the bispectrum is also computed because it can be used to determine the direction of non-linear energy transfers between wave frequencies (Norheim, 1998; Herbers, 2000; de Bakker et al., 2015). Different sign convention can be found in the literature for the imaginary part of the bispectrum. In this thesis, the same representation of Herbers (2000) and de Bakker et al. (2015) is used. If $\mathrm{Im}\{B(f_1, f_2)\}$ is positive, then energy is transferred from the f_1 and f_2 components to the higher-frequency $f_1 + f_2$

component. For negative $\mathrm{Im}\{B(f_1, f_2)\}$ the energy transfer reverses and the lower frequency components f_1 and f_2 grow at the expense of the higher-frequency $f_1 + f_2$ component.
The amplitude spectrum of Figure 4.15a at station 5 shows that there is already a second harmonic with frequency 0.8Hz. This harmonic is generated by the self-interaction of the first harmonic f=0.4Hz, as shown by the corresponding value of the bispectrum at $B(0.4, 0.4)$. The spatial variation of the harmonic amplitudes of Figure 4.6 can be explained by the evolution of the bispectrum. At the end of the upslope (station 8), the amplitude of the first harmonic increases due to the shoaling and contemporary the self-interaction of the first harmonic continues to transfer energy to the second component with frequency 0.8Hz (positive values of the imaginary part at $B(0.4, 0.4)$). Here, the non-linear effects become significant due to the ratio of wave height to water depth increasing and new interactions at $B(0.8, 0.4)$ appear that shift energy from $2f$ and f to $3f$=1.2Hz. Here, the second harmonic is simultaneously taking energy from the first component and releasing energy to the third harmonic. The balance of energy is positive for the second harmonic because the absolute value of the bispectrum $|B|(0.4, 0.4)$=15.44cm^3/Hz is greater than the value of 7.84cm^3/Hz at $B(0.8, 0.4)$ and in fact its amplitude increases in Figure 4.6 up to station 9. At station 10 the self-interactions of the second harmonic release energy to the fourth harmonic (positive values of the imaginary part of the bispectrum at $B(0.8, 0.8)$) and its amplitude decreases because the values of the bispectrum at $B(0.4, 0.4)$ are lower than the sum of the values at $B(0.8, 0.4)$ and $B(0.8, 0.8)$. Over the horizontal crest the wave propagates in shallow water so the triplet resonance conditions are nearly satisfied and significant energy transfers take place to higher harmonics, $4f$=1.6Hz and $5f$=2Hz. Starting from station 10 (Figure 4.16) difference interactions arise between higher harmonics, as shown by the negative values of the imaginary part at $B(1.2, 0.8)$ and $B(1.2, 1.2)$ and they transfer energy from the higher frequencies 2Hz and 2.4Hz back to 0.8Hz and 1.2Hz. In fact, higher harmonics propagate over the bar in intermediate water depth and for those frequencies the transfer of energy is back-and-forth because of the greater mismatch in the phase speed. At station 13 the wave decomposes into several waves and all frequency components return in intermediate water conditions. The intensity of the non-linear interactions remains strong on the leeside of the bar and sum and difference interactions alternate between all frequency components as the wave propagates along the downslope from station 13 to station 15. The maximum bicoherence b^2_{max} increases from 0.83 at station 1 to nearly 1 above the bar crest and it remains constant during the propagation behind the bar (Figure 4.18). A value of bicoherence close to 1 implies almost complete coupling between harmonic components.

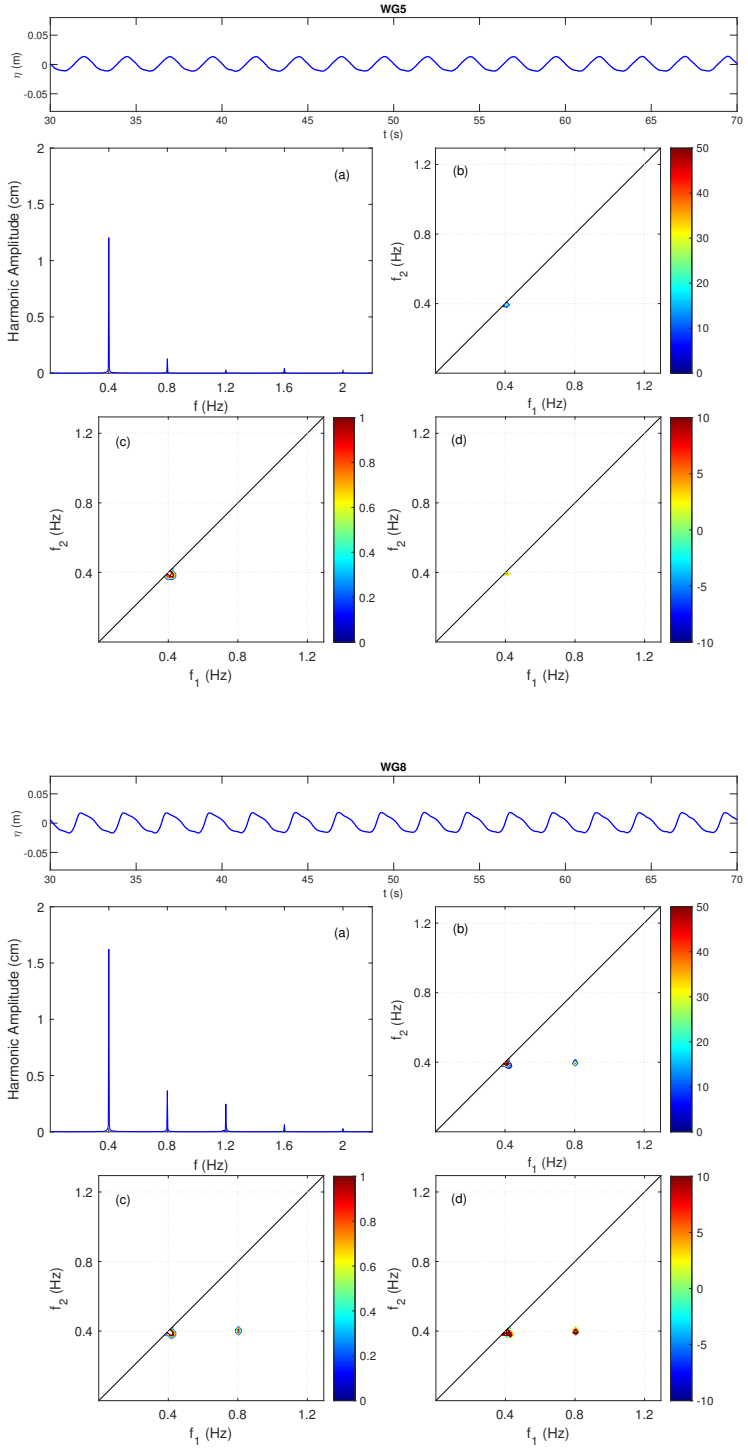

Figure 4.15: Amplitude spectrum (a), absolute bispectrum $|B|$ in cm^3/Hz^2 (b), bicoherence (c) and Imaginary part of the bispectrum (x10^{-6}) (d) at station 5 (upper panels) and station 8 (bottom panels); h=0.51m, H=3cm, T=2.5s.

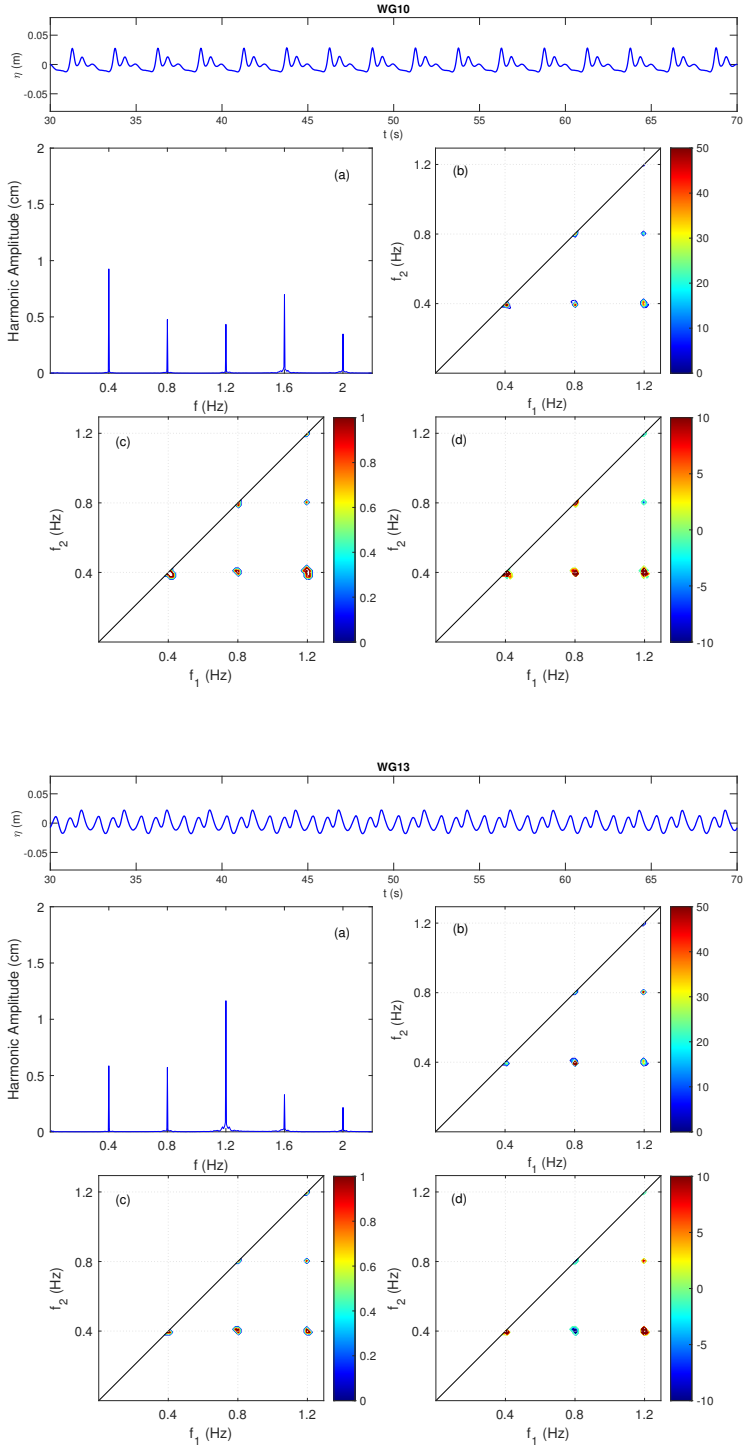

Figure 4.16: Amplitude spectrum (a), absolute bispectrum $|B|$ in cm^3/Hz^2 (b), bicoherence (c) and Imaginary part of the bispectrum (x10^{-6}) (d) at station 10 (upper panels) and station 13 (bottom panels); h=0.51m, H=3cm, T=2.5s.

The biphase has been computed from the bispectrum using equation 2.15 for selected frequency pairs. These pairs represent the phase relationships of the interacting wave components. The variations of the biphase values over the bar are plotted in Figure 4.17 where (f, f) represents the self-interaction of the first harmonic, $(f, 2f)$ denotes the interaction between the first and the second harmonic, $(f, 3f)$ and $(2f, 2f)$ are relative to the interactions between the first and the third harmonic and the self-interactions of the second harmonic, respectively. Up to station 6, the biphase of only the self-interaction (f, f) is shown; biphases of the other interactions are not plotted because no energy exists at the higher harmonics. The near-zero values of the biphase from station 1 to station 6 implies Stokes-type waves with sharp crest and flat troughs. As the waves propagate over the upslope side of the bar, the biphases converge to a value of $-\pi/2$ over the bar crest implying a wave pitched forward (saw-toothed shape). Over the downslope of the bar the biphase-value of the (f, f) interaction evolves to positive values. The biphases of the other harmonic interactions tend to be randomly scattered beyond the bar, hence, higher harmonics are largely released beyond the bar due to the decreasing nonlinearity.

The variation of the skewness and the asymmetry computed from the bispectra over the upslope, the bar crest and the downslope is shown in Figure 4.18. As a check on the bispectral calculation, the skewness and the asymmetry obtained directly from the time series (Eq. 2.17 and 2.22) are also plotted. The agreement is quite good. The variations of the non-linear parameters in Figure 4.18 are consistent with the evolution of the wave profile shape. From station 2 to station 6, the skewness shows positive values around 0.2, values that are representative of second order Stokes waves. Near-zero values are computed for the asymmetry up to station 7, then a sudden decrease is observed with a minimum over the bar crest, where the wave profile is characterised by very steep forward fronts and the biphases of the interactions converge to $-\pi/2$. The skewness increases over the horizontal part of the obstacle showing a maximum at the end of the crest, a little forward with respect to the minimum value of the asymmetry. On the downslope side of the bar, the skewness and asymmetry have rapid fluctuations between values ± 0.5. This means that the harmonics are not completely independent and the exchange of energy among different wave components continues, as demonstrated by the fact that the absolute bispectrum does not cancel out behind the obstacle. On the other hand, the skewness and the asymmetry vary significantly as a result of the varying phase lags between the freely propagating component waves.

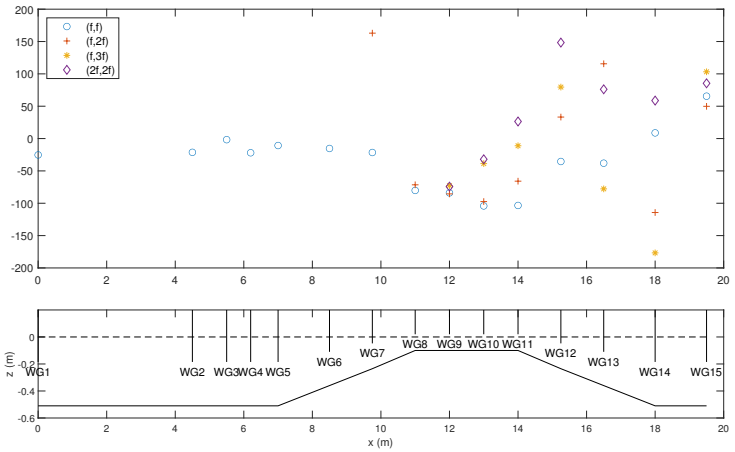

Figure 4.17: Biphase for selected frequency pairs; h=0.51m, H=3cm, T=2.5s.

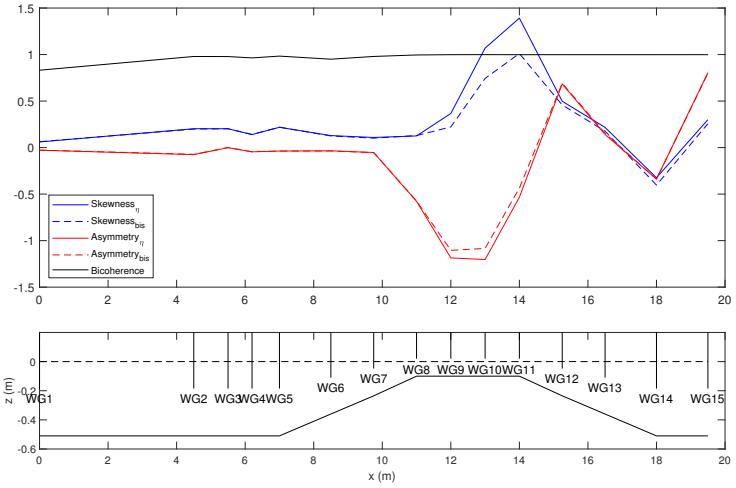

Figure 4.18: Spatial variation of indicators of nonlinearity in the physical wave flume; h=0.51m, H=3cm, T=2.5s. Solid lines: skewness and asymmetry from time series; dashed lines: skewness and asymmetry from bispectrum.

Now the results obtained for the previous monochromatic wave are compared to the results of the wave with T=1s and H=5cm, in order to compare the bispectra of waves with nearly the same height over the bar crest (similar nonlinear parameter ϵ') but different period. Here, the importance of the wave period over the generation and development of super-harmonics is investigated with the use of the bispectral analysis in order to give a more detailed description of the phenomena. As reported in Table 4.1 for h=0.51m, the wave with T=1s propagates over the bar in intermediate water depth while for T=2.5s the wave travels in shallow water conditions. At the toe of the structure (Figure 4.19) both waves present self-interactions of the first harmonic,

as shown by the values of the relative bispectra at $B(1,1)$ and $B(0.4,0.4)$. At station 8 (Figure 4.20) significant interactions start at the frequency pair $(f, 2f)$ and some energy is transferred from the first and the second harmonics to the third harmonic. The amplitude spectra of the two waves are still quite similar: the first harmonic remains dominant and the remaining energy is distributed to the second and the third harmonics. The situation totally changes in Figure 4.21 when waves travel over the bar. The wave with T=1s shows additional non-linear interactions only at $B(2,2)$ while for the longer wave the non-linear interactions involve a large number of higher harmonics which now have amplitudes comparable with the amplitude of the first harmonic. In fact, for T=2.5s the triplet resonance conditions are nearly satisfied and more energy is transferred to super-harmonics. At station 13, the shorter wave shows negative values of the imaginary part of the bispectrum and the energy is transferred back to lower frequencies. The result is that the changes in the amplitude spectrum are not as drastic with respect to the amplitude spectrum before the obstacle. For the wave with T=2.5s the non-linear interactions are still intense and they continue to involve numerous frequencies.

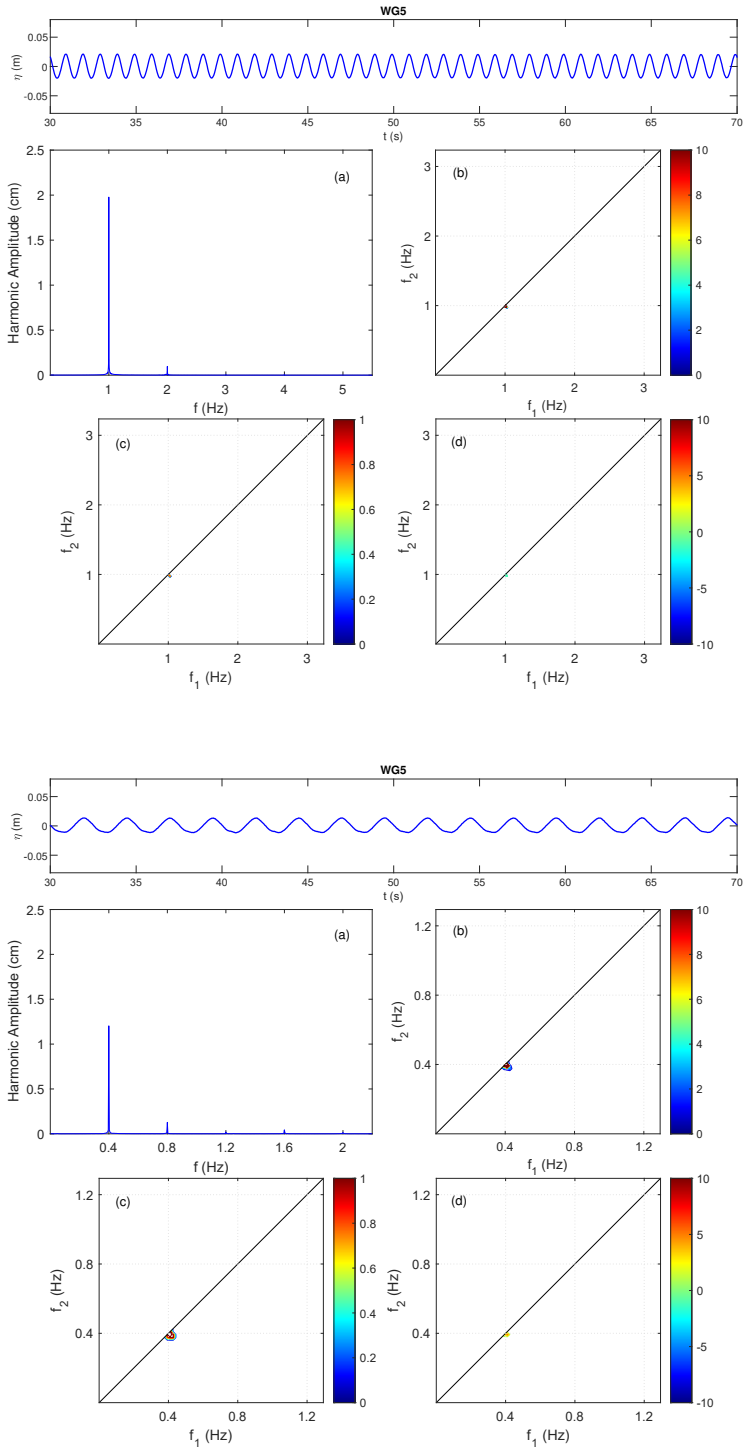

Figure 4.19: Amplitude spectrum (a), absolute bispectrum $|B|$ in cm^3/Hz^2 (b), bicoherence (c) and imaginary part of the bispectrum (x10^{-6}) (d) at station 5 for H=5cm, T=1s (upper panels) and H=3cm, T=2.5s (bottom panels); h=0.51m.

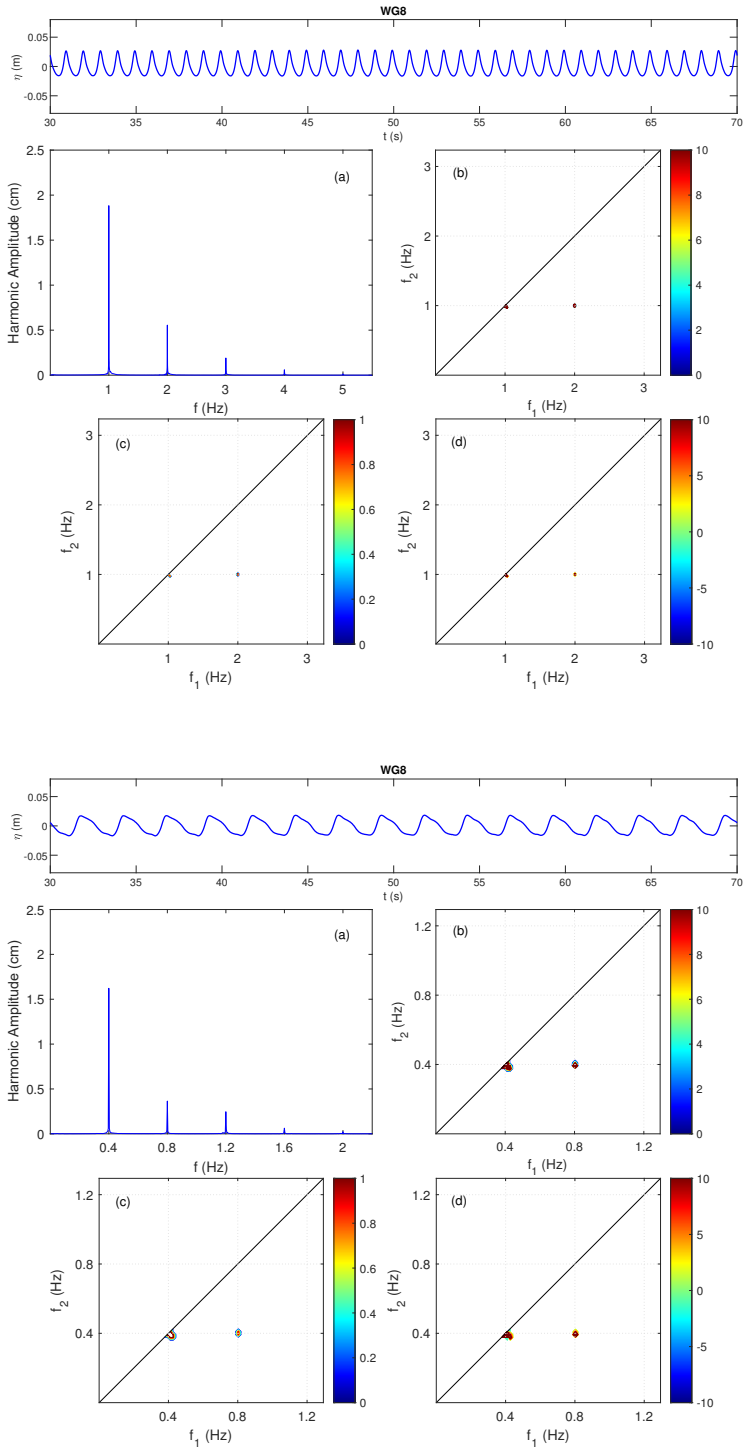

Figure 4.20: Amplitude spectrum (a), absolute bispectrum $|B|$ in cm^3/Hz^2 (b), bicoherence (c) and imaginary part of the bispectrum (x10^{-6}) (d) at station 8 for H=5cm, T=1s (upper panels) and H=3cm, T=2.5s (bottom panels); h=0.51m.

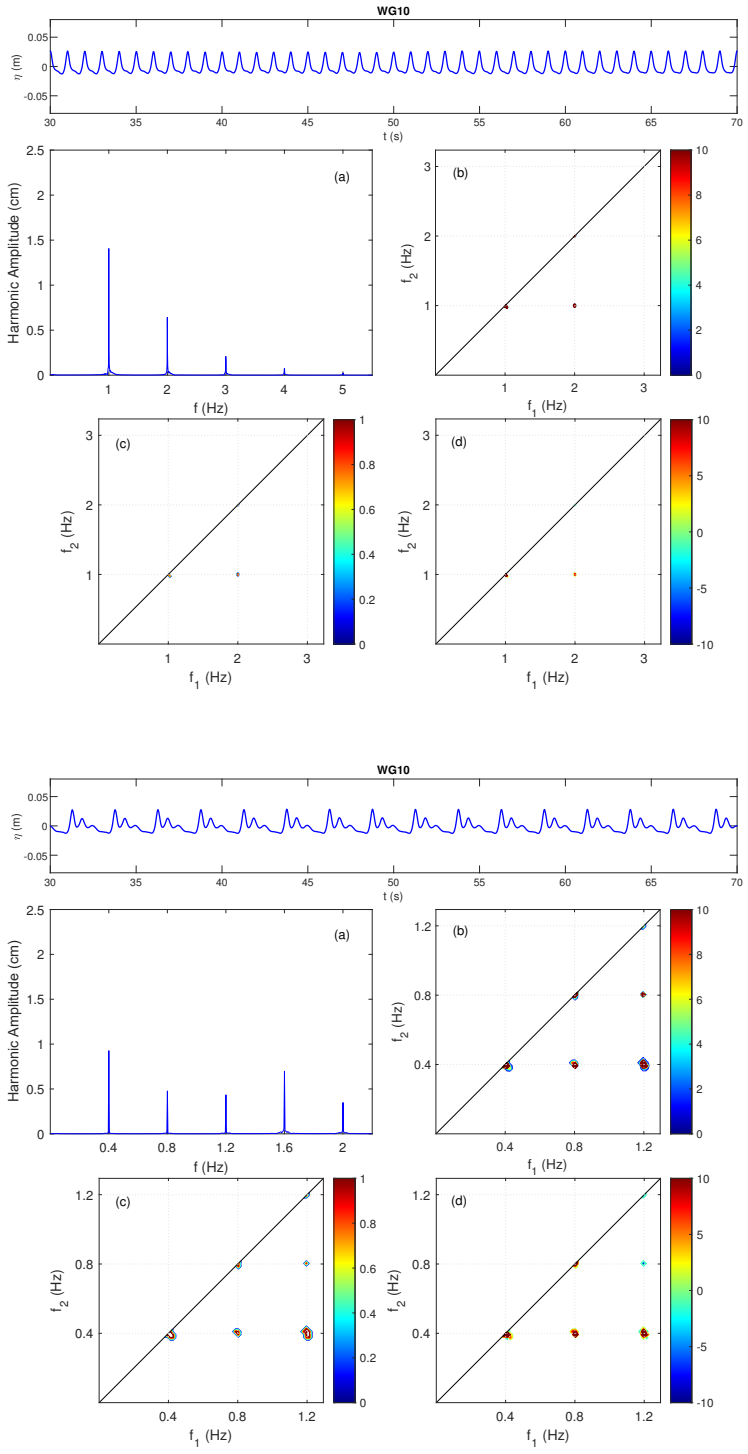

Figure 4.21: Amplitude spectrum (a), absolute bispectrum $|B|$ in cm^3/Hz^2 (b), bicoherence (c) and imaginary part of the bispectrum (x10^{-6}) (d) at station 10 for H=5cm, T=1s (upper panels) and H=3cm, T=2.5s (bottom panels); h=0.51m.

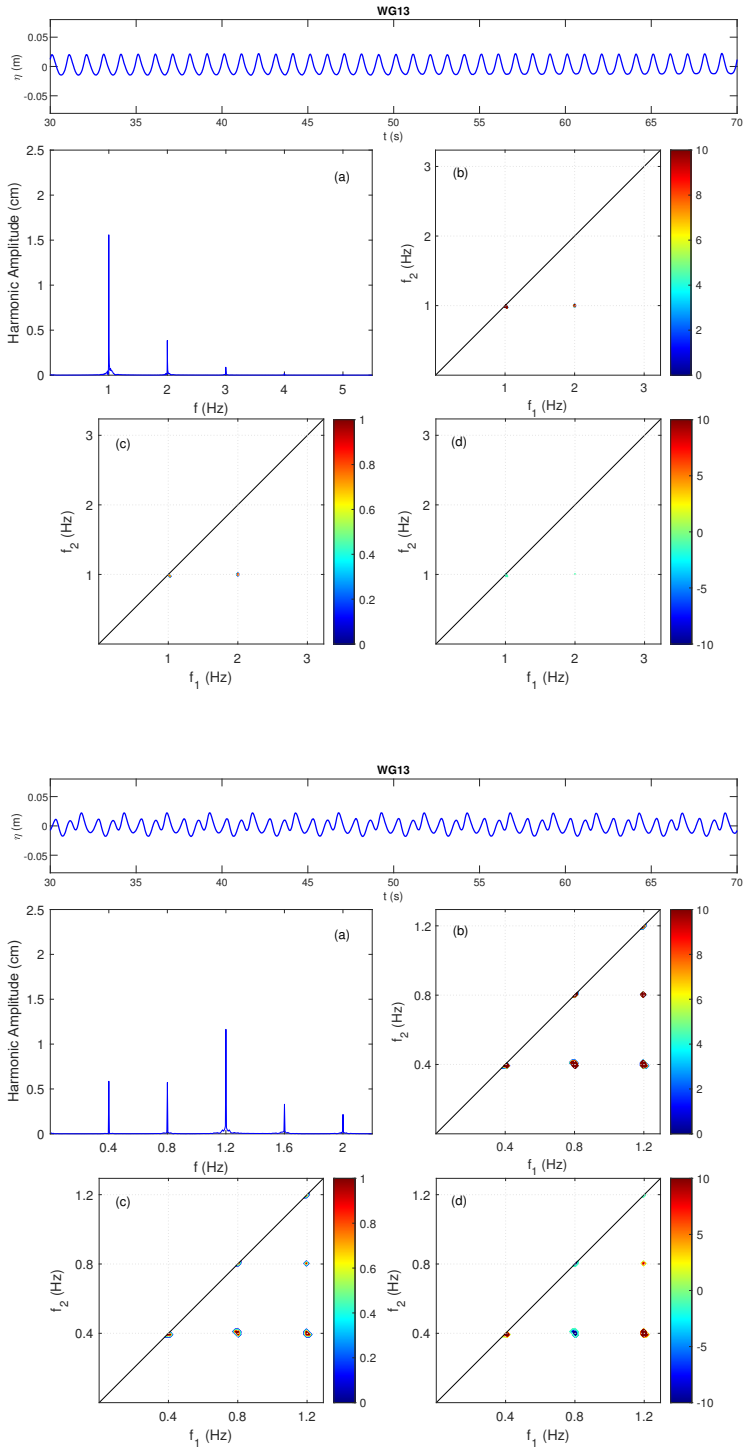

Figure 4.22: Amplitude spectrum (a), absolute bispectrum $|B|$ in cm^3/Hz^2 (b), bicoherence (c) and imaginary part of the bispectrum (x10^{-6}) (d) at station 13 for H=5cm and T=1s (upper panels) and H=3cm and T=2.5s (bottom panels); h=0.51m.

4.1.3 Random waves

The results of the spectral analysis applied to random waves are here presented. As already indicated in Section 3.2, irregular waves were generated as JONSWAP spectra with a peak enhancement factor equal to 3.3. 12 different random waves were tested, with two water depths, h=0.51m and h=0.56m. For each peak period, three significant wave heights were generated in order to have for h=0.51m non-breaking waves, spilling waves and plunging waves. As for monochromatic waves, the breaking criterium is based on visual observations. Waves with higher peak periods have smaller wave heights because the nonlinearity parameter ϵ is kept almost the same over the bar for all peak periods.
The effect of the wave period on the non-linear evolution of waves over the bar is evaluated by comparing the random waves with T_p=1s and T_p=2.5s. The influence of wave height and wave breaking is investigated with the comparisons of the spectral evolutions for the three different wave conditions for the same period. The characteristics of the selected waves are reported in Table 4.3 for h=0.51m and in Table 4.4 for h=0.56m. The values of H_s and T_p are those imposed at the wave generator, while ϵ' is the expected value of the nonlinearity parameter evaluated at the water depth h', over the bar crest, as $\epsilon' = a'_s/h'$ where $a' = H'_s/2$. The significant wave height H'_s over the bar has been estimated as $H'_s = H_s K_s$, where K_s is the shoaling coefficient for random waves computed as proposed by Goda (2010).

Table 4.3: Characteristics of the selected random waves for h=0.51m.

Name	h (m)	H_s (cm)	T_p (s)	f_p (Hz)	ϵ'
SpH5T10h51	0.51	5.0	1.0	1.0	0.25
SpH8T10h51	0.51	8.0	1.0	1.0	0.39
SpH12T10h51	0.51	12.0	1.0	1.0	0.39
SpH3T25h51	0.51	3.0	2.5	0.4	0.21
SpH5T25h51	0.51	5.0	2.5	0.4	0.36
SpH8T25h51	0.51	8.0	2.5	0.4	0.39

Table 4.4: Characteristics of the selected random waves for h=0.56m.

Name	h (m)	H_s (cm)	T_p (s)	f_p (Hz)	ϵ'
SpH5T10h56	0.56	5.0	1.0	1.0	0.16
SpH8T10h56	0.56	8.0	1.0	1.0	0.25
SpH12T10h56	0.56	12.0	1.0	1.0	0.37
SpH3T25h56	0.56	3.0	2.5	0.4	0.13
SpH5T25h56	0.56	5.0	2.5	0.4	0.22
SpH8T25h56	0.56	8.0	2.5	0.4	0.35

Figure 4.23 shows the power spectra for non-breaking (H_s=5cm), spilling (H_s=8cm) and plunging waves (H_s=12cm) with T_p=1s at three selected stations for the test configuration with h=0.51m. The measurements with the short waves (f_p=1.0Hz) reveal little spectral shape evolution over the obstacle. In fact, the spectral shape remains almost unchanged during the propagation and only a relatively small amount of high frequency energy is generated. The primary component of the wave train at frequency f_p remains prevalent during the propagation. At station 15 the energy transferred to higher frequencies ($f > 1.5f_p$) is about $15 - 17\%$ of the total transmitted wave energy. It is evident that the wave breaking acts by re-scaling the wave spectrum and the dissipation increases as the incident wave height increases.

The overall features of the spectral shape evolution do not differ substantially for these three wave conditions. Further clarification is offered in Figure 4.24, where the spatial variations of the normalized potential energy of the total, the primary and the higher frequency components are plotted. The primary wave energy is computed in the range of integration between 0.0Hz and 1.5Hz ($f_p + 0.5f_p$) while for the high-frequency energy the range is between 1.5Hz and 2.5Hz. The energy is negligible for frequencies higher than 2.5Hz. The total energy is obtained by adding the energy of the primary and the higher frequencies. In each case the energies are normalized with respect to the total energy measured at station 1. It can be seen that the high-frequency potential energy, with respect to the primary frequency one, develops independently of wave breaking. However, at station 15 the potential energy of higher frequencies increases from 14.9% of the total energy for the non-breaking wave to 17.0% for the spilling wave. For the plunging wave the percentage decreases to 15.0%.

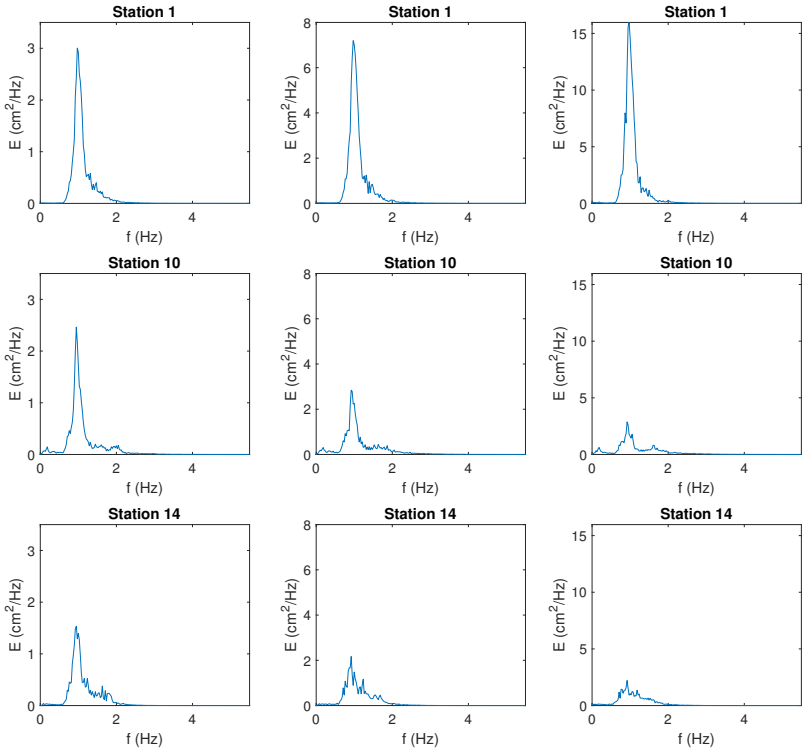

Figure 4.23: Spectral evolution for non-breaking (left), spilling (middle) and plunging (right) waves (JONSWAP incident spectrum, h=0.51m, f_p=1.0Hz).

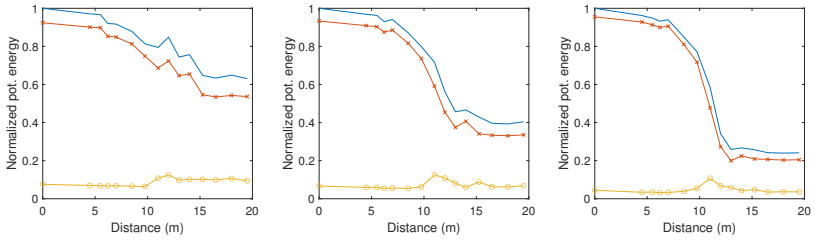

Figure 4.24: Spatial variations of normalized potential energy for non-breaking (left), spilling (middle) and plunging (right) waves (JONSWAP incident spectrum, h=0.51m, f_p=1.0Hz). (−) Total, (×) primary, (∘) higher frequencies. Distances are measured from station 1.

The spectral evolution of Figure 4.23 is now compared to the spectral evolution of the random waves with T_p=2.5s, for the same water depth of 0.51m (Figure 4.25). Even in this case the power spectra of non-breaking (H_s=3cm), spilling (H_s=5cm) and plunging waves (H_s=8cm) are shown at three stations along the wave flume. With respect to the previous case the spectral shape is completely modified by the non-linear interactions among frequency components over the structure. The result is that the initially narrow-banded spectra evolve in broader spectra leewards of the bar and about 80% of the energy is distributed among higher frequencies ($f > 1.5f_p$). At station 14, the non-breaking wave shows a multi-modal spectrum, where it is still evident the peak of the primary component at 0.4Hz but other peaks with comparable spectral density can be identified around frequencies multiple of the primary. For the breaking waves the peak at the primary frequency is strongly reduced by wave breaking and the energy is more uniformly distributed among higher frequencies, with less pronounced peaks.
The potential energy normalized with respect to the total potential energy at station 1 is plotted against distance in Figure 4.26. In computing the primary wave energy the range of integration is taken between 0.0Hz and 0.6Hz ($1.5f_p$), while for high-frequency energy it is between 0.6Hz and 2.5Hz. The spatial evolution of the high-frequency potential energy changes for the three wave conditions. For each case it starts to increase at about 10m from station 1 at the end of the upslope. The non-breaking wave is characterized by a potential energy at the higher frequencies that increases along the entire length of the submerged bar remaining almost constant at the last four stations (left panel of Figure 4.26). For the spilling and plunging waves, the growing trend is interrupted by wave breaking that occurs at the offshore edge of the horizontal crest located at 11m from station 1. The high-frequency energy of the spilling wave (middle panel of Figure 4.26) shows an almost constant stroke after breaking, it increases again at the onshore edge of the bar (at the distance of 14m from station 1) and then it remains constant. The more intense breaking of the plunging wave (right panel of Figure 4.26) leads to a drop also in the potential energy of higher frequencies followed by a slight increase on the downslope. At station 15, the potential energy of higher frequencies increases from 80.8% of the total energy for the non-breaking wave to 82.8% for the spilling wave. For the plunging wave the percentage decreases to 77.3%. As in the case of T_p=1.0s, the percentage of energy transferred to higher frequencies reaches a maximum for the spilling wave and then

it decreases for the plunging wave. This effect could be due to the fact that, in breaking conditions, as the wave height increases, an increasing amount of energy is also shifted toward lower frequencies, as shown below.

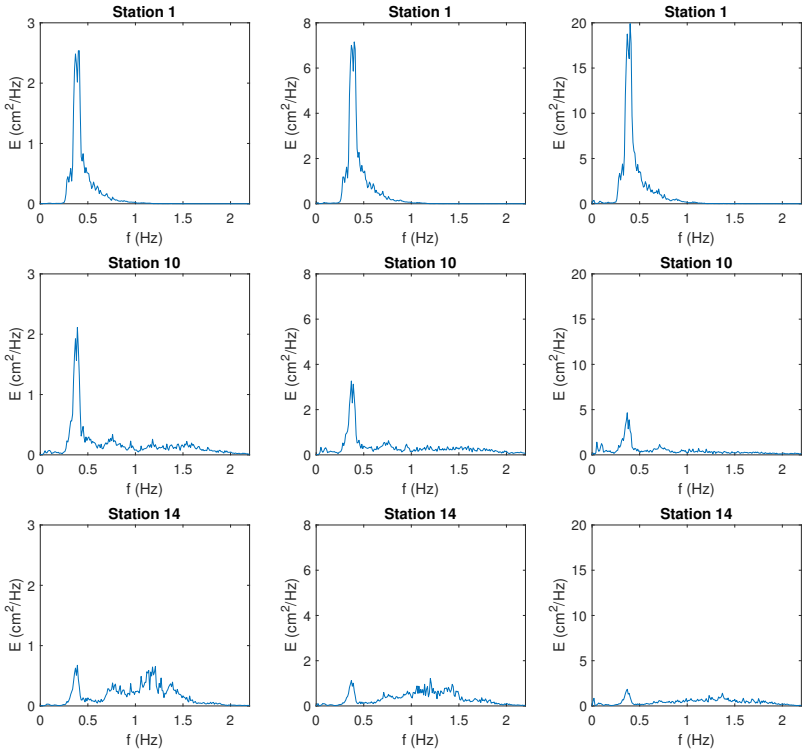

Figure 4.25: Spectral evolution for non-breaking (left), spilling (middle) and plunging (right) waves (JONSWAP incident spectrum, h=0.51m, f_p=0.4Hz).

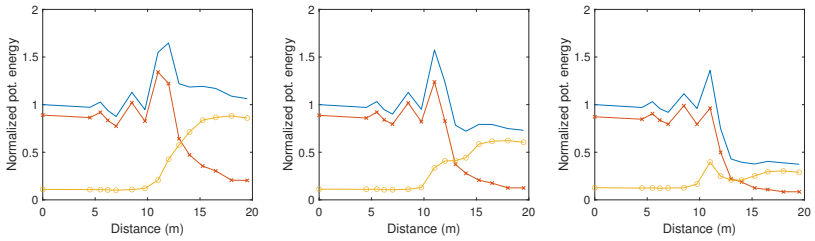

Figure 4.26: Spatial variations of normalized potential energy for non-breaking (left), spilling (middle) and plunging (right) waves (JONSWAP incident spectrum, h=0.51m, f_p=0.4Hz). (−) Total, (×) primary, (∘) higher frequencies. Distances are measured from station 1.

In order to make direct comparisons of spectral evolutions for different wave conditions, spectral estimates obtained at stations 7, 9, 11 and 14 for non-breaking and plunging breakers are normalized and plotted together. The normalization is such that the total area under the spectrum for every case is unitary. The results are shown in Figures 4.27, 4.28, 4.29 and 4.30 for the peak period T_p=1.0s. The spatial evolution of the spectral shape is similar for the non-breaking and the breaking waves. The normalized spectral density of both waves remains concentrated around the incident peak frequency f_p=1.0Hz but, after the occurrence of wave breaking for H_s=12cm, the spectral peak of the plunging wave is lower than that of the non-breaking wave over the bar crest and on the downslope side of the bar (at stations 9, 11 and 14). Furthermore, for the breaking wave more energy is transferred at frequencies lower that $0.5f_p$. This could be explained with the two main mechanisms of generation of infragravity waves (IGW). It is widely accepted that the generation of energy at IGW frequencies is caused by nonlinear interactions between wave triads composed by two closely spaced short wave (SW) frequencies and one IGW frequency. This is known as the *bound wave mechanism* (BWM) proposed by Longuet-Higgins and Stewart (1962) since it generates a forced IGW that propagates with the group velocity of the SW group. For breaking waves there is also another mechanism of generation of infragravity waves, *the breakpoint mechanism* (BKM). It is attributed to the time-varying displacement of the breakpoint location which induces a dynamic setup propagating both offshore and onshore from the breakpoint (Symonds et al., 1982). The IGW generated by the BKM propagate with their own celerity given by the dispersion relationship and therefore they can be considered free IGW. So, for the studied plunging wave both mechanisms act to generate infragravity waves and this in turn implies more energy at lower frequencies. This difference in the propagation of non-breaking and breaking waves is also observed for the other tested random waves with T_p=1.5s, T_p=2.0s and T_p=2.5s. As expected, it becomes less pronounced in the configuration with h=0.56m as the severity of wave breaking decreases.
Figures 4.31, 4.32, 4.33 and 4.34 show the comparisons between the spectra of the longest waves (T_p=2.5s). The shape of the normalized spectra is very similar for the non-breaking and the plunging waves during propagation over the upslope and at the beginning of the horizontal crest (stations 7 and 9), even if the wave breaking reduces the spectral peak of the primary component (station 9 in Figure 4.32) and it involves a greater amount of energy transferred at low frequencies, as previously observed for the shorter waves. At stations 11 and 14 the spectrum of the plunging wave differs from that of the non-breaking wave, because it has lower peaks at higher frequencies and the energy is distributed over a wider range of frequencies.

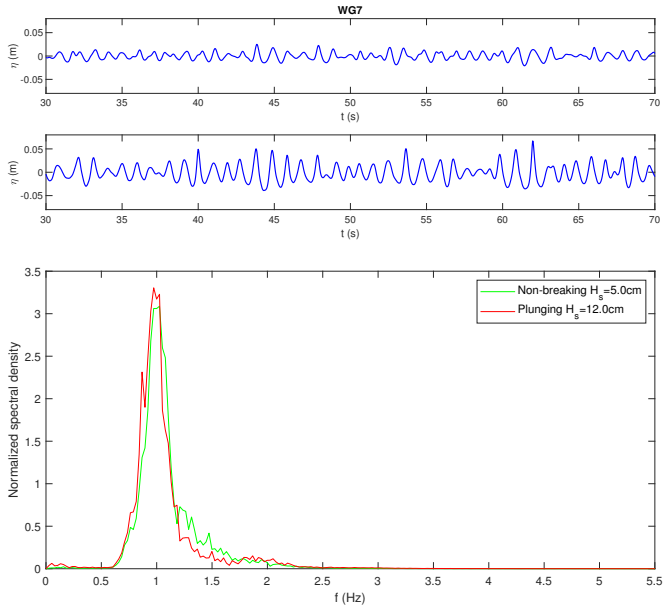

Figure 4.27: Comparisons of normalized spectra for non-breaking and plunging waves at station 7 (h=0.51m, f_p=1.0Hz).

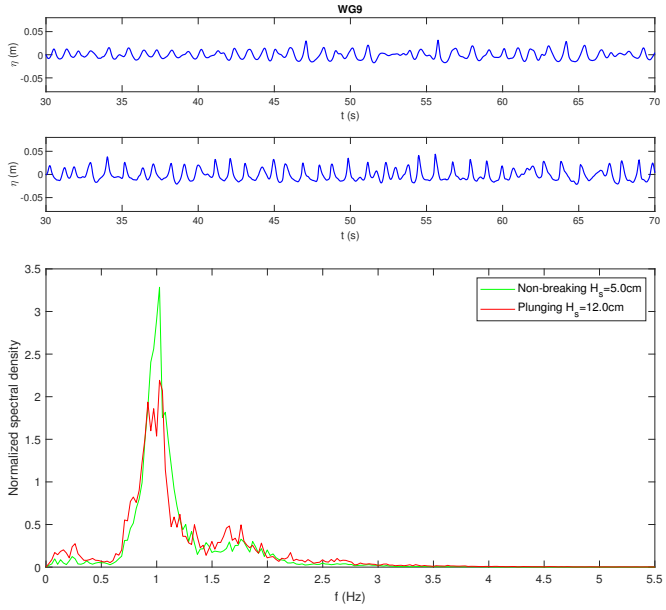

Figure 4.28: Comparisons of normalized spectra for non-breaking and plunging waves at station 9 (h=0.51m, f_p=1.0Hz)

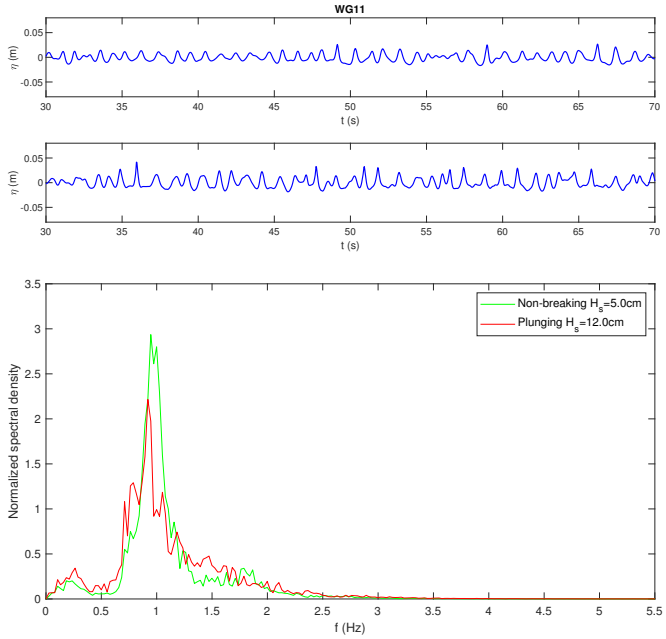

Figure 4.29: Comparisons of normalized spectra for non-breaking and plunging waves at station 11 (h=0.51m, f_p=1.0Hz)

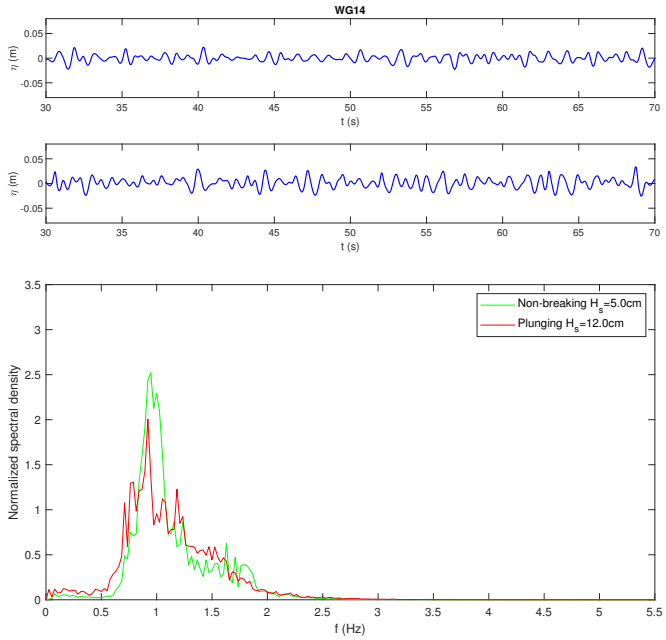

Figure 4.30: Comparisons of normalized spectra for non-breaking and plunging waves at station 14 (h=0.51m, f_p=1.0Hz)

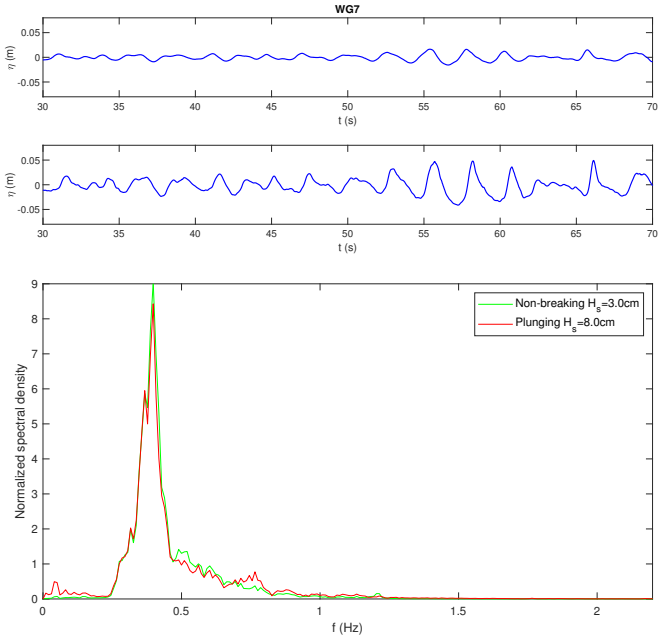

Figure 4.31: Comparisons of normalized spectra for non-breaking and plunging waves at station 7 (h=0.51m, f_p=0.4Hz).

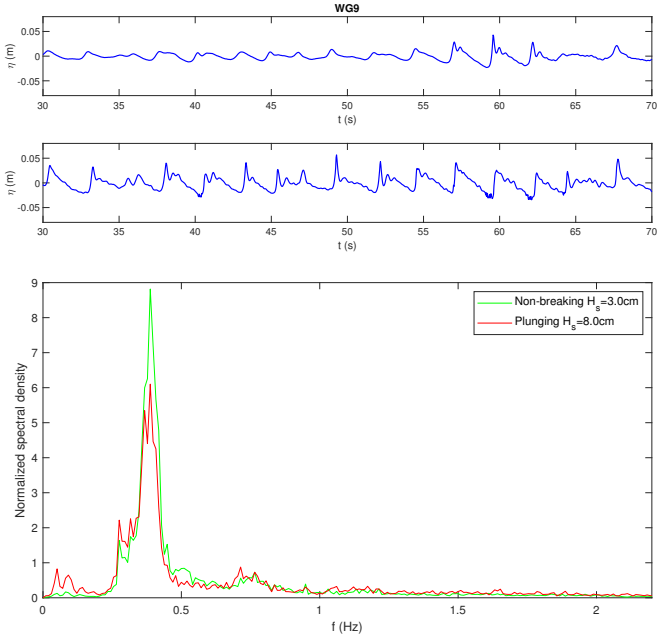

Figure 4.32: Comparisons of normalized spectra for non-breaking and plunging waves at station 9 (h=0.51m, f_p=0.4Hz)

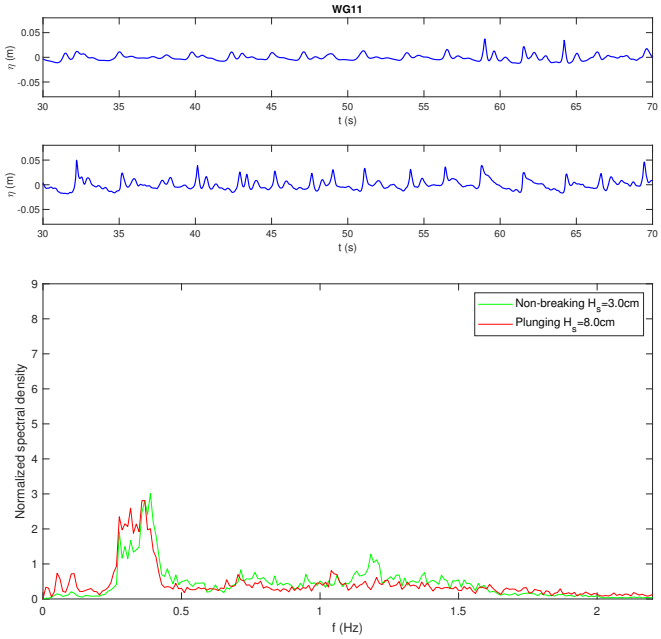

Figure 4.33: Comparisons of normalized spectra for non-breaking and plunging waves at station 11 (h=0.51m, f_p=0.4Hz)

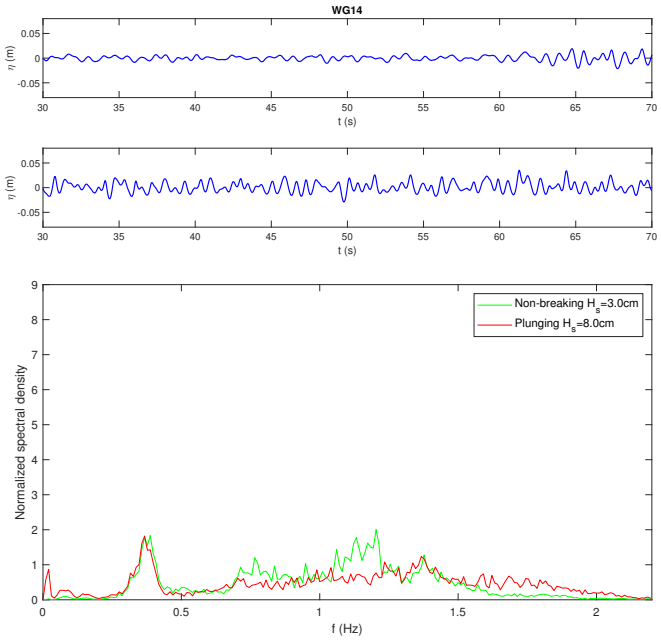

Figure 4.34: Comparisons of normalized spectra for non-breaking and plunging waves at station 14 (h=0.51m, f_p=0.4Hz)

4.1.4 Bispectral evolution of random waves

In this section the bispectral analysis is applied to random waves to determine the significant interactions that lead to harmonic generation and the influence of wave breaking on the intensity of the nonlinear couplings.
First of all, the evolution of the bispectra are shown for a specific case, the random wave with H_s=3.0cm, T_p=2.5s and h=0.51m. The bispectra are computed by dividing the record into equal segments, each of 4096 data resulting in a frequency resolution for the raw data of 0.0136Hz. The bispectral estimates are obtained by ensemble averaging over 24 segments. Figures 4.35 and 4.36 show the energy spectrum (a), the absolute values of the bispectrum (b), the values of the bicoherence (c) and the imaginary part of the bispectrum (d) at four stations along the wave flume. Noisy and spiky results from the bicoherence estimates have been suppressed by limiting the calculations to those frequency pairs for which the absolute value of the bispectral density exceeded 5% of the maximum value in the same bispectrum. The minimum bicoherence contour level is 0.1 with additional contours every 0.1.
The bispectrum at the toe of the structure (station 5) is shown in the upper (b) panel of Figure 4.35, in which a bispectral peak already exists at (0.4Hz, 0.4Hz). This peak indicates the self-interaction of the primary component at 0.4Hz with itself leading to the generation of the first super-harmonic at 0.8Hz. In fact, positive values of the imaginary part of the bispectrum (d) at B(0.4, 0.4) indicate a transfer from 0.4Hz to 0.8Hz. After propagation over the upslope of the bar (station 8), the bispectrum in the bottom (b) panel of Figure 4.35 shows amplification of the self-interaction peak of the primary. A less pronounced bispectral peak exists at (0.4Hz, 0.05Hz) which indicates phase-coupling between the primary and the low-frequency waves. This peak is attributed to the interactions between neighbouring primary waves. The resultant wave group forces a long wave at the difference frequency that is phase coupled to the group (Longuet-Higgins and Stewart, 1962). After propagation of an additional 2m over the horizontal crest (upper panels of Figure 4.36) other two bispectral peaks start to develop at (0.8Hz, 0.4Hz) and (1.2Hz, 0.4Hz), indicating interactions between the primary and its first and second super-harmonics resulting in energy transfer to the second and the third super-harmonics, respectively. At station 13 the bispectral peak at (0.4Hz, 0.4Hz) is reduced in intensity and the interaction involving infragravity frequencies (0.4Hz, 0.05Hz) disappears almost entirely. Difference interactions start to involve the second super-harmonic of the primary generating a new infragravity wave with frequency 0.07Hz. The interaction at (0.8Hz, 0.4Hz) becomes a negative interaction that transfers back energy from the sum frequency 1.2Hz to 0.8Hz and 0.4Hz. A similar behaviour was observed by Norheim (1998). They reported that simulations of waves propagating over a bar into deeper water showed a reversal in nonlinear energy transfers on the downslope section of the bar, with difference triad interactions transferring high-frequency energy back toward lower frequencies. Leewards of the structure the interactions slowly become weaker.
The values of the maximum bicoherence over the structure are shown in Figure 4.38. They vary from 0.51 at station 1, through a maximum of 0.97 at station 9, to 0.78 at station 15. The biphase has been computed from the bispectrum according to equation 2.15 for selected frequency pairs. These pairs represent the self-interactions of the primary denoted as (f_p, f_p), the interaction between the primary and the first and second super-harmonics denoted respectively as $(f_p, 2f_p)$ and $(f_p, 3f_p)$ and the self-interactions of the first super-harmonic $(2f_p, 2f_p)$. The variations of the biphases over the bar are plotted in Figure 4.37 when the corresponding absolute value of the

bispectrum exceeds 5% of the maximum value in the same bispectrum. At the first six stations the biphase of only the (f_p, f_p) interaction is shown; biphases of the other interactions are not plotted because little energy exists at the higher harmonics. The values of the biphase from station 1 to station 6 are close to zero and they imply Stokes-type waves with sharp crest and flat troughs. As the waves propagate over the bar, the biphases approach a value of $-\pi/2$ at station 9 implying a wave with a saw-toothed shape. Over the downslope of the bar the biphase-value of the (f_p, f_p) interaction gradually evolves to positive values. The biphases of the other harmonic interactions tend to be randomly scattered beyond the bar, so higher harmonics are largely released beyond the bar due to the decreasing nonlinearity. The overall nonlinearity parameters, skewness and asymmetry, have been calculated along the wave flume using both the time series (Equations 2.17 and 2.22) and the bispectrum (Equations 2.21 and 2.23). Their spatial variations in Figure 4.38 indicate that the absolute values of skewness and asymmetry increase significantly over the horizontal crest to a maximum. On the lee side of the bar, they decrease to near-zero values, comparable to those on the exposed side of the bar. This in turn means reduction of the nonlinear interactions on the down-wave side of the bar, unlike what happens for monochromatic waves.

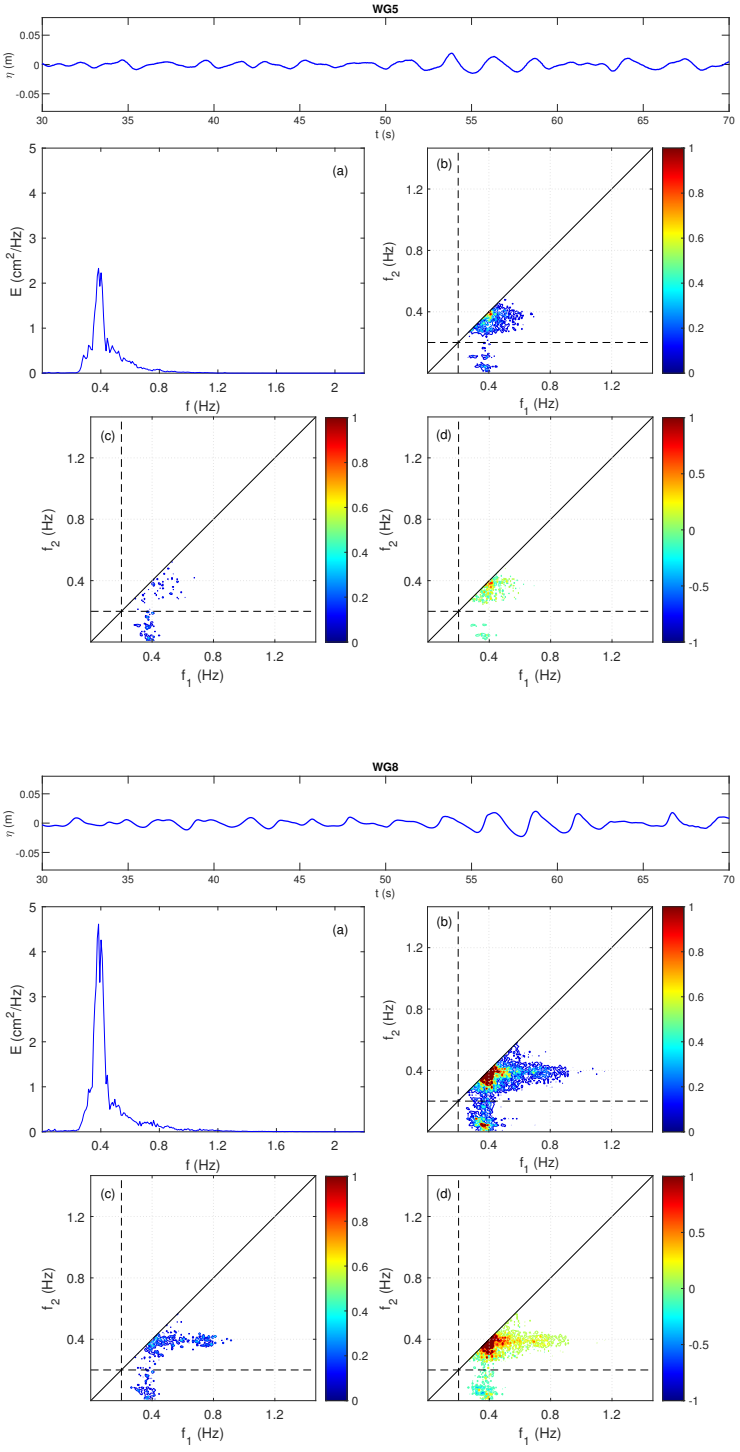

Figure 4.35: Energy spectrum (a), absolute bispectrum $|B|$ in cm^3/Hz^2 (b), bicoherence (c) and imaginary part of the bispectrum ($\times 10^{-6}$) (d) at station 5 (upper panels) and station 8 (bottom panels); h=0.51m, H_s=3cm, T_p=2.5s. Black dashed lines indicate the cutoff between infragravity and short-wave frequencies f_{IG}.

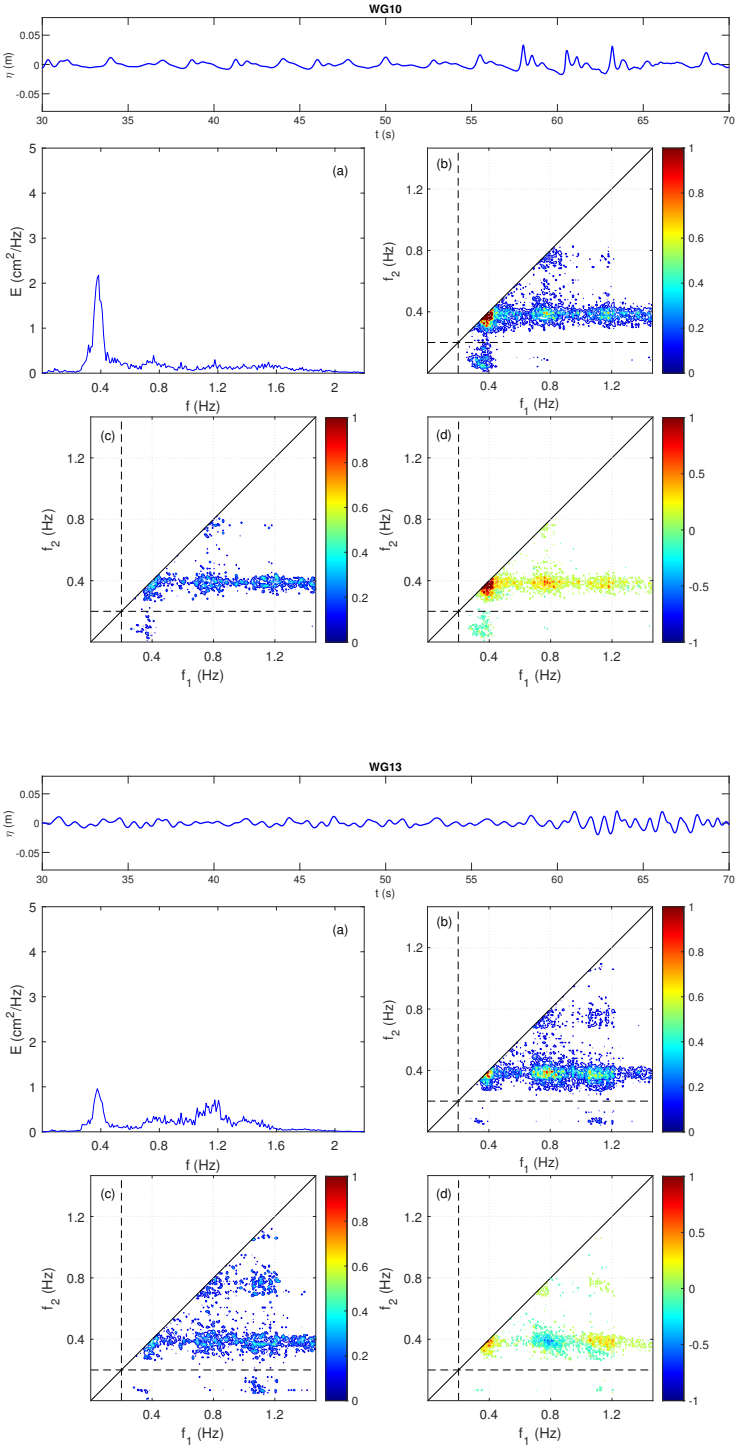

Figure 4.36: Energy spectrum (a), absolute bispectrum $|B|$ in cm^3/Hz^2 (b), bicoherence (c) and imaginary part of the bispectrum ($\times 10^{-6}$) (d) at station 10 (upper panels) and station 13 (bottom panels); h=0.51m, H_s=3cm, T_p=2.5s. Black dashed lines indicate the cutoff between infragravity and short-wave frequencies f_{IG}.

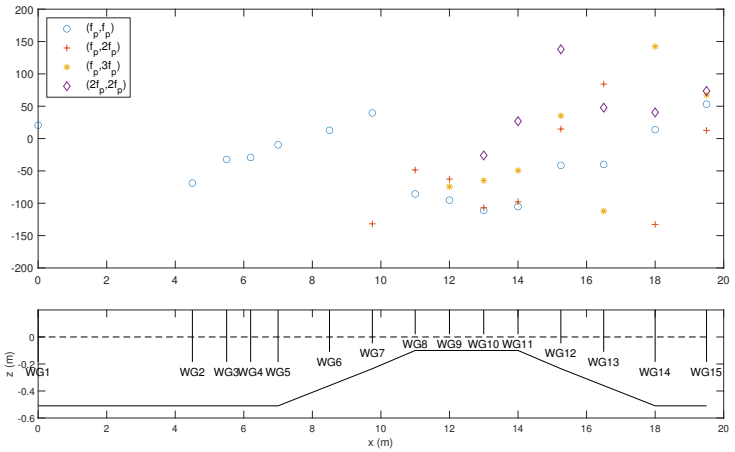

Figure 4.37: Biphase for selected frequency pairs in random wave propagating over the submerged bar; h=0.51m, H_s=3cm, T_p=2.5s.

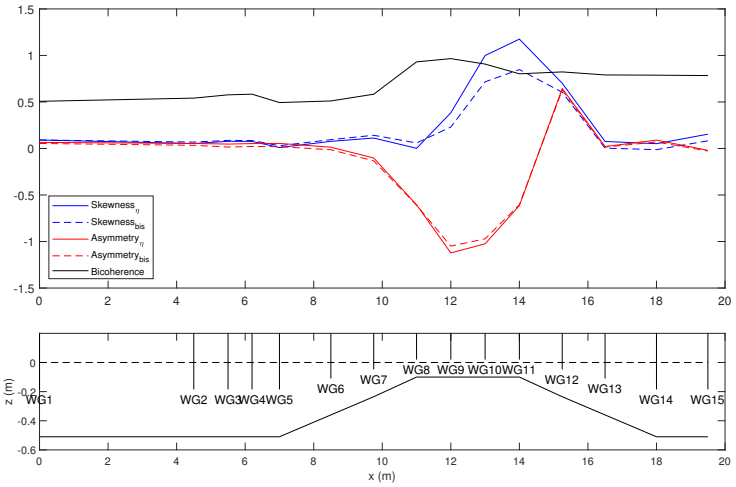

Figure 4.38: Spatial variation of indicators of nonlinearity in the physical wave flume; h=0.51m, H_s=3cm, T_p=2.5s. Solid lines: skewness and asymmetry from time series; dashed lines: skewness and asymmetry from bispectrum.

The previous analysis is relative to the case of a non-breaking wave. For spilling and plunging waves, wave breaking takes place as the wave field propagates into shallower water, leading to energy dissipation. The spectral and bispectral evolution of the plunging wave with H_s=8cm and T_p=2.5s is given in Figure 4.39 for the water depth h=0.51m. The absolute values of the bispectra show significant self-interactions of the primary waves near the spectral peak and interactions between these components and their harmonics, with intensity increasing on the upslope to a maximum at the offshore edge of the horizontal crest (station 8) and decreasing to low values in deep

water beyond the bar (stations 10 and 13). At station 5 and 8, the bispectral peaks at (0.4 Hz, 0.4Hz) and (0.4Hz, 0.05Hz) are higher than those computed for the non-breaking wave (Figure 4.35) and the nonlinear couplings at station 8 involve a greater number of multiple frequencies as a consequence of the increasing non-linearity related to the higher wave. The energy dissipation due to wave breaking strongly reduces the spectral energy at station 10 as well as the energy transfers between harmonic components. Over the bar all the bispectral peaks are significantly damped, particularly the peak generated by the self-interaction of the primary component at (0.4 Hz, 0.4Hz). Unlike the non-breaking wave for which the nonlinear interactions persist even on the leeside of the bar, for the plunging wave most of the bispectral regions show substantial reduction in their intensity and the nonlinear interactions almost disappear at station 13.

Since the bispectrum depends on the wave amplitude, conclusions about the influence of wave breaking on the nonlinear couplings require a measure of the nonlinear coupling that is independent of the wave amplitude. These considerations can be made using the normalized bispectrum, i.e. the bicoherence. The effect of wave breaking has been shown in Section 4.1.3 in terms of spectral analysis. Beji and Battjes (1993) concluded that for single-peaked incident wave spectra, the generation of high frequency energy and its transfer among wave components during the propagation across a shallow bar is hardly affected by wave breaking which acts as a secondary effect by simply re-scaling the wave spectrum. In accordance to Beji and Battjes (1993), the results of Section 4.1.3 confirm that the spectral shape keeps similar for non-breaking and plunging waves, even if wave breaking has been found to favour the generation of long waves and to redistribute energy over a wider range of higher frequencies. The evolution of the normalized energy spectra for the non-breaking and the plunging waves is plotted in Figure 4.40, together with the corresponding bicoherence values. The bicoherence has been calculated only for the frequency pairs for which the absolute value of the bispectral density exceeds 5% of the maximum value in the same bispectrum. Before wave breaking (station 7) and a little forward of the breaking point (station 9), the bispectral regions with significant values of the bicoherence are similar for the non-breaking (middle panels) and the breaking wave (right panels). At stations 11 and 14, the triad interactions of the plunging wave have lower bicoherence levels. They are also less concentrated around the frequencies multiple of the primary (which is more affected by the energy dissipation due to breaking) and they appear to be distributed over wider frequency ranges. Thus wave breaking reduces the intensity of the bispectral levels and it weakens the strength of the nonlinear couplings but it also involves a greater number of harmonic components in the interactions.

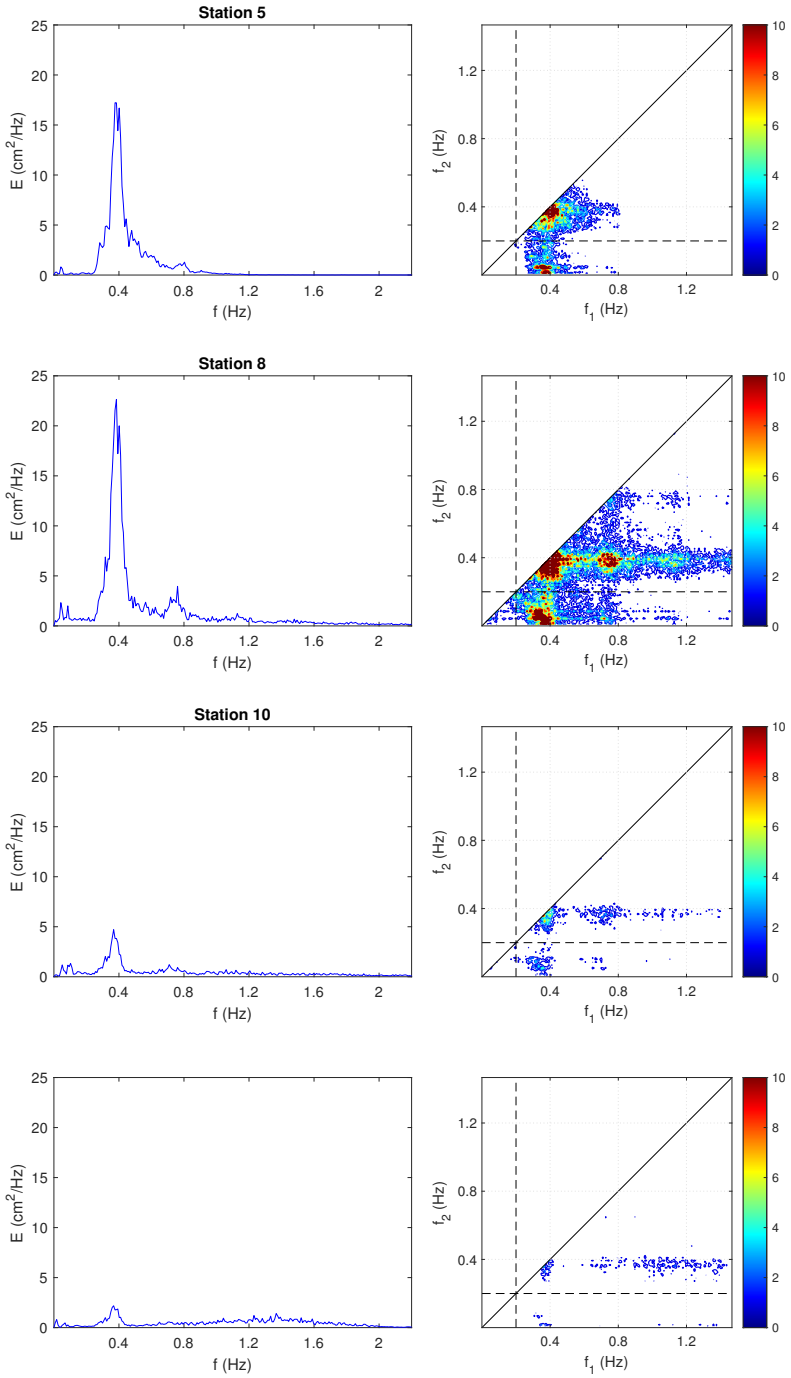

Figure 4.39: Energy spectrum (left panels) and absolute bispectrum $|B|$ in cm^3/Hz^2 (right panels) at station 5, 8, 10 and 13; h=0.51m, H_s=8cm, T_p=2.5s. Black dashed lines indicate the cutoff between infragravity and short-wave frequencies f_{IG}.

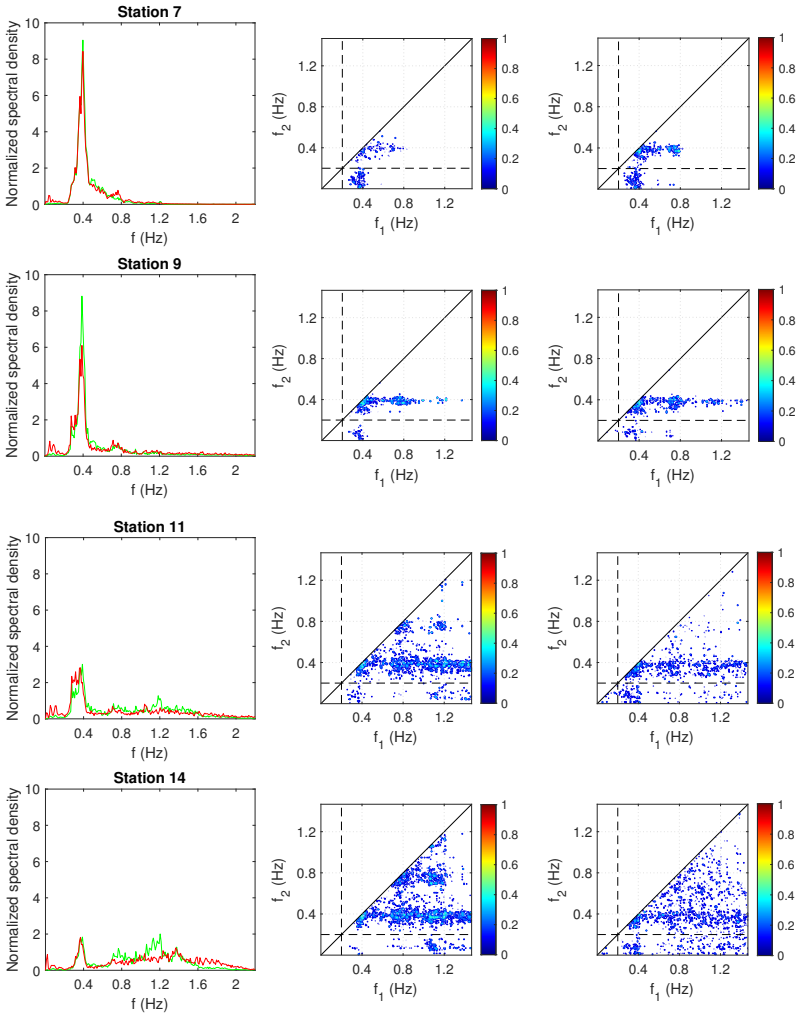

Figure 4.40: Comparisons of normalized energy spectra (left panels) for the non-breaking wave with H_s=3cm (green line) and the plunging wave with H_s=8cm (red line) at stations 7, 9, 11 and 14. Bicoherence for the non-breaking wave (middle panels) and for the plunging wave (right panels); JONSWAP incident spectrum, h=0.51m, T_p=2.5s.

The propagation of random waves over the submerged bar has been studied also by changing the test configuration with a grater water depth, in order to simulate the effect of a sea level rise. The influence of the increased water level on the phenomenon of harmonic generation has been evaluated by comparing the results of the spectral and bispectral analyses with the water depth h=0.56m and the results obtained in the previous configuration with h=0.51m. Figure 4.41 shows this comparison for the non-breaking wave with H_s=3cm and T_p=2.5s while Figure 4.42 is relative to the plunging wave with H_s=8cm and T_p=2.5s. By comparing waves with same height and period propagating over different water depths, it is possible to understand how the submergence of the bar affects the nonlinear couplings and thus the spectral evo-

lution. For the same wave, the increased submergence leads to a greater amount of transmitted energy leewards of the bar because the wave is less affected by the bottom friction. The wave with T_p=2.5s passes over the bar in shallow water conditions for h=0.51m and the interactions among triads become near-resonant. For h=0.56m the relative water depth reaches the limit of intermediate waters ($h/L \approx 0.05$) and the interaction process moves away from exact resonance. Figure 4.41 shows that for the non-breaking wave the departure from the resonant condition due to the increased water level leads to a reduction in the number of multiple frequencies involved in the interactions. This implies that the spectral peak of the primary component decreases less in terms of spectral density and smaller energy is shifted to higher frequencies at station 11 and 14. The plunging wave (Figure 4.42) breaks over the bar also with the higher water level but the intensity of wave breaking is reduced. This implies that more energy is available for the nonlinear interactions between harmonic components. Even if the wave train moves away from the resonance conditions for h=0.56m, bicoherence levels at multiple frequencies are higher at station 11 and 14 because the dissipation of the primary component due to breaking is less intense and it enhances strong coupling between specific frequencies.
By increasing the submergence for the breaking wave, the spectral peaks at higher frequencies result emphasized in the transmitted energy spectrum (station 14) and the maximum frequency with non-negligible spectral density is smaller. The submergence of the bar also influences the generation of low frequency waves in the energy spectra. The smallest water depth (green line) leads to more severe wave breaking which favours the development of infragravity waves according to the breakpoint mechanism.

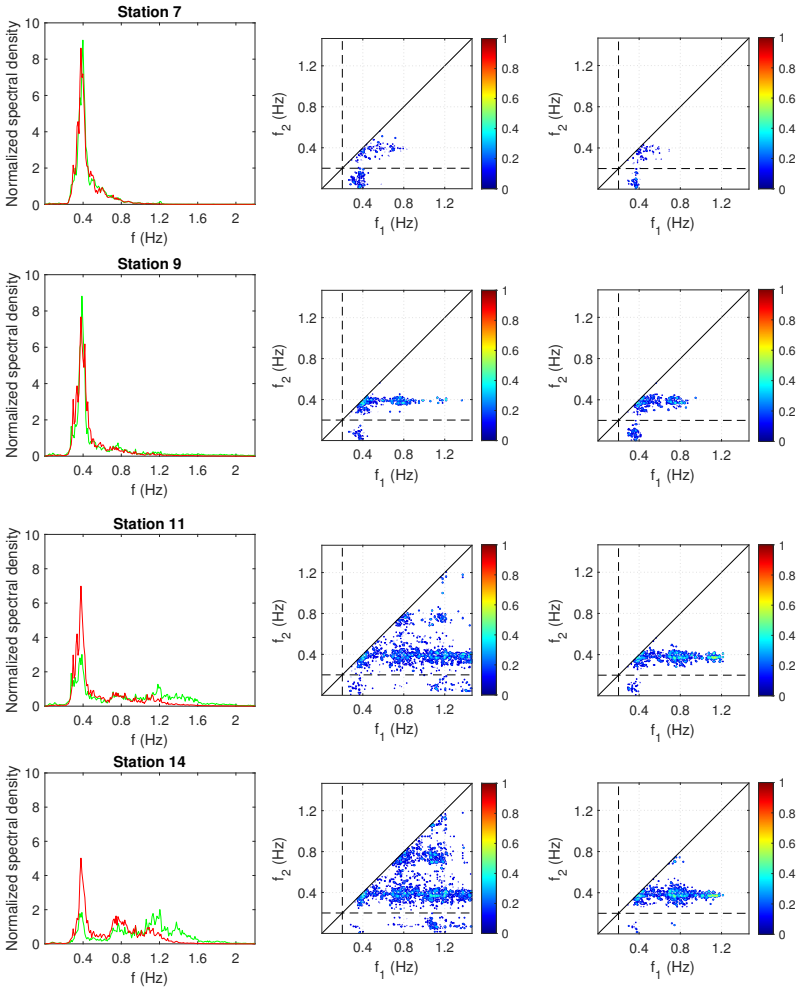

Figure 4.41: Comparisons of normalized energy spectra (left panels) for the random wave with H_s=3cm and T_p=2.5s in the configuration with water depth h=0.51m (green line) and in the configuration with h=0.56m (red line) at stations 7, 9, 11 and 14. Bicoherence for the random wave with the lower water level h=0.51m (middle panels) and with the higher water level h=0.56m (right panels).

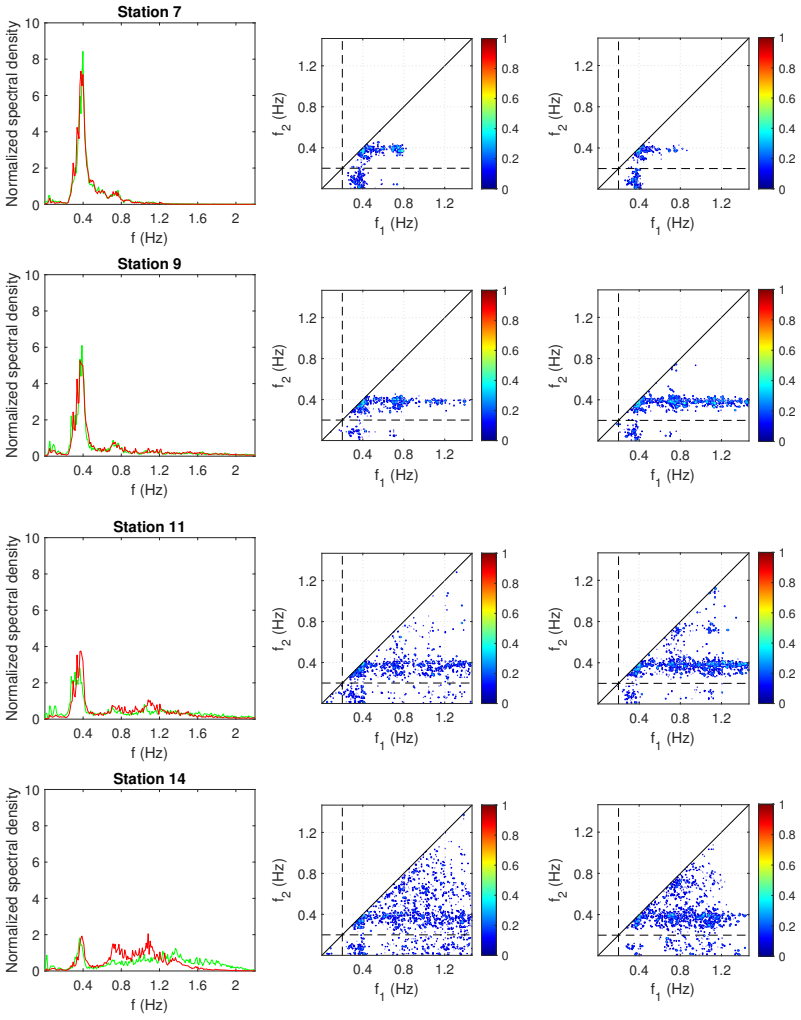

Figure 4.42: Comparisons of normalized energy spectra (left panels) for the random wave with H_s=8cm and T_p=2.5s in the configuration with water depth h=0.51m (green line) and in the configuration with h=0.56m (red line) at stations 7, 9, 11 and 14. Bicoherence for the random wave with the lower water level h=0.51m (middle panels) and with the higher water level h=0.56m (right panels).

4.2 Wave transmission of the submerged bar

In the previous section the spectral and bispectral analyses have been applied to investigate the effect of the nonlinear triad interactions that occur when waves pass over a submerged obstacle. In this section the wave transformation is studied in more general terms, by establishing the wave transmission coefficient, the ratio between transmitted and incident wave height. As seen in the previous section, the energy spectra undergo important changes due to the nonlinear wave-structure interaction which causes a transfer of wave energy from primary harmonics to higher harmonics of the wave spectrum. At first, the wave transmission has been evaluated for monochromatic and random waves by following a classical linear approach. A non-linear method for the evaluation of the transmission coefficients related to higher-order components of monochromatic waves is then proposed. For random waves, the energy content of the transmitted spectra has been evaluated for different frequency ranges, in order to verify if the transmitted wave spectrum can be predicted based only on the incident wave conditions and the structure geometry.

4.2.1 Monochromatic waves

The transmission process behind submerged structures is generally studied my means of a transmission coefficient, K_t. This parameter represents the wave energy transmitted behind the structure with respect to the incident energy and it can be evaluated as:

$$K_t = \sqrt{\frac{m_{0t}}{m_{0i}}} \tag{4.1}$$

where m_{0t} is the zero-order moment of the wave spectra in the protected area (transmitted) and m_{0i} is the zero-order moment of the incident wave spectra.
As a first attempt, the transmission coefficient of monochromatic waves has been evaluated from the zero-order moment of the wave spectra at station 15, $m_{0(15)}$, and that at station 1, $m_{0(1)}$. The results are shown in Figure 4.43 for all the tested monochromatic waves and both the water depths. In Figure 4.43 K_t is given as a function of the relative crest height $R_c/H_{m0(1)}$, where R_c is the structure freeboard (negative for submerged structures) and $H_{m0(1)}$ is the spectral wave height at station 1, calculated as $H_{m0(1)} = 4\sqrt{m_{0(1)}}$. The transmission coefficient linearly increases as $R_c/H_{m0(1)}$ decreases up to a maximum value of about 0.90 for $R_c/H_{m0(1)} \approx -2.2$. It remains almost constant for values $R_c/H_{m0(1)} < -2.2$. Four K_t values have been removed from the graph because they are greater than unity. K_t values greater than 1 correspond to the highest non-breaking waves with longer periods (T=2.0s and T=2.5s), for which the wave reflection from the 1:20 beach is not entirely negligible.

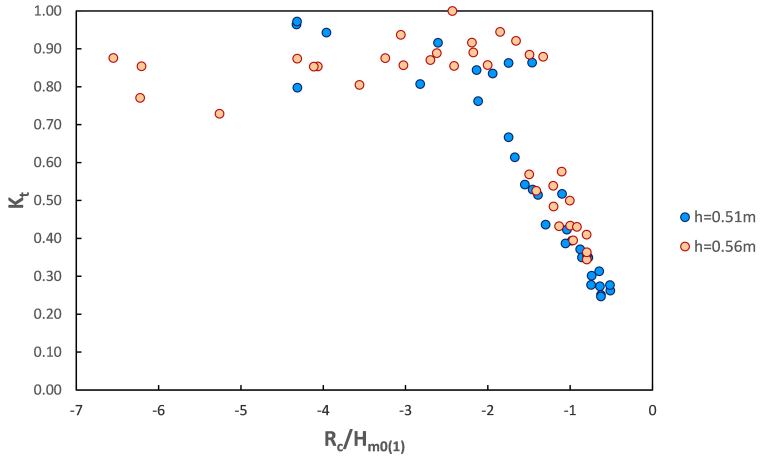

Figure 4.43: Transmission coefficient for monochromatic waves as a function of the ratio $R_c/H_{m0(1)}$.

Since the waves generated by the wave maker are partially reflected by the submerged structure, the method of Lin and Huang (2004) has been used to separate incident and reflected components for monochromatic waves. The method allows to isolate both the free and the locked modes in the higher harmonics. Therefore, the transmission coefficient has been also evaluated with the incident wave estimated by the method of Lin and Huang (2004). From the theory of signals, the variance of the signal m_0 can be evaluated as the half sum of the squares of the Fourier amplitudes C_n:

$$m_0 = \sigma^2 = \frac{1}{2}\sum_n C_n^2 \tag{4.2}$$

The incident and the transmitted energy has been computed with Equation 4.2, from the sum of the first five harmonic amplitudes, reconstructed with Lin and Huang (2004) on the sea side of the structure and separated from the transmitted signal at station 15. In Figure 4.44 the results of the transmission coefficient evaluated from Equation 4.2 are plotted against the ratio R_c/H_i, where H_i is the incident wave from the application of the Lin and Huang (2004)'s method. As in Figure 4.43, the transmission coefficient linearly increases for decreasing values of R_c/H_i and it reaches a maximum value of about 0.90 for $R_c/H_i \approx -3$, then it remains almost constant for values $R_c/H_i < -3$. It is noted that the absolute values of R_c/H_i are higher than the absolute values of $R_c/H_{m0(1)}$ because H_i is obviously smaller than the spectral wave height $H_{m0(1)}$ computed from the time series of the free surface at station 1. Also in Figure 4.44, four K_t values related to the longest and the highest non-breaking waves have been discarded because they are greater than 1.

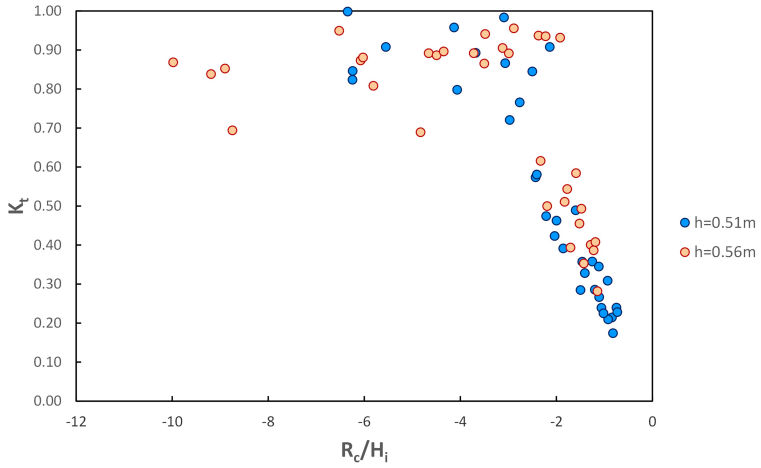

Figure 4.44: Transmission coefficient for monochromatic waves as a function of the ratio R_c/H_i.

The comparison between the transmission coefficient computed with the incident wave (Figure 4.44) and the transmission coefficient derived from the spectra at station 1 and station 15 (Figure 4.43) is shown in Figure 4.45. The values computed with the incident wave ($K_t(H_i)$) are comparable with the values computed from the spectra ($K_t(H_{m0(1)})$) with a squared correlation r^2=0.97 and a root mean squared error $rmse$=0.05. The difference between the two values increases for the test configuration with h=0.51m (r^2=0.96 and $rmse$=0.06). The small difference is due to the fact that the wave reflection from the submerged bar is small.

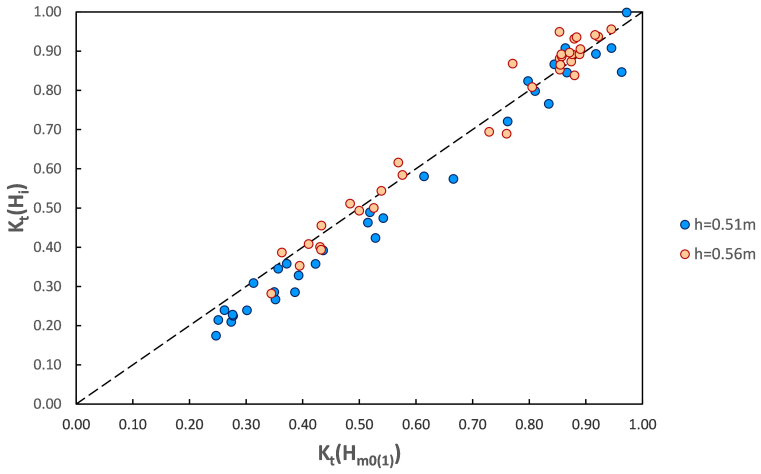

Figure 4.45: Comparison between the transmission coefficient evaluated from the incident wave $K_t(H_i)$ and the transmission coefficient evaluated from the spectra computed at station 1 and station 15 $K_t(H_{m0(1)})$.

As seen in the previous sections, the presence of the structure causes non-linear

interactions between harmonics and the generation of higher-order components. A non-linear method for the evaluation of the transmission coefficients related to higher-order components is proposed. These transmission coefficients are computed as:

$$K_{tn} = \sqrt{\frac{m_{0tn}}{m_{0i}}} \tag{4.3}$$

where m_{0tn} is the variance of the transmitted signal related to the harmonic amplitudes of order equal and higher than n, computed as:

$$m_{0tn} = \frac{1}{2} \sum_{j \geq n} C_{jt}^2 \tag{4.4}$$

where C_{jt} is the transmitted harmonic amplitude of order j. From Equation 4.3 it derives that K_{t1} coincides with the global K_t. In Figure 4.46 the values of K_t (or K_{t1}) are plotted as a function of R_c/H_i for different values of T and it results that the values of K_t do not depend from the wave period. Figures 4.47, 4.48, 4.49 and 4.50 show the transmission coefficients of higher-order components. The higher-order values of K_{tn} depends on the wave period and they increase for longer waves because the generation of super-harmonics is enhanced by larger wave periods. Furthermore, the higher-order transmission coefficients do not show a linear trend with the relative submergence, as instead shown by the global K_t. The values of K_{tn} increase as the incident wave height increases (or with increasing R_c), approximately until the wave breaking conditions are reached. The maximum values of K_{tn} correspond to different R_c/H_i, according to the wave period. Once the breaking has occurred, the transfer of energy to high-frequency harmonics is reduced (K_{tn} decreases) for higher R_c/H_i, suggesting a phenomenon of saturation of the amplitudes of these harmonics. This trend is more evident for K_{t2} (Figure 4.47) and K_{t3} (Figure 4.48). For K_{t4} (Figure 4.49) and K_{t5} (Figure 4.50), the longest waves (with T=2.0s and T=2.5s) still exhibit this behaviour, while waves with T=1.0s and T=1.5s have values of K_{tn} close to 0, because the shortest waves have a lower potential to generate fourth and fifth-order harmonics.

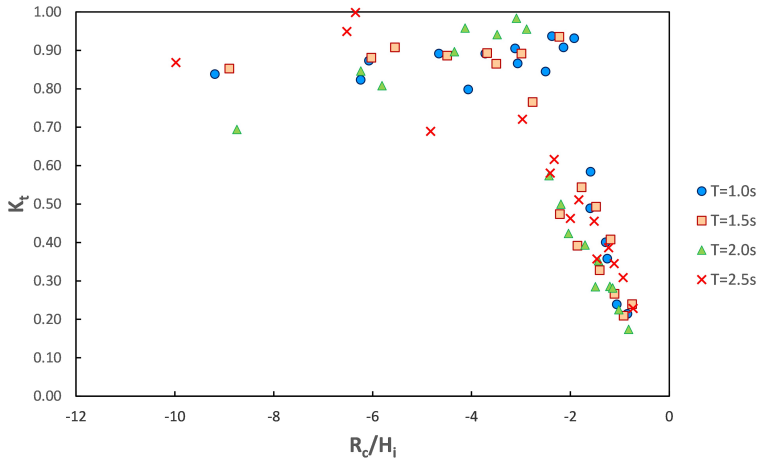

Figure 4.46: Transmission coefficient K_{t1} as a function of the ratio R_c/H_i for different wave periods.

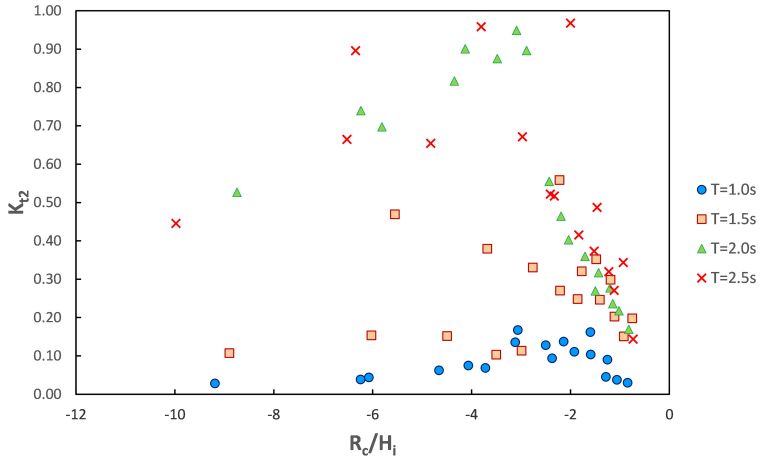

Figure 4.47: Transmission coefficient K_{t2} as a function of the ratio R_c/H_i for different wave periods.

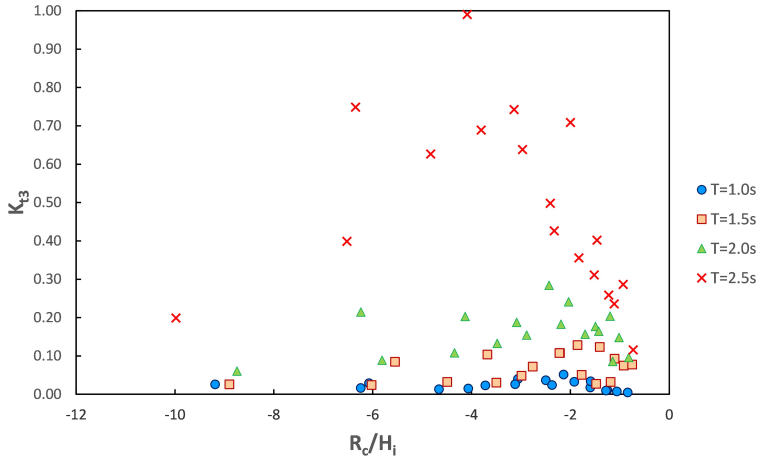

Figure 4.48: Transmission coefficient K_{t3} as a function of the ratio R_c/H_i for different wave periods.

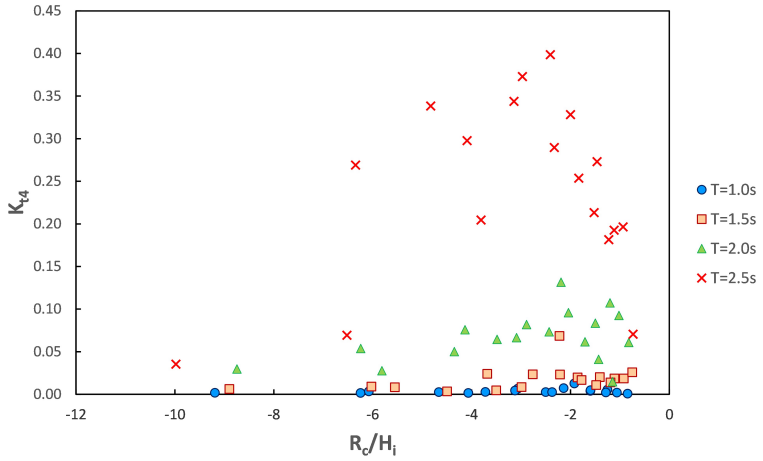

Figure 4.49: Transmission coefficient K_{t4} as a function of the ratio R_c/H_i for different wave periods.

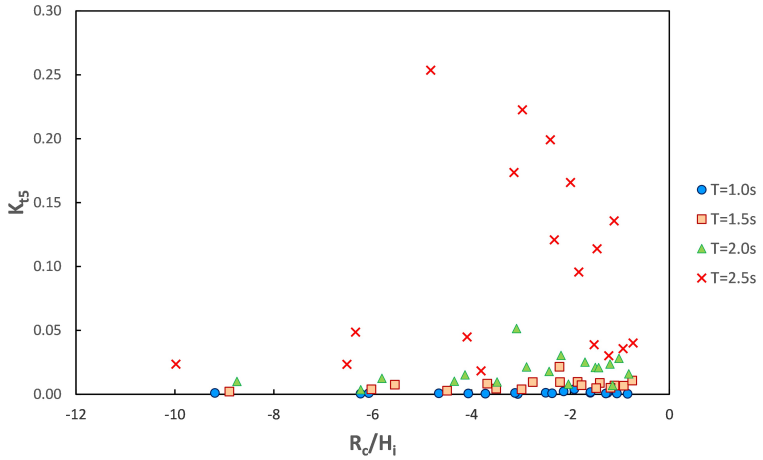

Figure 4.50: Transmission coefficient K_{t5} as a function of the ratio R_c/H_i for different wave periods.

4.2.2 Random waves

The transmission coefficient of random waves is evaluated from the ratio between the zero-order moments of the wave spectra at station 15 and at station 1. For random waves, wave record from gauge 1 is assumed to be an incident wave (indicated with the subscript i) and wave record from gauge 15 a transmitted one (with the subscript t). The values are plotted in Figure 4.51 against the ratio R_c/H_{m0i}, for both the water depths. For h=0.51m a value of K_t=1.02 is found related to the wave with H_s=3cm and T_p=2.5s and it has been removed from the graph. The trend observed in Figure 4.51 is similar to that obtained for monochromatic waves: K_t linearly increases as R_c/H_{m0i} decreases and it reaches a maximum value of about 0.9 at R_c/H_{m0i} ≈-3. For lesser values of R_c/H_{m0i} the transmission coefficient remains almost constant.

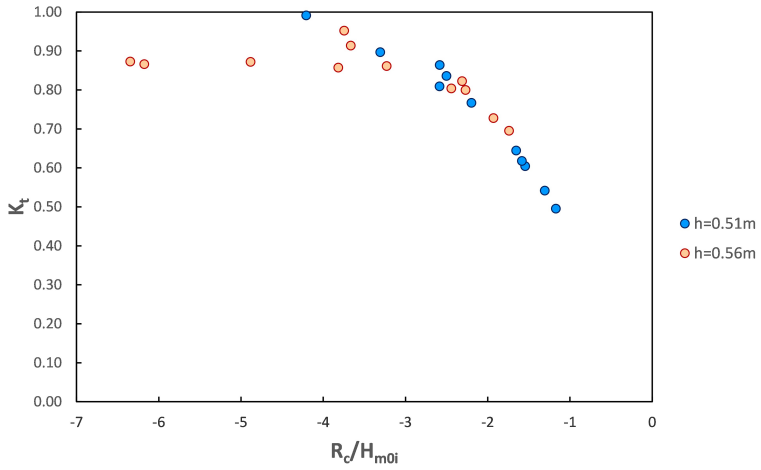

Figure 4.51: Transmission coefficient for random waves as a function of the ratio R_c/H_{m0i}.

For the laboratory tests of irregular waves, the measured parameters of the incident and the transmitted waves are summarized in Tables 4.5 and 4.6. The Tables also indicate the incident and the transmitted values of the mean spectral period T_m and of the peak period T_p. The mean spectral period is defined as $T_m = \sqrt{m_0/m_2}$ based on the spectral moments m_0 and m_2, where $m_n = \int_0^\infty f^n S(f) df$.

Table 4.5: Incident and transmitted wave parameters for random wave tests with R_c=-0.10m.

R_c=-0.10m						
Name	Incident			Transmitted		
	H_{m0i} (cm)	T_{02i} (s)	T_{pi} (s)	H_{m0t} (cm)	T_{02t} (s)	T_{pt} (s)
SpH5T10h51	3.8	0.9	1.0	3.1	0.8	1.0
SpH8T10h51	6.0	0.9	1.0	3.9	0.8	1.1
SpH12T10h51	8.5	0.9	1.0	4.2	0.8	1.1
SpH4T15h51	3.0	1.3	1.5	2.7	0.9	1.6
SpH6T15h51	4.5	1.3	1.5	3.5	0.9	0.9
SpH10T15h51	7.6	1.3	1.5	4.1	0.8	0.9
SpH3T20h51	2.4	1.5	2.0	2.3	1.0	1.0
SpH5T20h51	4.0	1.5	2.0	3.3	0.9	1.1
SpH8T20h51	6.4	1.5	2.0	3.9	0.8	1.0
SpH3T25h51	2.3	1.8	2.4	2.3	0.9	0.8
SpH5T25h51	3.9	1.8	2.5	3.3	0.8	0.8
SpH8T25h51	6.3	1.8	2.5	3.9	0.8	2.7

Table 4.6: Incident and transmitted wave parameters for random wave tests with R_c=-0.15m.

R_c=-0.15m						
Name	Incident			Transmitted		
	H_{m0i} (cm)	T_{02i} (s)	T_{pi} (s)	H_{m0t} (cm)	T_{02t} (s)	T_{pt} (s)
SpH5T10h56	3.9	0.9	1.0	3.3	0.9	1.0
SpH8T10h56	6.1	0.9	1.0	4.9	0.9	1.0
SpH12T10h56	8.6	0.9	1.0	5.2	0.9	1.1
SpH4T15h56	3.1	1.2	1.5	2.7	1.2	1.5
SpH6T15h56	4.6	1.3	1.5	4.0	1.1	1.6
SpH10T15h56	7.7	1.3	1.5	5.6	1.0	1.6
SpH3T20h56	2.4	1.4	2.0	2.1	1.1	2.0
SpH5T20h56	4.1	1.5	2.0	3.7	1.1	2.0
SpH8T20h56	6.6	1.6	2.0	5.3	1.0	1.1
SpH3T25h56	2.4	1.6	2.6	2.1	1.2	2.5
SpH5T25h56	4.0	1.9	2.6	3.8	1.1	2.5
SpH8T25h56	6.5	1.9	2.6	5.3	1.0	0.9

As seen in Section 4.1.3, the energy spectra tend to undergo important changes due to the non-linear wave-structure interaction which tends to shift the energy content toward higher and lower frequencies.
The model for the calculation of spectral changes was first studied by van der Meer et al. (2000) on emerged low-crested structures. Based on measurements, they developed a simple model for calculating transmitted energy spectra where it is assumed that 40% of all transferred energy is positioned at higher frequencies (between $1.5f_p$ and $3.5f_p$) and 60% of spectrum energy at lower frequencies ($< 1.5f_p$). In the work of van der Meer et al. (2005) this model was experimentally confirmed on emerged and submerged structures and much wider ranges of spectral change parameters were given. It was therefore suggested that the energy at higher frequencies can vary between 30 and 60% and the range of higher frequencies is between $1.5f_p$ and 2.9-$5.6f_p$. The assumption of this model is that energy transfer to higher harmonics is independent of incident wave parameters and breakwater geometry. Carevic et al. (2013) proposed an improvement of the van der Meer et al. (2000) model based on the conclusion that the energy fraction transferred to high frequencies is variable with the structure submergence and reaches the value of 40% when the breakwater crest

is around the water level. The process of wave transmission and spectral change over a permeable low-crested breakwater is also described in Lamberti et al. (2007) and Zanuttigh and Martinelli (2008). The authors developed an analytical model for emerged low-crested breakwaters able to predict transmitted wave spectrum based only on incident wave conditions and structure geometry.
For all the tested random waves, the energy content of the transmitted spectra is calculated at different frequency ranges in terms of the area of the spectrum m_{0t}. The frequency ranges are: $f \leq 0.5f_p$, $f \geq 1.5f_p$, $1.5 - 2.5f_p$, $2.5 - 3.5f_p$ and $f \geq 3.5f_p$. Table 4.7 shows the energy m_{0t} for each frequency range with respect to the total energy of the transmitted spectrum. The submergence of the structure crest and the peak period of the incident wave are the parameters with the greatest influence on the spectral change. If the submergence increases, the energy transfer toward lower and higher frequency decreases for the same wave period and height. For similar values of the nonlinear parameter ϵ measured at station 8 (indicated in Tables as ϵ'), the transfer of energy at higher frequencies tends to increase with the peak period, while for the same peak period the energy at higher frequencies does not show a growing trend with the wave height. Instead, the amount of energy transferred to frequencies lower than $0.5f_p$ is mainly influenced by the wave height and it increases for higher waves for the same peak period.

Table 4.7: Energy content of the transmitted spectra at different frequency ranges.

R_c=-0.10m							
H_s (cm)	T_p (s)	ϵ'	m_{0t} (%) $(0 - 0.5f_p)$	m_{0t} (%) $(f \geq 1.5f_p)$	m_{0t} (%) $(1.5 - 2.5f_p)$	m_{0t} (%) $(2.5 - 3.5f_p)$	m_{0t} (%) $f \geq 3.5f_p$
5.0	1.0	0.18	2.00	15.83	15.12	0.46	0.24
8.0	1.0	0.27	3.70	17.27	16.49	0.62	0.16
12.0	1.0	0.34	4.97	15.68	14.80	0.69	0.19
4.0	1.5	0.17	1.60	45.93	39.25	6.24	0.44
6.0	1.5	0.25	2.05	53.04	44.07	8.21	0.76
10.0	1.5	0.37	3.90	59.48	48.99	9.11	1.38
3.0	2.0	0.14	0.97	71.00	54.30	13.98	2.72
5.0	2.0	0.23	1.46	77.27	48.70	23.35	5.22
8.0	2.0	0.35	3.45	78.32	39.32	29.79	9.21
3.0	2.5	0.14	0.88	79.94	24.59	39.99	15.36
5.0	2.5	0.24	1.57	82.74	21.59	36.38	24.77
8.0	2.5	0.37	4.74	77.16	17.92	29.50	29.74
R_c=-0.15m							
H_s (cm)	T_p (s)	ϵ'	m_{0t} (%) $(0 - 0.5f_p)$	m_{0t} (%) $(f \geq 1.5f_p)$	m_{0t} (%) $(1.5 - 2.5f_p)$	m_{0t} (%) $(2.5 - 3.5f_p)$	m_{0t} (%) $f \geq 3.5f_p$
5.0	1.0	0.12	0.80	8.92	8.43	0.29	0.21
8.0	1.0	0.18	1.93	7.47	6.96	0.33	0.18
12.0	1.0	0.24	2.77	6.53	6.09	0.32	0.12
4.0	1.5	0.11	1.10	19.42	18.36	0.83	0.24
6.0	1.5	0.16	1.83	23.90	22.29	1.31	0.31
10.0	1.5	0.26	2.81	34.37	31.03	2.88	0.46
3.0	2.0	0.09	0.68	44.64	41.10	3.16	0.38
5.0	2.0	0.15	1.19	58.30	51.18	6.48	0.64
8.0	2.0	0.24	1.90	64.50	51.66	10.99	1.86
3.0	2.5	0.08	0.73	53.93	34.18	18.06	1.68
5.0	2.5	0.15	1.08	72.63	37.64	30.64	4.35
8.0	2.5	0.24	1.93	77.69	34.97	34.43	8.28

Figure 4.52 presents the amount of energy shifted toward higher frequencies in the transmitted spectrum, expressed by the parameter $m_{0t1.5}/m_{0t}$, as a function of the relative freeboard R_c/H_{m0i}. The ratio $m_{0t1.5}/m_{0t}$ represents how much energy

is positioned on frequencies $f > 1.5f_p$ with respect to the total transmitted energy. For emerged low-crested structure van der Meer et al. (2000) showed that a constant ratio $m_{0t1.5}/m_{0t}$ of 0.4 is found for transmission coefficients $K_t > 0.15$. For the submerged structure of this experimental campaign, it is clear that $m_{0t1.5}/m_{0t}$ varies from about 0.1 to 0.8 and it is correlated with R_c/H_{m0i}. The colours of Figure 4.52 are associated to different values of the nonlinear parameter ϵ'. The relation between $m_{0t1.5}/m_{0t}$ and R_c/H_{m0i} is approximated as linear for the same value of ϵ' with a lower limit at $m_{0t1.5}/m_{0t}$=0.076, which corresponds to the average value of the three lowest positioned dots. The interpretation of Figure 4.52 is not so immediate because the value of ϵ' in turn depends on the ratio R_c/H_{m0i}. For a fixed R_c and decreasing values of H_{m0i}, the ratio R_c/H_{m0i} decreases and the energy shifted to higher frequencies increases for the same ϵ'. In fact, even if the incident wave height is smaller, the increase in the wave period to maintain the same value of ϵ' causes a greater energy transfer to higher frequencies. Therefore, the parameter ϵ' measured over the bar has a great influence on the spectral change because it indirectly depends on the incident peak period. The ratio $m_{0t1.5}/m_{0t}$ varies in the range 0.1-0.8 but this variation is obtained within a smaller range of R_c/H_{m0i} for increasing values of ϵ'.

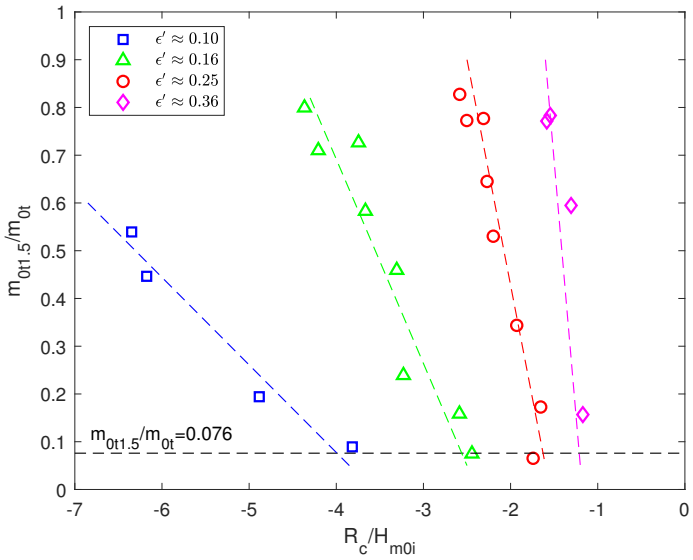

Figure 4.52: Ratio between the transmitted energy for frequencies $f > 1.5f_p$ and the total transmitted energy plotted versus the relative submergence R_c/H_{m0i} for different values of the nonlinear parameter ϵ'.

In order to determine where the transfer of energy to higher frequencies starts, the parameter named energy distribution parameter (e.d.p.) defined by Briganti et al. (2004) is used:

$$e.d.p. = \left[\left(\frac{m_{0t1.5}}{m_{0t}}\right) - \left(\frac{m_{0i1.5}}{m_{0i}}\right)\right] / \left(\frac{m_{0i1.5}}{m_{0i}}\right) \tag{4.5}$$

where $m_{0i1.5}/m_{0i}$ is the incident spectral energy for frequencies larger than $1.5f_p$ with respect to the total incident energy.
The e.d.p. describes the variation of the amount of energy associated to $f > 1.5f_p$

between the incident and the transmitted spectra. The e.d.p. is positive if energy is transferred towards $f > 1.5f_p$ and zero if no energy transmission occurs. Figure 4.53 shows the relation of the e.d.p. and the parameter R_c/H_{m0i}. The lowest three dots represent the waves from Table 4.7 with the smallest peak period ($T_p = 1s$) and R_c=-0.15m. These three values are around zero and it can be assumed that the energy transfer for these three tests does not arise. In this way the lower limit of parameter $m_{0t1.5}/m_{0t}$=0.076, that has been obtained by averaging the three corresponding values of $m_{0t1.5}/m_{0t}$ in Figure 4.52, can be interpreted as the threshold value where transfer of energy starts/ends for all the tested waves. A similar value of $m_{0t1.5}/m_{0t}$=0.071 was obtained in the study of Carevic et al. (2013), where laboratory tests were carried out in presence of a smooth submerged breakwater.

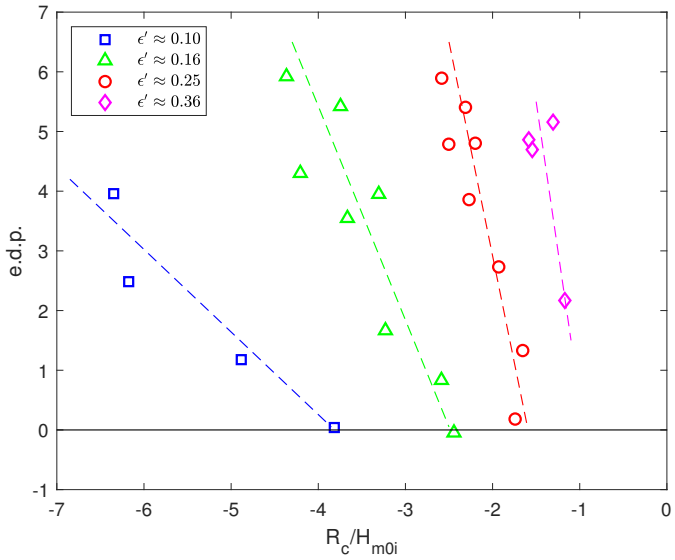

Figure 4.53: Correlation between e.d.p. and R_c/H_{m0i} for the measured data.

In Figure 4.52 the dependence on the parameter ϵ' is identified because the waves to be tested have been selected with the attempt to keep the nonlinearity parameter ϵ nearly the same over the bar crest. A linear relationship between $m_{0t1.5}/m_{0t}$ and R_c/H_{m0i} was also found in Carevic et al. (2013), depending on the deepwater wave steepness $s_{op} = 2\pi H_{m0i}/gT_p^2$. The same results of Figure 4.52 are shown in Figure 4.54 where the dots are now coloured with the values of s_{op}, as in Carevic et al. (2013). The energy shifted to higher frequencies increases by keeping constant R_c/H_{m0i} and decreasing s_{op}, as expected.

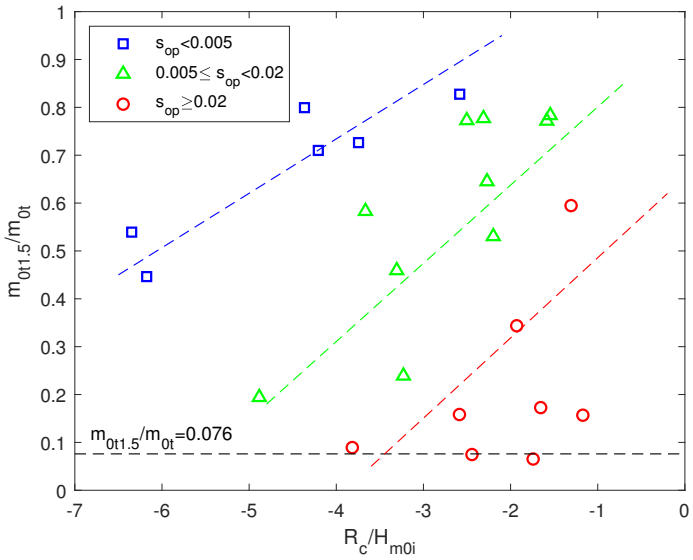

Figure 4.54: Ratio between the transmitted energy for frequencies $f > 1.5f_p$ and the total transmitted energy plotted versus the relative submergence R_c/H_{m0i} for different values of s_{op}.

From the previous analyses it is highlighted that the structure submergence and the peak period are the main parameters which influence the transfer of energy to higher frequencies. On the other hand, the incident wave height is found to have a smaller effect on the redistribution of high frequency energy. In Figure 4.55 $m_{0t1.5}/m_{0t}$ is plotted against the ratio R_c/L_p, where L_p is the wave length calculated with the peak period T_p at the water depth h. The dots are coloured for different ranges of H_{m0i}/h, in order to verify also the effect of H_{m0i}. Figure 4.55 shows that there is a clear trend of $m_{0t1.5}/m_{0t}$ with the parameter R_c/L_p: for small values of R_c/L_p (higher submergence and shorter waves) the values of $m_{0t1.5}/m_{0t}$ asymptotically tends to the lower limit $m_{0t1.5}/m_{0t}$=0.076 while it increases to values of 0.8 for higher R_c/L_p (lower submergence and longer waves). The increase of H_{m0i}/h causes a greater high-frequency energy transfer for $-0.051 \leq R_c/L_p \leq -0.024$, while it has a small influence for values of R_c/L_p outside this range. In Figure 4.56 the ratio $m_{0t1.5}/m_{0t}$ is plotted as a function of a non-dimensional parameter, defined as $(R_c/L_p)^2(h/H_{m0i})^{1/3}$, which provides the best-fit to the data (with a squared-correlation r^2=0.98). The non-dimensional parameter is also well correlated with the transmitted energy at frequencies $f > 2.5f_p$ and $f > 3.5f_p$, as can be observed in Figure 4.57. For the submerged structure tested during this experimental campaign, Figure 4.57 also shows that the energy at frequencies higher than $3.5f_p$ is far from negligible for various tested waves and it reaches the maximum value of approximately 30% for the longest and highest wave (H_s=8cm and T_p=2.5s) with the smallest submergence (R_c=-0.10m). An increase of the energy at higher frequencies in the transmitted spectrum causes a reduction of the mean period. Figure 4.58 shows that also the mean spectral period T_m can be represented as a function of the parameter $(R_c/L_p)^2(h/H_{m0i})^{1/3}$.

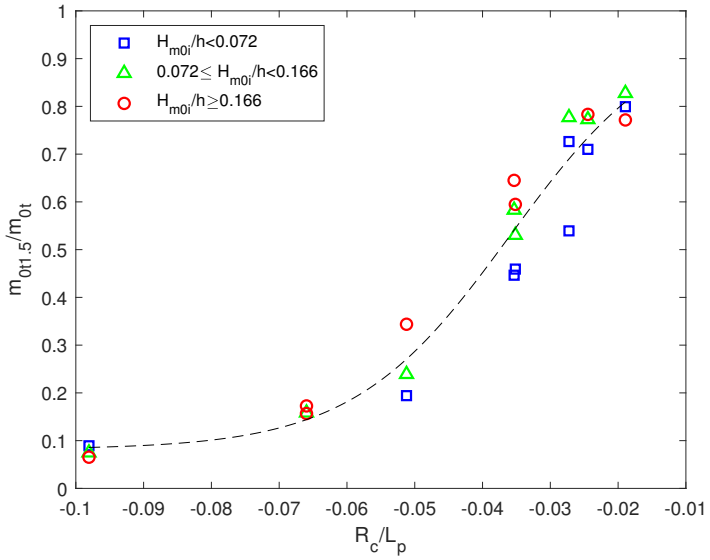

Figure 4.55: Ratio between the transmitted energy for frequencies $f > 1.5f_p$ and the total transmitted energy plotted versus R_c/H_{m0i} for different values of H_{m0i}/h.

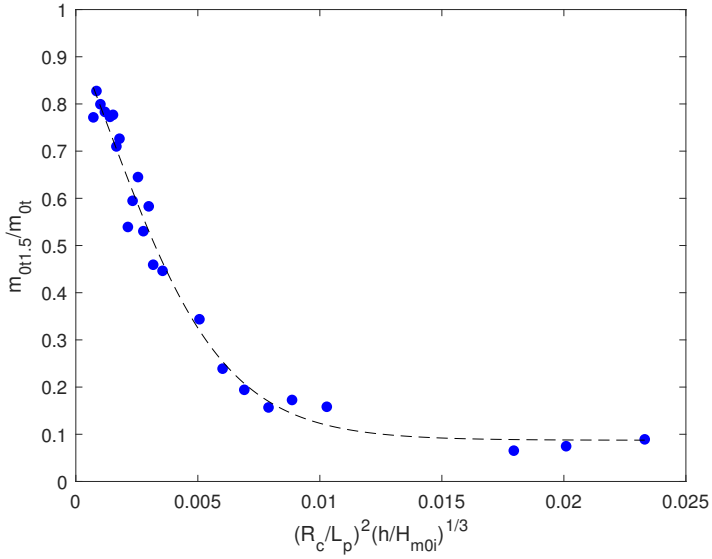

Figure 4.56: Ratio between the transmitted energy for frequencies $f > 1.5f_p$ and the total transmitted energy plotted versus $(R_c/L_p)^2(h/H_{m0i})^{1/3}$.

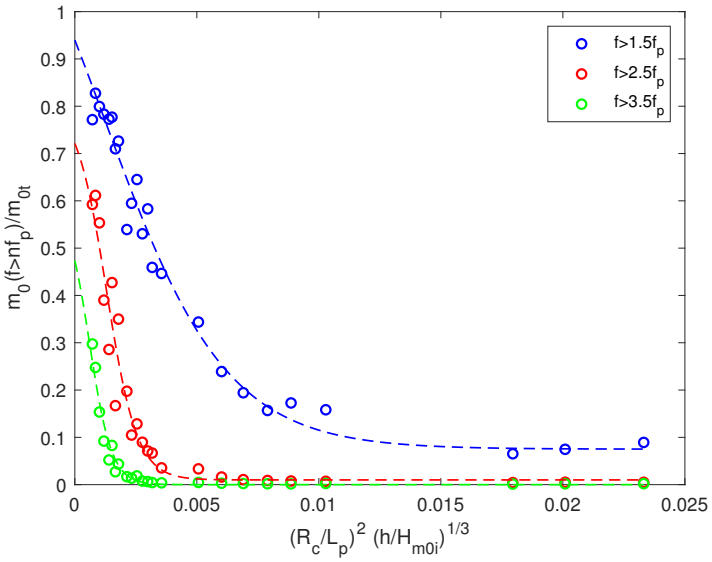

Figure 4.57: Ratio between the transmitted energy for frequencies $f > 1.5f_p$, $f > 2.5f_p$ and $f > 3.5f_p$ and the total transmitted energy plotted versus $(R_c/L_p)^2(h/H_{m0i})^{1/3}$.

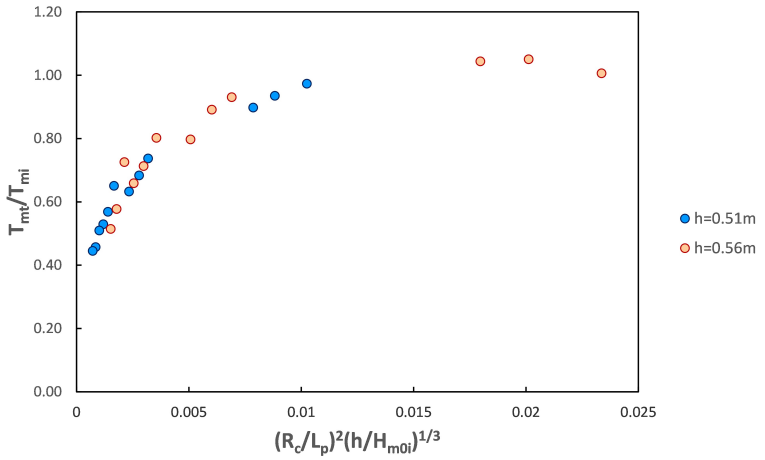

Figure 4.58: Ratio of mean period T_m transmitted/incident as function of the term $(R_c/L_p)^2(h/H_{m0i})^{1/3}$.

4.3 Wave run-up over a beach

The transformation of the wave spectrum behind submerged obstacles also affects the run-up on the beach. The second experimental campaign has been carried out to evaluate the wave run-up over a 1:20 impermeable slope in presence of the submerged bar, for both monochromatic and random waves.
For each test, the run-up is evaluated by identifying the individual maxima R_u of the water level time series recorded by the run-up wave gauge. The 2% exceedence value of run-up $R_{u2\%}$ is calculated from the cumulative probability density function of the discrete measures of R_u (Figure 4.59).

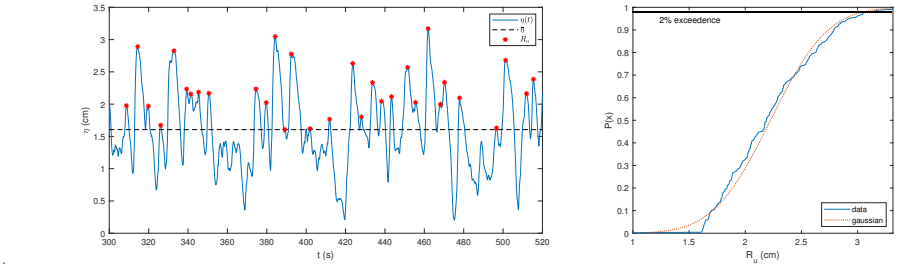

Figure 4.59: Water level time series (left panel) recorded by the run-up wave gauge indicating individual run-up maxima R_u and the setup at the beach slope $\bar{\eta}$. The cumulative PDF of the discrete measures of R_u compared with the Gaussian distribution (right panel); random wave H_s=8cm, T_p=2.5s and h=0.56m.

The value of the run-up is also computed by merging contributions from setup and swash:

$$R_{u2\%} = \bar{\eta} + \frac{S}{2} \tag{4.6}$$

The significant swash height S can be subdivided into the significant incident-band S_{inc} (f >0.05Hz) and the infragravity-band S_{ig} (f ≤0.05Hz):

$$S = \sqrt{(S_{inc})^2 + (S_{ig})^2} \tag{4.7}$$

where S_{inc} and S_{ig} are calculated from the spectra of the continuous water level time series:

$$S_{inc} = 4\sqrt{\int_{0.05}^{\infty} E_\eta(f)df} \tag{4.8}$$

$$S_{ig} = 4\sqrt{\int_{0}^{0.05} E_\eta(f)df} \tag{4.9}$$

where $E_\eta(f)$ is the variance density of the shoreline motion. The assumption that the 2% exceedence level for run-up approximately equals $\bar{\eta} + S/2$ (Equation 4.6) is first tested. The squared-correlation r^2 between the measured values of $\bar{\eta} + S/2$ and $R_{u2\%}$ is 0.99 for monochromatic waves and 0.96 for random waves. The slope of the regression is around 1.1 as found by Stockdon et al. (2006), reflecting the slight deviation from the Gaussian distribution of the natural swash. To account for this

deviation, the slope of the regression of Figures 4.60 and 4.61 is included in Equation 4.6, resulting in the following definition of run-up:

$$R_{u2\%} = 1.1\left[\bar{\eta} + \frac{S}{2}\right] \tag{4.10}$$

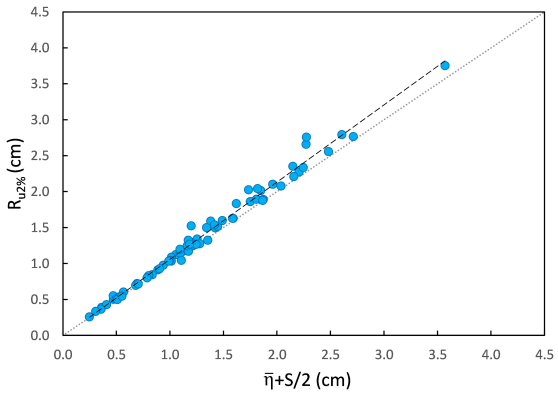

Figure 4.60: The 2% run-up elevation plotted against the sum of setup and half of the swash excursion for monochromatic waves. The dotted line is a 1:1 line, the dashed line is the best fit to the data (m=1.07, b=-0.02, r^2=0.99).

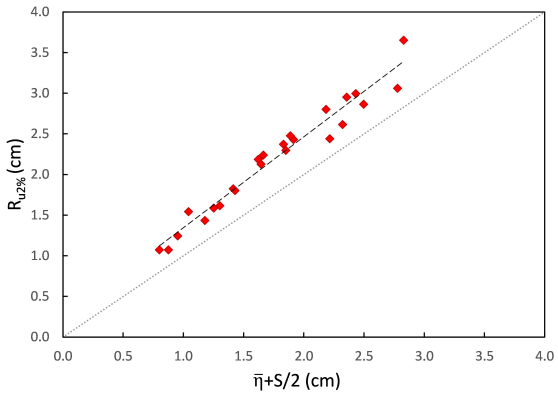

Figure 4.61: The 2% run-up elevation plotted against the sum of setup and half of the swash excursion for random waves. The dotted line is a 1:1 line, the dashed line is the best fit to the data (m=1.12, b=0.23, r^2=0.96).

The run-up value measured on the linear beach with a slope of 1:20 has been related to the incident and the transmitted wave characteristics. The empirical parametrization of run-up is presented in dimensional space and the regression is forced through the origin. The measured run-up of monochromatic waves is best parametrized as a function of the incident wave height H_i from the method of Lin and Huang (2004), the wavelength L at the wave paddle and the beach slope β_f (Figure 4.62):

$$R_{u2\%} = 0.66\beta_f(H_i L)^{0.5} \tag{4.11}$$

The squared-correlation of the dimensional parametrization is r^2=0.83 and the rms error is equal to 0.30cm. Table 4.8 presents a summary of the regression coefficients for the suggested parametrizations. In Table 4.8 also the parametrizations with the transmitted wave (H_{m0t} and $L{-}20t$ computed with $T{-}20t$) are reported.
For monochromatic waves it has been observed that about 82% of the run-up is due to the contribution of the setup. This could explain the fact that the wave run-up of monochromatic waves depends on the incident wave height. In fact, the setup is generated by wave breaking and it increases for higher incident waves. The propagation over the bar of monochromatic regular waves leads to the generation of higher frequencies. For the tested waves, the Iribarren number ξ_o is lower than 1.25 ($\xi_o = 0.18 \div 1.19$) and, according to the classification of Stockdon et al. (2006), the 1:20 beach represents dissipative ($\xi_o < 0.3$) to intermediate conditions ($0.3 < \xi_o < 1.25$). Under these conditions, the higher frequency components tend to be dissipated over the beach slope and the primary component remains the main forcing of the run-up. As a consequence, the run-up results related to the wave length L of the first harmonic. This effect could be not verified for reflective beaches ($\xi_o > 1.25$) and it could be the subject of future investigation.

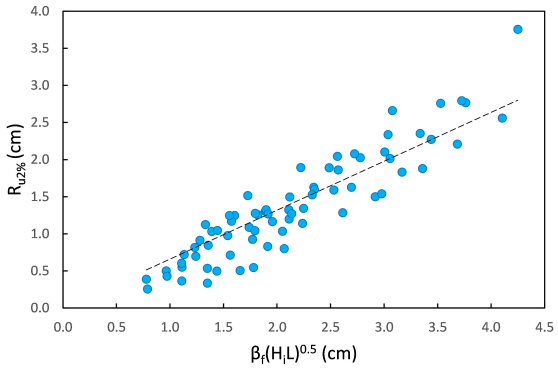

Figure 4.62: Run-up values for regular monochromatic waves as a function of the incident wave characteristics.

For the random waves the better correlations of the run-up values are obtained with the spectral characteristics of the transmitted waves measured at station 15. It has been observed that most of the incident spectra become bi-modal spectra behind the submerged bar and the nonlinear interactions also generate long waves which affect the infragravity component of swash. Using the peak period for the evaluation of the beach run-up generates fairly large scatter, due to the fact that bi-modal spectra are present. In van Gent (1999) the performance of different spectral wave periods for the evaluation of the run-up was analysed numerically and it was concluded that the wave period T_{-10} is the optimal period for describing wave run-up and wave overtopping for non uni-modal spectra. This conclusion was confirmed also in van Gent (2001) where physical model tests were performed to study wave run-up on dikes with shallow foreshores. In this work the wave run-up is related with both T_{-10} and T_{-20} at station 15 because periods with negative moments give more weight to the energy at the lower frequencies. In Figure 4.63 the run-up is best parametrized as:

$$R_{u2\%} = 1.43\beta_f(H_{m0t}L_{-10t})^{0.5} \tag{4.12}$$

where H_{m0t} is the spectral height and L_{-10t} the wavelength computed from T_{-10t}. The correlation 4.12 has a r^2=0.63 and a rms error equal to 0.42cm. Figure 4.64 relates the run-up of the random waves with H_{m0t} and the wavelength L_{-20t} derived from T_{-20t}, with the following best fit:

$$R_{u2\%} = 0.92\beta_f(H_{m0t}L_{-20t})^{0.5} \tag{4.13}$$

In this case the correlation improves to r^2=0.79 and the rms error decreases to 0.31cm. The same parametrizations are applied also to the single components of run-up, $\bar{\eta}$, S_{inc} and S_{ig} and the summary of the regression coefficients, squared correlations and rms errors is presented in Table 4.8.

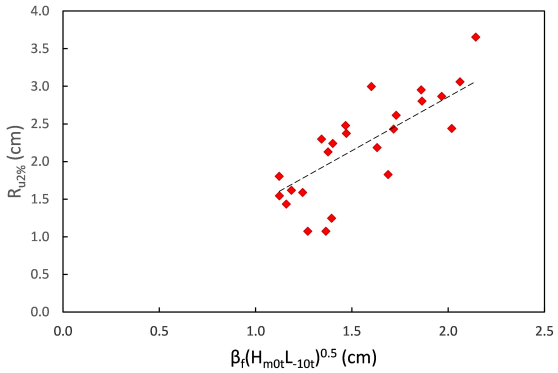

Figure 4.63: Run-up values for random waves as a function of the beach slope and the characteristics of the transmitted wave, H_{m0t} and L_{-10t}.

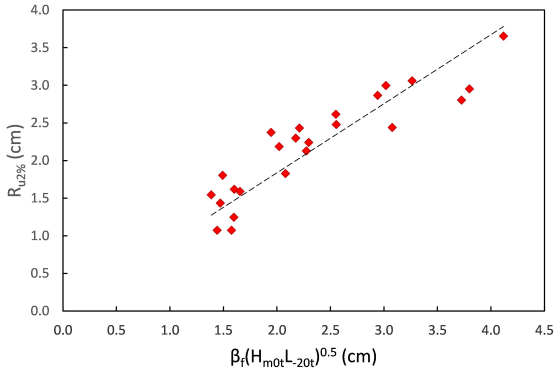

Figure 4.64: Run-up values for random waves as a function of the beach slope and the characteristics of the transmitted wave, H_{m0t} and L_{-20t}.

Table 4.8: Regression parameters for components of run-up model.

	Quantity modelled	Model input	Slope, m	Intercept, b	r^2	$rmse$ (cm)
Monochromatic	$R_{u2\%}$	$\beta_f(H_iL)^{0.5}$	0.66	0	0.83	0.30
	$\bar{\eta}$	$\beta_f(H_iL)^{0.5}$	0.54	0	0.80	0.26
	S_{inc}	$\beta_f(H_iL)^{0.5}$	0.14	0	0.11	0.24
	S_{ig}	$\beta_f(H_iL)^{0.5}$	0.07	0	0.48	0.09
	$R_{u2\%}$	$\beta_f(H_{m0t}L_{-20t})^{0.5}$	0.76	0	0.66	0.41
	$\bar{\eta}$	$\beta_f(H_{m0t}L_{-20t})^{0.5}$	0.62	0	0.66	0.35
	S_{inc}	$\beta_f(H_{m0t}L_{-20t})^{0.5}$	0.16	0	0.00	0.25
	S_{ig}	$\beta_f(H_{m0t}L_{-20t})^{0.5}$	0.08	0	0.41	0.09
Random	$R_{u2\%}$	$\beta_f(H_{m0t}L_{-10t})^{0.5}$	1.43	0	0.63	0.42
	$\bar{\eta}$	$\beta_f(H_{m0t}L_{-10t})^{0.5}$	0.60	0	0.70	0.18
	S_{inc}	$\beta_f(H_{m0t}L_{-10t})^{0.5}$	0.94	0	0.41	0.37
	S_{ig}	$\beta_f(H_{m0t}L_{-10t})^{0.5}$	0.55	0	0.62	0.23
	$R_{u2\%}$	$\beta_f(H_{m0t}L_{-20t})^{0.5}$	0.92	0	0.79	0.31
	$\bar{\eta}$	$\beta_f(H_{m0t}L_{-20t})^{0.5}$	0.39	0	0.76	0.16
	S_{inc}	$\beta_f(H_{m0t}L_{-20t})^{0.5}$	0.61	0	0.64	0.29
	S_{ig}	$\beta_f(H_{m0t}L_{-20t})^{0.5}$	0.35	0	0.72	0.20

Chapter 5

Numerical Analysis with XBeach

To better understand the hydrodynamic circulation induced by submerged breakwaters, numerical analyses have been carried out by means of XBeach, which is an open-source numerical model developed to simulate hydrodynamic and morphodynamic processes and impacts on sandy coasts. It includes the hydrodynamic processes of short and long wave transformation, wave set-up and unsteady currents and the morphodynamics due to bed load and suspended sediment transport. The numerical simulations have been performed through the non-hydrostatic model of XBeach, which solves the phase of short waves and allows to model all processes of wave propagation and decay, including run-up, overwashing and diffraction.
In this thesis the XBeach model is used to reproduce the physical model in order to test the capabilities of the numerical tool to simulate the non-linear phenomena which occurs during the propagation of waves over a submerged bar. So, the experimental results of the physical model are compared to the results obtained with the non-hydrostatic model of XBeach.
The advantage of the numerical model is that it allows to simulate a lot of different configurations for coastal structures.

5.1 Model overview

XBeach is an open-source process-based numerical model which simulates hydrodynamic and morphodynamic processes and impacts on sandy coasts (Roelvink et al., 2009, 2010). Hydrodynamic processes such as incident wave transformation (refraction, shoaling and breaking) infragravity wave transformation (generation, propagation and dissipation) and wave-induced setup are included. The included morphodynamic processes are not relevant for this research. The model can be used in 1D and 2D and is depth-averaged (1DH and 2DH).

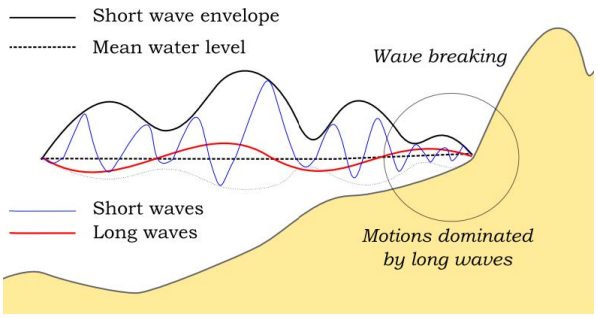

Figure 5.1: Principle sketch of the relevant wave processes in XBeach (Roelvink et al., 2010).

XBeach non-hydrostatic solves the individual incident waves and is a phase-resolving model (Roelvink et al., 2010). Both incident and infragravity waves are solved with the non-linear shallow water equations including non-hydrostatic pressure. The hydrostatic front approximation is used to improve the location of wave breaking, where the pressure under breaking bores is assumed to be hydrostatic (Smit et al., 2013).

5.2 Numerical model setup

The experimental setup has been reproduced in XBeach through a 2DH model with a domain length of 40m in the flow direction (x-direction) and a transversal width of 1m in the y-direction. A constant grid size of 5.0cm is used in x and y directions for all the length of the wave flume.
The offshore end of the numerical wave flume, where the wave generation boundary condition is applied, corresponds to the position of the first wave gauge. The structure toe is located at a distance of 7m from the offshore end of the model. Behind the structure, the impermeable beach with slope 1:20 is also modelled starting at distance of 19.50m from the seaward boundary. Figure 5.2 shows a sketch of the numerical model domain.

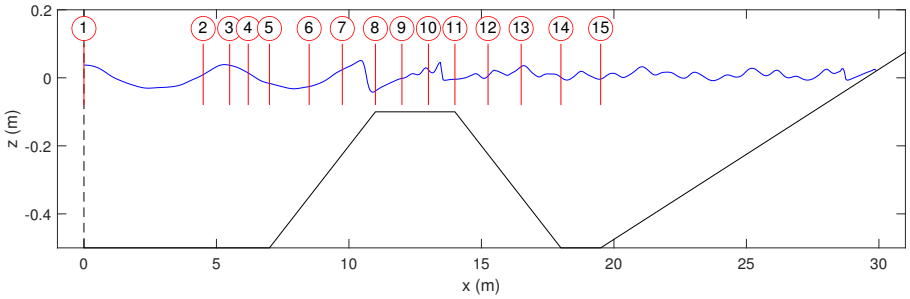

Figure 5.2: Sketch of the numerical domain in XBeach: positions of the wave gauges and water surfaces computed for the test "H8T25h51".

The offshore flow boundary condition is set as *nonh_1d* to use the non-hydrostatic solver of XBeach, lateral boundaries are set as *wall* and the landward boundary is set as *abs_2d* that is an absorbing boundary condition.

The time step of the numerical simulations is adapted by the model in order to keep a maximum value of the Courant-Friedrichs-Lewy number CFL equal to 0.7.
Among all the experimental wave tests, twelve regular waves have been reproduced by the numerical model for both the tested water depths. For each period three different wave heights have been selected as representative of different hydrodynamic conditions, non-breaking, spilling and plunging waves. All the random tested cases with h=0.51m and h=0.56m have been reproduced with XBeach. The input wave height of each simulation derives from the experimental measurements recorded by the first wave gauge at station 1. The wave characteristics are summarized on Tables 5.1 and 5.2. For monochromatic waves a *stat* type wave generation condition is applied which requires a H_{rms} wave height and a representative wave period T_{rep}. In such cases the numerical simulations last 300s.
Random wave simulations have a *jons* type wave generation condition to provide a JONSWAP spectrum input. This condition requires an additional file where the main parameters of the wave spectrum can be defined (H_{m0}, T_p, γ). The directional spreading coefficient is set to 1000 in order to generate an unidirectional spectrum. For random waves, the duration of the numerical simulations depends on the peak period and it is set equal to 600s for T_p=1.0s, 900s for T_p=1.5s, 1200s for T_p=2.0s and 1500s for T_p=2.5s.

Table 5.1: Characteristics of monochromatic waves used in the numerical simulations.

Name	h (m)	H_{rms} (cm)	T_{rep} (s)
H5T10h51	0.51	4.0	1.0
H8T10h51	0.51	6.5	1.0
H12T10h51	0.51	9.6	1.0
H4T15h51	0.51	3.6	1.5
H6T15h51	0.51	5.5	1.5
H10T15h51	0.51	9.1	1.5
H3T20h51	0.51	2.5	2.0
H5T20h51	0.51	4.1	2.0
H8T20h51	0.51	6.7	2.0
H3T25h51	0.51	2.5	2.5
H5T25h51	0.51	4.2	2.5
H8T25h51	0.51	6.8	2.5
H5T10h56	0.56	4.1	1.0
H8T10h56	0.56	6.4	1.0
H12T10h56	0.56	9.6	1.0
H4T15h56	0.56	3.5	1.5
H6T15h56	0.56	5.3	1.5
H10T15h56	0.56	8.8	1.5
H3T20h56	0.56	3.0	2.0
H5T20h56	0.56	4.8	2.0
H8T20h56	0.56	7.5	2.0
H3T25h56	0.56	2.6	2.5
H5T25h56	0.56	4.4	2.5
H8T25h56	0.56	7.1	2.5

Table 5.2: Characteristics of random waves used in the numerical simulations.

Name	h (m)	H_{m0} (cm)	T_p (s)
SpH5T10h51	0.51	3.9	1.0
SpH8T10h51	0.51	6.0	1.0
SpH12T10h51	0.51	8.5	1.0
SpH4T15h51	0.51	3.0	1.5
SpH6T15h51	0.51	4.5	1.5
SpH10T15h51	0.51	7.6	1.5
SpH3T20h51	0.51	2.4	2.0
SpH5T20h51	0.51	4.0	2.0
SpH8T20h51	0.51	6.4	2.0
SpH3T25h51	0.51	2.3	2.5
SpH5T25h51	0.51	3.9	2.5
SpH8T25h51	0.51	6.3	2.5
SpH5T10h56	0.56	3.9	1.0
SpH8T10h56	0.56	6.1	1.0
SpH12T10h56	0.56	8.6	1.0
SpH4T15h56	0.56	3.1	1.5
SpH6T15h56	0.56	4.6	1.5
SpH10T15h56	0.56	7.8	1.5
SpH3T20h56	0.56	2.4	2.0
SpH5T20h56	0.56	4.1	2.0
SpH8T20h56	0.56	6.6	2.0
SpH3T25h56	0.56	2.4	2.5
SpH5T25h56	0.56	4.0	2.5
SpH8T25h56	0.56	6.5	2.5

Output of water levels are generated in 15 different positions along the domain, at the locations of the wave gauges in the physical model. The positions of the output points and the instantaneous free surface calculated for the test "H8T25h51" are shown in Figure 5.2. The interval time of the output is set according to the sample frequency of the wave gauges (35Hz). The run-up over the impermeable slope is also computed with the addition of an output run-up gauge location. The XBeach non-hydrostatic model has been calibrated with sea bottom friction and run-up gauge depth, the minimum depth which is used to determine the last wet point in the run-up gauge (Roelvink et al., 2010). The calibration aims to get the better agreement of both the wave height transformation over the bar and the run-up level over the beach with the experimental data. Stockdon et al. (2014) showed that the XBeach surfbeat model is sensitive to the choice of the run-up gauge depth. The water depth threshold for the definition of the waterline in the model simulations is set to 0.001m to correspond with the probable water depth identified as the leading run-up edge by the run-up wave gauge. In the XBeach model different bottom friction formulations are available, some of which are depth independent and some are depth dependent. In the study of de Beer (2017) the XBeach *non-h* was used to simulate wave run-up observed during the SandyDuck '97 experiment on an intermediate-reflective sandy beach. Three different bottom friction formulations were tested for the calibration of the model of de Beer (2017). The formulation of Chezy was chosen because the depth dependent formulations of Manning and White-Colebrook resulted in a lower prediction of the significant swash.
Also in the present thesis, the formulation of Chezy has been chosen. It has been found that the wave transformation over the obstacle is little affected by the bed friction parameter, while the wave run-up is strongly influenced by this calibration coefficient. The calibration led to the selection of a Chezy coefficient of C=$20m^{1/2}/s$. This value is low to be representative of a smooth surface but the Chezy formulation

is depth independent and it leads to a smaller friction in the shallow water of the oscillating zone at the scale of the physical model.

5.3 Comparison with experimental data

The numerical results of XBeach non-hydrostatic model are compared to the experimental measurements. For monochromatic waves the time series of the free surface recorded at different stations are compared to those calculated by the numerical model. The comparisons for random waves are carried out in terms of the spectral evolution along the wave flume. Additional comparisons are carried on in terms of the wave run-up over the beach slope.

5.3.1 Monochromatic waves

Time domain comparisons of the measured and computed surface displacements for monochromatic waves of Table 5.1 are shown from Figure 5.3 to Figure 5.7 at six different stations. Station 5 is located at the structure toe, at a distance of 7m from the wave generation boundary condition. Stations 8 and 10 correspond to the wave gauges at the end of the upslope and over the bar crest, respectively. The other three stations show the results over the downslope and behind the bar, at stations 12, 14 and 15. The numerical model reproduces the observed evolution and decomposition of the wave field quite well. The initial nonlinear steepening on the seaward slope (stations 5 and 8) is well represented for each wave condition even if the numerical model under-predicts the wave heights for the cases with T=1.0s. Also the subsequent enhancement of higher harmonics over the bar crest (station 10) and the associated profile distortion are well calculated apart from the breaking waves with T=2.5s in which the wave crests are overestimated. This effect could be improved with the calibration of the breaking parameters. For these numerical simulations the default values are used. The representation of the wave field shows more discrepancies between measured and computed values in the de-shoaling region at station 12 and 14. This is particularly evident in the case of breaking waves with the higher period (Figures 5.6 and 5.8), in which a phase shift is present and the amplitudes of the higher order harmonics are not well reproduced. For the shortest breaking waves this effect is less pronounced due to the smaller energy transfer to super-harmonics (Figures 5.5 and 5.7). This effect is also evident behind the bar at station 15 and it is enhanced for the highest tested waves, probably due to the influence of wave breaking. Figure 5.9 shows the XBeach run-up predictions compared to the measured values for the six tested waves. In most cases the model overestimates the values of the wave run-up over the beach slope.

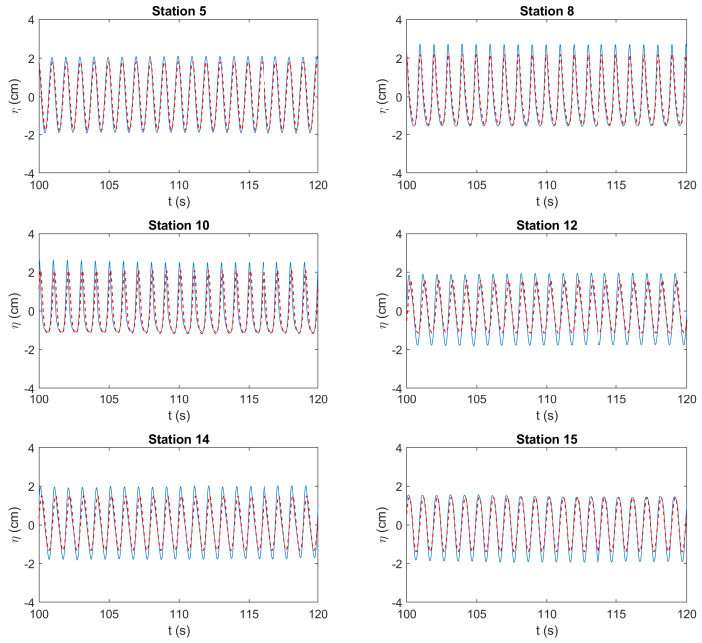

Figure 5.3: Surface elevation at several stations for monochromatic incident waves with H=5cm, T=1s and h=0.51m. (−) Experimental values; (−−) values obtained numerically with the XBeach *non-h* model.

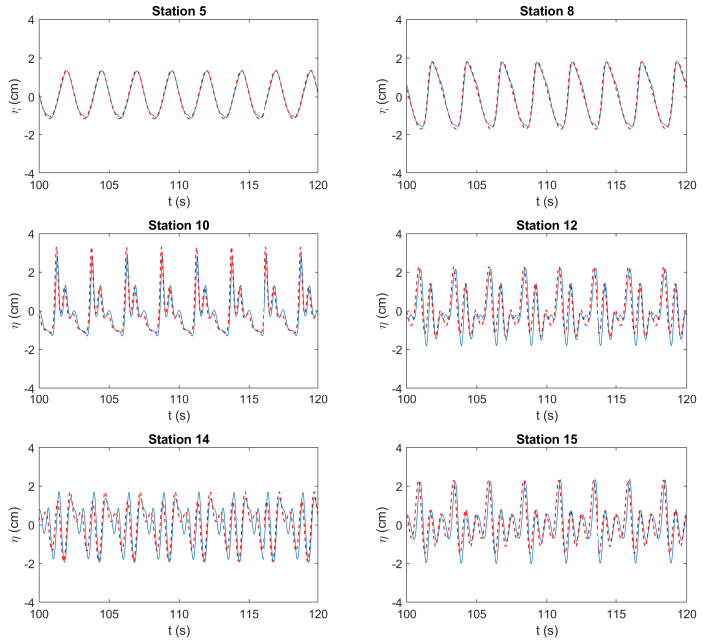

Figure 5.4: Surface elevation at several stations for monochromatic incident waves with H=3cm, T=2.5s and h=0.51m. (−) Experimental values; (−−) values obtained numerically with the XBeach *non-h* model.

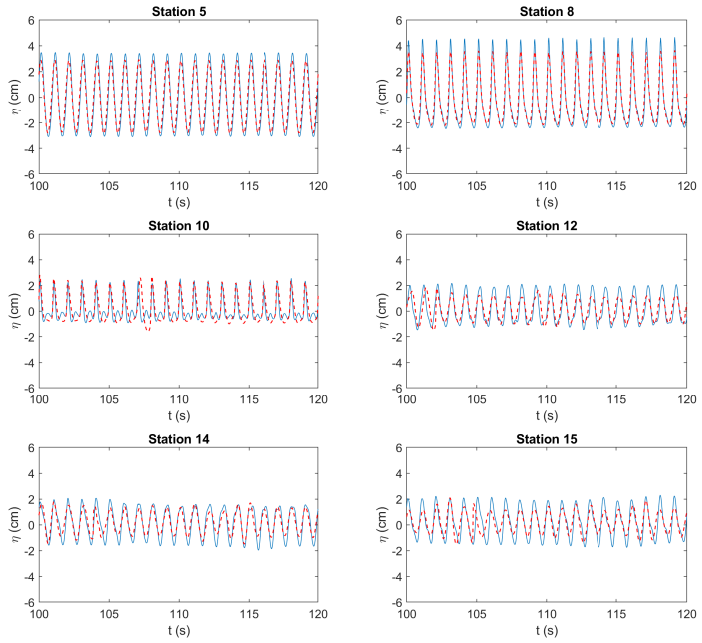

Figure 5.5: Surface elevation at several stations for monochromatic incident waves with H=8cm, T=1s and h=0.51m. (−) Experimental values; (−−) values obtained numerically with the XBeach *non-h* model.

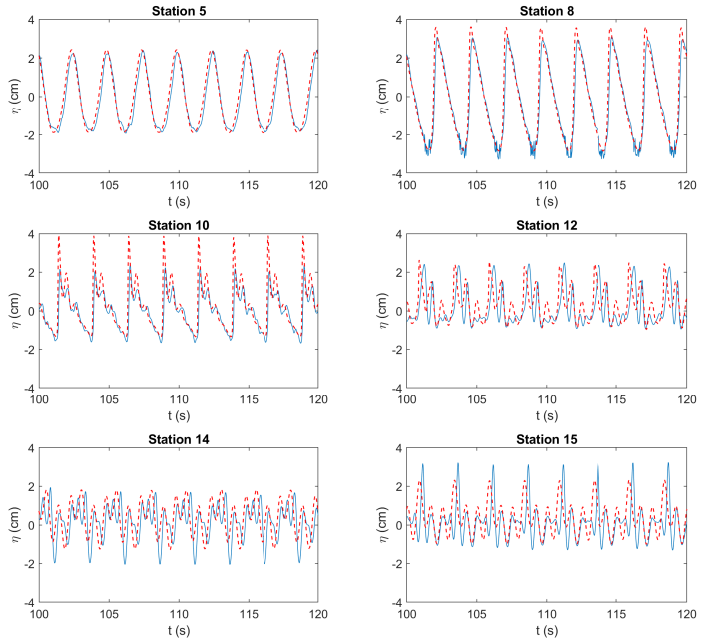

Figure 5.6: Surface elevation at several stations for monochromatic incident waves with H=5cm, T=2.5s and h=0.51m. (−) Experimental values; (−−) values obtained numerically with the XBeach *non-h* model.

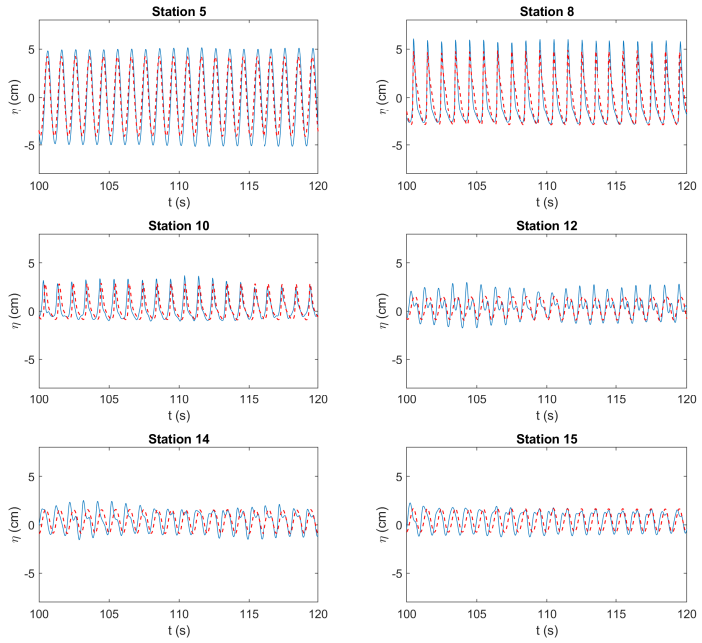

Figure 5.7: Surface elevation at several stations for monochromatic incident waves with H=12cm, T=1s and h=0.51m. (−) Experimental values; (−−) values obtained numerically with the XBeach *non-h* model.

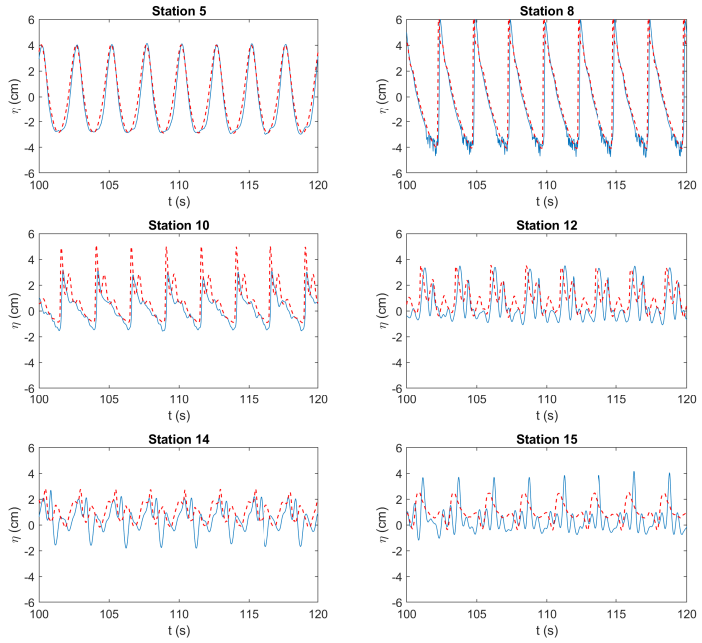

Figure 5.8: Surface elevation at several stations for monochromatic incident waves with H=8cm, T=2.5s and h=0.51m. (−) Experimental values; (−−) values obtained numerically with the XBeach *non-h* model.

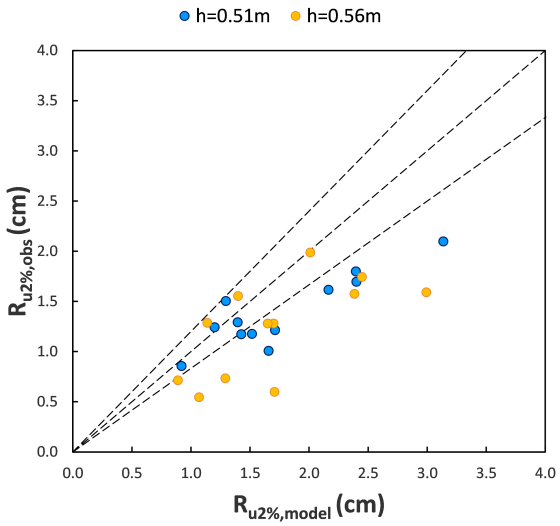

Figure 5.9: Observed and modelled $R_{u2\%}$ for the XBeach *non-h* model. Dashed lines indicate the 1:1 and 20% error lines.

5.3.2 Random waves

Frequency domain comparisons of the measured and computed energy spectra for the random waves of Table 5.2 with peak periods T_p=1s and T_p=2.5s are shown from Figure 5.10 to Figure 5.15. The results are shown at the same six stations selected for monochromatic waves. The spectral evolution over and behind the obstacle is well reproduced by the model. More discrepancies are observed for the shortest random waves which show similar behaviours for the three different wave heights (Figures 5.10, 5.12, 5.14). For such waves, the spectral energy density at the peak frequency is underestimated along the upslope up to station 7 (not shown). From the horizontal crest (station 8) the spectral peak is well estimated. However, the spectral energy at higher frequencies is underestimated for any case. Better comparisons are obtained for the longest waves (Figures 5.11, 5.13, 5.15). The numerical model is able to reproduce the spectral evolution along the wave flume, both in terms of the spectral peak and of the energy redistribution at higher frequencies. The differences in the energy spectra increase when the wave height and, thus, the wave nonlinearity increase. However, the larger deviations are observed for frequencies higher than about 1.2Hz, corresponding to $3f_p$.
In addition, the numerical model well reproduces the generation of long waves due to the breaking mechanism and to the difference interactions between harmonic components close to the peak frequency. As seen in section 4.3, the correct representation of infragravity waves is particularly important for the reliability of the numerical model in correctly estimating the wave run-up over beaches protected by submerged structures.

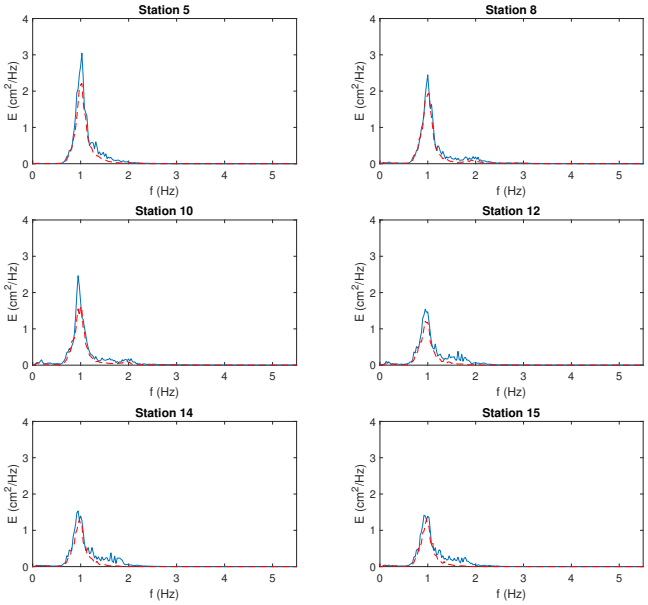

Figure 5.10: Energy spectra at several stations for random incident wave with H_s=5cm, T_p=1.0s and h=0.51m. (−) Experimental values; (−−) values obtained numerically with the XBeach *non-h* model.

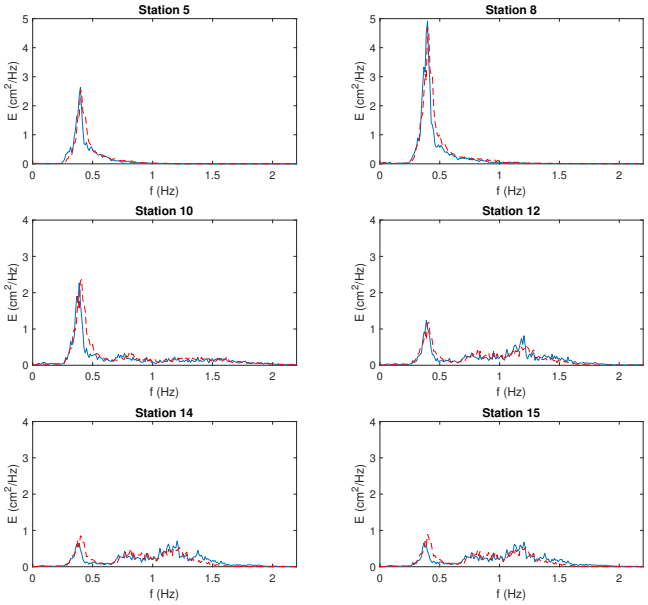

Figure 5.11: Energy spectra at several stations for random incident wave with H_s=3cm, T_p=2.5s and h=0.51m. (−) Experimental values; (−−) values obtained numerically with the XBeach *non-h* model.

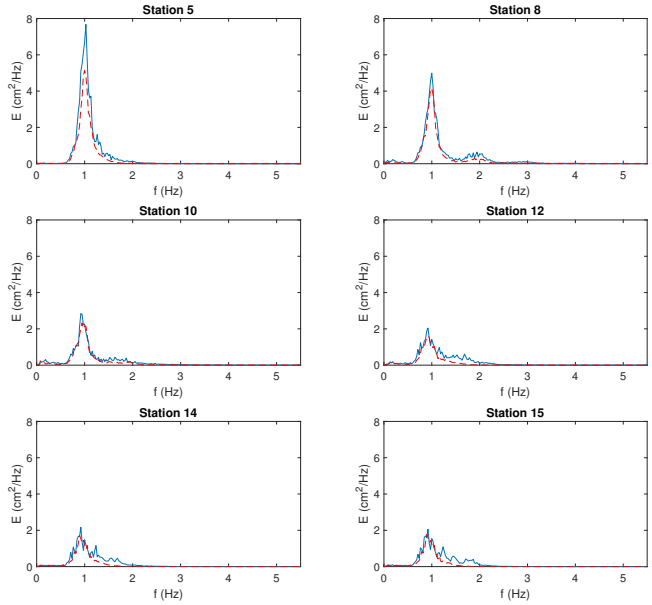

Figure 5.12: Energy spectra at several stations for random incident wave with H_s=8cm, T_p=1.0s and h=0.51m. (−) Experimental values; (−−) values obtained numerically with the XBeach *non-h* model.

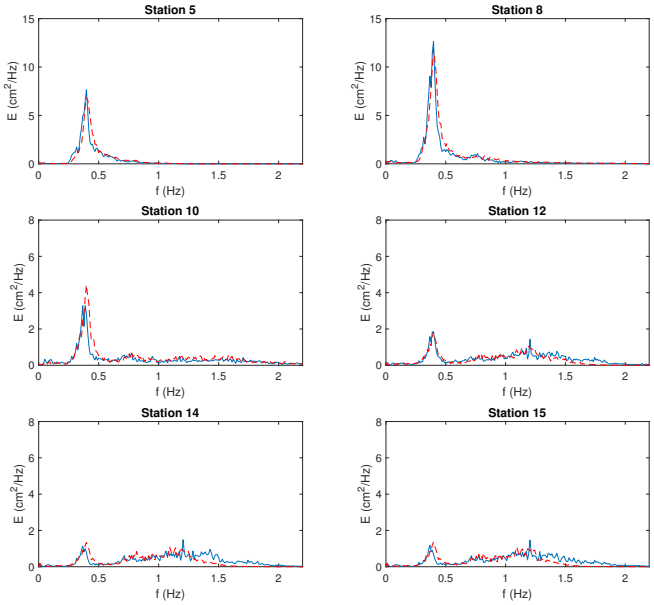

Figure 5.13: Energy spectra at several stations for random incident wave with H_s=5cm, T_p=2.5s and h=0.51m. (−) Experimental values; (−−) values obtained numerically with the XBeach *non-h* model.

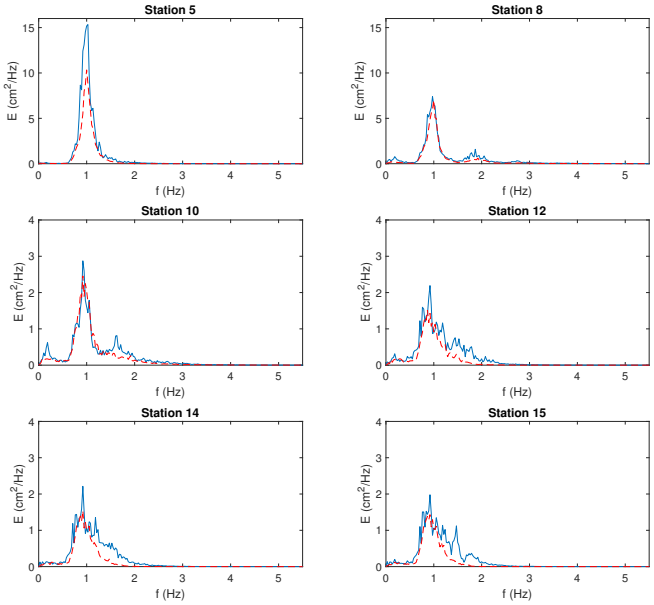

Figure 5.14: Energy spectra at several stations for random incident wave with H_s=12cm, T_p=1.0s and h=0.51m. (−) Experimental values; (−−) values obtained numerically with the XBeach *non-h* model.

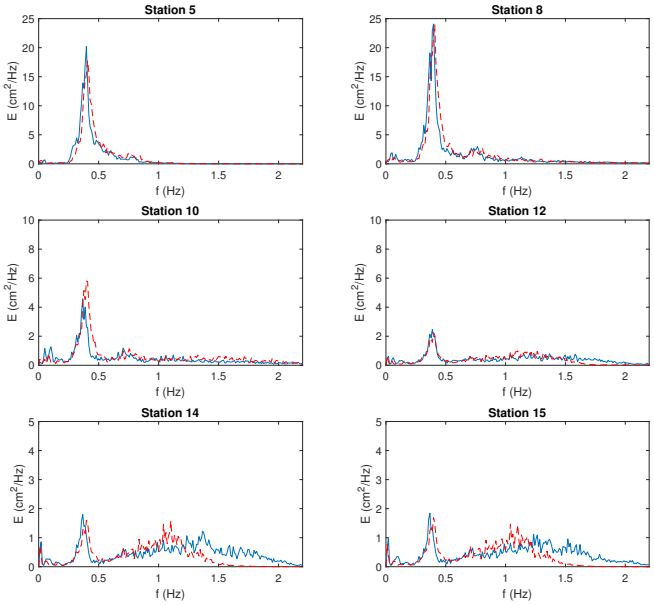

Figure 5.15: Energy spectra at several stations for random incident wave with H_s=8cm, T_p=2.5s and h=0.51m. (−) Experimental values; (−−) values obtained numerically with the XBeach *non-h* model.

For random waves in addition to the 2%-exceedence run-up level ($R_{u2\%}$), the setup ($\bar{\eta}$), the incident-band and the infragravity-band swash (S_{inc} and S_{ig}) are computed following Equations 4.8 and 4.9. From Figure 5.16 to Figure 5.21 the predicted swash spectra obtained with XBeach are compared with the measured swash spectra. The results show that the XBeach *non-h* model describes the shape of the swash spectrum quite well for both the shortest and the longest tested waves. The comparisons for all the tested waves are summarized in Figure 5.22 and Table 5.3 for the 2%-exceedence run-up level and for the single contributions of run-up.
The error statistics used to define the performance of the model for predicting run-up are the root mean squared error ($rmse$), $bias$ and the coefficient of determination (r^2). With Y representing the model results and X representing the measured values, the $bias$ is defined as:

$$bias = \frac{1}{n}\sum_{i=1}^{n}(Y_i - X_i) \tag{5.1}$$

The performance of XBeach *non-h* is better for setup and infragravity-band swash predictions, while the model overestimates the incident-band swash ($bias$=0.42cm), particularly for the case with the increased water level h=0.56m.

Table 5.3: Statistics describing the fit between observations and model results for run-up.

	$rmse$ (cm)	$bias$ (cm)	r^2
$\bar{\eta}$	0.17	0.03	0.74
S_{inc}	0.33	0.42	0.59
S_{ig}	0.17	-0.02	0.75
$R_{u2\%}$	0.42	0.18	0.64

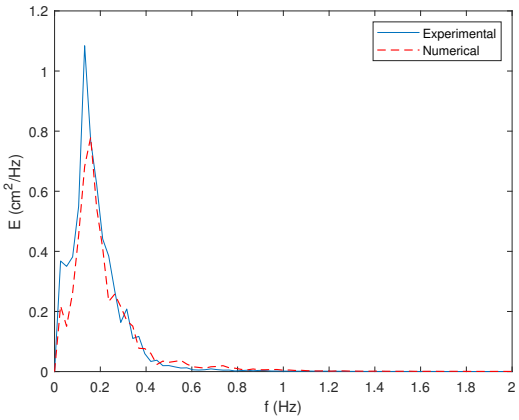

Figure 5.16: Swash spectra for random incident wave with H_s=5cm, T_p=1.0s and h=0.51m. (−) Experimental values; (−−) values obtained numerically with the XBeach *non-h* model.

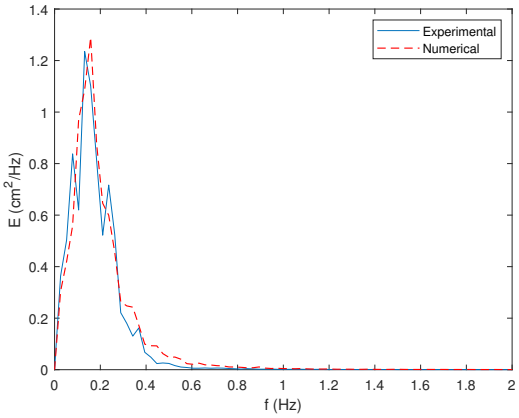

Figure 5.17: Swash spectra for random incident wave with H_s=8cm, T_p=1.0s and h=0.51m. (−) Experimental values; (−−) values obtained numerically with the XBeach *non-h* model.

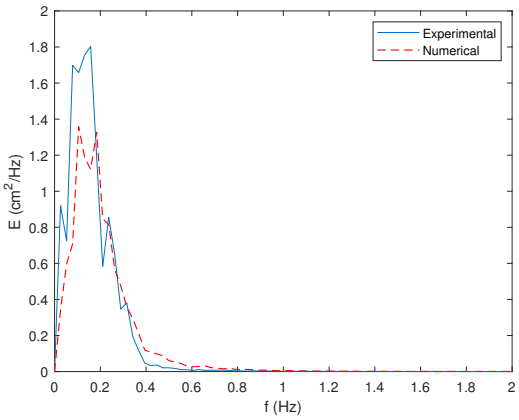

Figure 5.18: Swash spectra for random incident wave with H_s=12cm, T_p=1.0s and h=0.51m. (−) Experimental values; (−−) values obtained numerically with the XBeach *non-h* model.

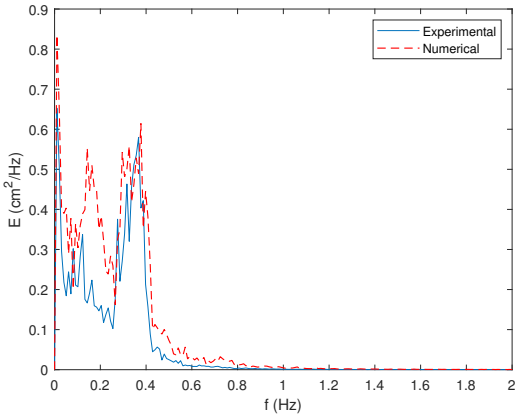

Figure 5.19: Swash spectra for random incident wave with H_s=3cm, T_p=2.5s and h=0.51m. (−) Experimental values; (−−) values obtained numerically with the XBeach *non-h* model.

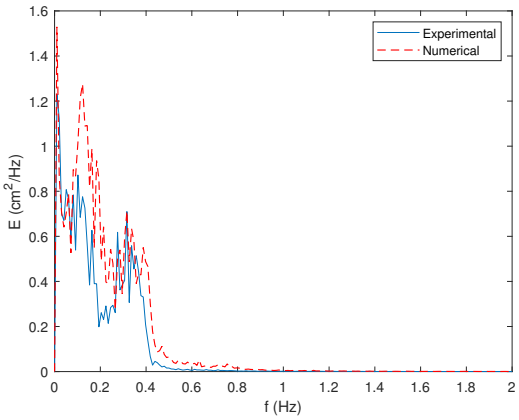

Figure 5.20: Swash spectra for random incident wave with H_s=5cm, T_p=2.5s and h=0.51m. (−) Experimental values; (−−) values obtained numerically with the XBeach *non-h* model.

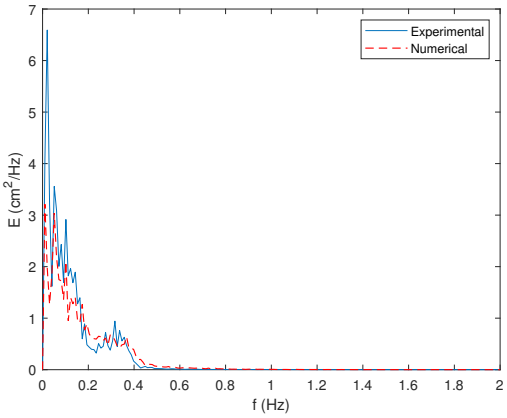

Figure 5.21: Swash spectra for random incident wave with H_s=8cm, T_p=2.5s and h=0.51m. (−) Experimental values; (−−) values obtained numerically with the XBeach *non-h* model.

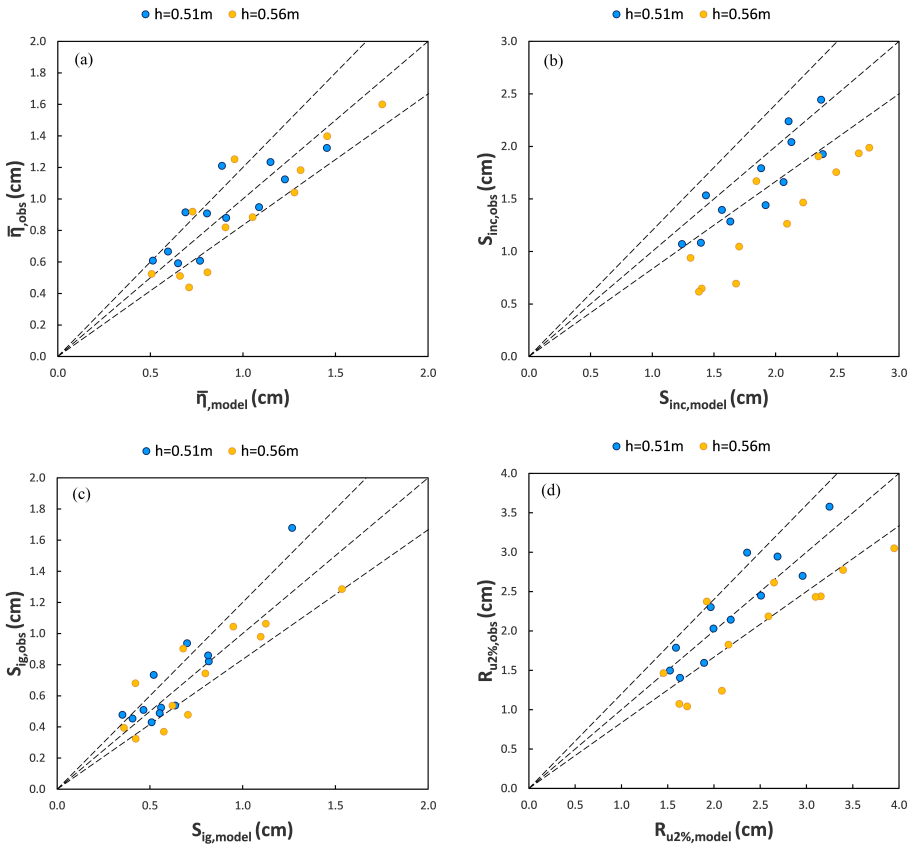

Figure 5.22: Observed and modelled $\bar{\eta}$ (a), S_{inc} (b), S_{ig} (c) and $R_{u2\%}$ (d) for the XBeach *non-h* model. Dashed lines indicate the 1:1 and 20% error lines.

Chapter 6

Conclusions

The objective of this thesis is to increase the knowledge of non-linear interaction mechanisms induced by the passage of waves over submerged structures. Extensive laboratory experiments have been carried out to study the transformations of both monochromatic and random waves during the propagation over a submerged obstacle. A better physical understanding of these processes can be incorporated in numerical models to improve their predictive capabilities. In order to better understand the energy exchange between the different wave harmonics, the submerged obstacle has been made as a bar with a larger berm width and gentler slopes with respect to the typical geometries used for submerged breakwaters, in order to analyse the non-linear interactions over a longer distance. At first, the monochromatic waves have been studied because they are easier to analyse and they provide quite valuable information about the generation of super-harmonics. Monochromatic waves are useful to simulate narrow-banded spectra, which are typical of sea swell conditions. By analysing the evolution of the harmonic amplitude over the structure it is found that the the generation of higher order components is affected by the wave period: during the propagation of the shorter wave, the first component remains the dominant one, while the increase of the wave length provide a larger transferred energy to the third and to the fourth harmonics. The free surface measurements have been also studied by means of spectral and bispectral analyses and the influence of different wave parameters on the non-linear wave interactions has been evaluated. It has been observed that the increase in the wave period causes a greater transfer of energy at high frequencies and, in some cases, the secondary harmonic components become prevalent. The wave breaking acts by mainly reducing the energy of the primary component and it involves a redistribution of energy over a wider high-frequency range, with less pronounced peaks at the secondary harmonics. For breaking waves, more energy is also shifted towards low frequencies and it could be due to the breakpoint mechanism of generation of infragravity waves. The bispectral analysis is used to examine the spatial variation in intensity of nonlinear coupling in a wave field propagating over and beyond the bar. The observed spatial variations of the nonlinearity parameters (such as bicoherence, skewness and asymmetry) indicate strong phase couplings between the primary component and its harmonics over the bar due to the non-linear triad interactions. The occurrence of energy transfer is confirmed by the bispectral analysis. Indeed, when the wave propagates in shallow water conditions over the horizontal crest, the triplet resonance conditions are nearly satisfied and significant energy transfers take place to higher harmonics. After the generation of higher harmonics,

such harmonics propagate over the bar in intermediate water depth conditions and, consequently, for those frequencies the transfer of energy is back and forth because of the greater mismatch in the phase speed.

The evolution of the biphase has been found to be consistent with visual observation that waves evolve from a slightly peaked, nearly sinusoidal shape offshore of the structure (with biphase equal to zero) to a shape characterized by a steep front face over the horizontal crest of the structure (with biphase equal to $-\pi/2$). Over the downslope of the bar the biphase value of the main harmonic interaction with itself evolves to positive values. The biphases of the other harmonic interactions tend to be randomly scattered beyond the bar, hence, higher harmonics are largely released beyond the bar due to the decreasing nonlinearity.

In the deepening region beyond the bar, a different behaviour for random and monochromatic waves is observed. For random waves the bound harmonics are released and the wave field can still be described as a superposition of statistically independent waves, without memory of the phase locks which existed over the bar. Unlike irregular waves, the harmonic components of monochromatic waves continue to interact in the protected area and the asymmetry parameters vary significantly as a result of the varying phase lags between the freely propagating component waves. The evolution of the wave spectrum behind submerged obstacles also affects the run-up on the beach. A second experimental campaign has been carried out to evaluate the wave run-up over a 1:20 impermeable slope in presence of the submerged bar. The observed run-up is better correlated to the incident wave characteristics for regular monochromatic waves and to the characteristics of the transmitted spectra for random waves. Indeed, for random waves the non-linear interactions induced by the submerged bar also generate long waves that affect the infragravity band swash. This does not occur for regular monochromatic waves where the first harmonic remains the main forcing of the run-up.

References

Ahrens, J. (1981). Irregular wave run-up on smooth slopes. Technical report, Coastal Engineering ResearchCentre Vol. CETA 81-17.

Archetti, R. and Brocchini, M. (2002). An integral swash zone model with friction: an experimental and numerical investigation. *Coastal Engineering*, 45(2):89–110.

Archetti, R. and Zanuttigh, B. (2010). Integrated monitoring of the hydro-morphodynamics of a beach protected by low crested detached breakwaters. *Coastal Engineering*, 57(10):879–891.

Armstrong, J. A., Bloembergen, N., Ducuing, J., and Pershan, P. S. (1962). Interactions between light waves in a nonlinear dielectric. *Phys. Rev.*, 127:1918–1939.

Battjes, J. (1974). Surf similarity. *Coastal Engineering Proceedings*, 1(14):26.

Beji, S. and Battjes, J. A. (1993). Experimental investigation of wave propagation over a bar. *Coast. Eng.*, 19:151–162.

Beji, S. and Battjes, J. A. (1994). Numerical simulation of nonlinear wave propagation over a bar. *Coast. Eng.*, 23:1–16.

Bertin, X., de Bakker, A., van Dongeren, A., Coco, G., André, G., Ardhuin, F., Bonneton, P., Bouchette, F., Castelle, B., Crawford, W. C., Davidson, M., Deen, M., Dodet, G., Guérin, T., Inch, K., Leckler, F., McCall, R., Muller, H., Olabarrieta, M., Roelvink, D., Ruessink, G., Sous, D., Stutzmann, É., and Tissier, M. (2018). Infragravity waves: From driving mechanisms to impacts. *Earth-Science Reviews*, 177:774–799.

Briganti, R., van der Meer, J., Buccino, M., and Calabrese, M. (2004). Wave transmission behind low-crested structures. In *Coastal Structures 2003*. American Society of Civil Engineers.

Byrne, R. J. (1969). Field occurrences of induced multiple gravity waves. *Journal of Geophysical Research*, 74(10):2590–2596.

Carevic, D., Loncar, G., and Prsic, M. (2013). Wave parameters after smooth submerged breakwater. *Coastal Engineering*, 79:32–41.

Ciardulli, F. (2009). *La Risposta Idraulica di Barriere Sommerse in Campo Non Lineare*. PhD thesis, Università degli Studi di Napoli "Federico II".

de Bakker, A. T. M., Herbers, T. H. C., Smit, P. B., Tissier, M. F. S., and Ruessink, B. G. (2015). Nonlinear infragravity–wave interactions on a gently sloping laboratory beach. *Journal of Physical Oceanography*, 45(2):589–605.

de Beer, A. (2017). The influence of incident waves on runup. Master's thesis, Delft University of Technology.

Elgar, S. and Guza, R. T. (1985a). Observations of bispectra of shoaling surface gravity waves. *J. Fluid Mech.*, 161:425–448.

Elgar, S. and Guza, R. T. (1985b). Shoaling gravity waves: comparisons between field observations, linear theory, and a nonlinear model. *Journal of Fluid Mechanics*, 158:47–70.

Elgar, S. and Guza, R. T. (1986). Nonlinear model predictions of bispectra of shoaling surface gravity waves. *Journal of Fluid Mechanics*, 167(-1):1.

Elgar, S., Guza, R. T., Raubenheimer, B., Herbers, T. H. C., and Gallagher, E. L. (1997). Spectral evolution of shoaling and breaking waves on a barred beach. *Journal of Geophysical Research: Oceans*, 102(C7):15797–15805.

Freilich, M. H. and Guza, R. T. (1984). Nonlinear effects on shoaling surface gravity waves. *Philos. Trans. R. Soc. London, Ser. A*, 311:1–41.

Goda, Y. (1967). Travelling secondary wave crests in wave channels. Technical report, Appendix to Rep. No. 13, Port and Harbour Research Institute, Ministry of Transport, Japan.

Goda, Y. (2010). *Random Seas and Design of Maritime Structures*. WORLD SCIENTIFIC.

Goda, Y., Okazaki, K., and Kagawa, M. (1999). Generation and evolution of harmonic wave components by abrupt depth changes. In *Proceedings of Coastal Structures '99*, pages 649–658, Balkema.

Goda, Y. and Suzuki, Y. (1976). Estimation of incident and reflected waves in random wave experiments. In *ASCE, Proc. 15th Coastal Engineering Conference*, pages 828–845, ASCE, New York.

Grue, J. (1992). Nonlinear water waves at a submerged obstacle or bottom topography. *Journal of Fluid Mechanics*, 244(-1):455.

Hansen, N.-E. O., Sand, S. E., Lundgren, H., Sorensen, T., and Gravesen, H. (1980). Correct reproduction of group-induced long waves. In *Coastal Engineering 1980*. American Society of Civil Engineers.

Hasselmann, K. (1962). On the non-linear energy transfer in a gravity wave spectrum, part i. general theory. *J. Fluid Mech.*, 12:481–500.

Hasselmann, K., Munk, W., and McDonald, G. (1963). Bispectra of ocean waves. In *Proceedings of the Symposium on Time Series Analysis*, pages 125–139, Wiley, New York.

Herbers, T.H.C., R. N. E. S. (2000). Spectral energy balance of breaking waves within the surf zone. *J. Phys. Oceanogr.*, (30):2723–2737.

Hughes, S. A. (2004). Estimation of wave run-up on smooth, impermeable slopes using the wave momentum flux parameter. *Coastal Engineering*, 51(11-12):1085–1104.

Hunt, I. A. (1959). Design of seawalls and breakwaters. *Journal of the Waterways and Harbors Division*, 85(3):123–152.

Kim, Y. C. and Powers, E. J. (1979). Digital bispectral analysis and its application to the non-linear wave interactions. *IEEE Trans. on Plasma Sc.*, 1:120–131.

Lamberti, A., Zanuttigh, B., and Martinelli, L. (2007). Wave overtopping and transmission: An interpretation of spectral change at low crested rubble-mound structures. In *Coastal Engineering 2006*. World Scientific Publishing Company.

Liberatore, G. and Petti, M. (1992). Wave transformations over a submerged bar: Experiments and theoretical interpretations. *Coast. Eng.*, pages 447–459.

Lin, C.-Y. and Huang, C.-J. (2004). Decomposition of incident and reflected higher harmonic waves using four wave gauges. *Coastal Engineering*, 51(5-6):395–406.

Longuet-Higgins, M. and Stewart, R. (1964). Radiation stresses in water waves: a physical discussion, with applications. *Deep Sea Research and Oceanographic Abstracts*, 11(4):529–562.

Longuet-Higgins, M. S. and Stewart, R. W. (1962). Radiation stress and mass transport in gravity waves, with application to 'surf beats'. *Journal of Fluid Mechanics*, 13(4):481–504.

Losada, I. J., Patterson, M. D., and Losada, M. A. (1997). Harmonic generation past a submerged porous step. *Coast. Eng.*, 31:281–304.

Mansard, E. P. and Funke, E. R. (1980). The measurement of incident and reflected spectra using a least squares method. In *ASCE, Proc. 17th Coastal Engineering Conference*, pages 154–172, ASCE, New York.

Mase, H. and Kirby, J. T. (1993). Hybrid frequency-domain KdV equation for random wave transformation. In *Coastal Engineering 1992*. American Society of Civil Engineers.

Massel, S. (1983). Harmonic generation by waves propagating over a submerged step. *Coastal Engineering*, 7:357–380.

Masson-Delmotte, V., Zhai, P., Pirani, A., Connors, S., Péan, C., Berger, S., Caud, N., Chen, Y., Goldfarb, L., Gomis, M., Huang, M., Leitzell, K., Lonnoy, E., Matthews, J., Maycock, T., Waterfield, T., Yelekçi, O., Yu, R., and Zhou, B. (2021). Ipcc, 2021: Climate change 2021: The physical science basis. contribution of working group i to the sixthassessment report of the intergovernmental panel on climate change. Technical report, Cambridge University Press. InPress.

Miche, M. (1944). Mouvements ondulatoires de la mer en profondeur constante ou décroissante. Technical report, Annales de Ponts et Chaussées, Paris.

Nielsen, P. and Hanslow, D. (1991). Wave runup distributions on natural beaches. *Journal of Coastal Research*, 7(4):1139–1152.

Norheim, C.A., H.-T. E. S. (1998). Nonlinear evolution of surface wave spectra on a beach. *J. Phys. Oceanogr.*, (28):1534–1551.

Peng, Z., Zou, Q., Reeve, D., and Wang, B. (2009). Parameterisation and transformation of wave asymmetries over a low-crested breakwater. *Coastal Engineering*, 56(11-12):1123–1132.

Peregrine, D. H. (1967). Long waves on a beach. *Journal of Fluid Mechanics*, 27(4):815–827.

Phillips, O. M. (1960). On the dynamics of unsteady gravity waves of finite amplitude. part 1. *J. Fluid Mech.*, 9:193–217.

Roelvink, D., Reniers, A., van Dongeren, A., van Thiel de Vries, J., McCall, R., and Lescinski, J. (2009). Modelling storm impacts on beaches, dunes and barrier islands. *Coastal Engineering*, 56(11-12):1133–1152.

Roelvink, D., Reniers, A., van Dongeren, A., vanThiel de Vries, J., Lescinski, J., and McCall, R. (2010). *Xbeach model description and manual.* Unesco-IHE Institute for WaterEducation, Deltares and Delft University of Technology.

Smit, P., Zijlema, M., and Stelling, G. (2013). Depth-induced wave breaking in a non-hydrostatic, near-shore wave model. *Coastal Engineering*, 76:1–16.

Stockdon, H., Thompson, D., Plant, N., and Long, J. (2014). Evaluation of wave runup predictions from numerical and parametric models. *Coastal Engineering*, 92:1–11.

Stockdon, H. F., Holman, R. A., Howd, P. A., and Sallenger, A. H. (2006). Empirical parameterization of setup, swash, and runup. *Coastal Engineering*, 53(7):573–588.

Symonds, G., Huntley, D. A., and Bowen, A. J. (1982). Two-dimensional surf beat: Long wave generation by a time-varying breakpoint. *Journal of Geophysical Research*, 87(C1):492.

van der Meer, J. W., Briganti, R., Zanuttigh, B., and Wang, B. (2005). Wave transmission and reflection at low-crested structures: Design formulae, oblique wave attack and spectral change. *Coastal Engineering*, 52(10-11):915–929.

van der Meer, J. W., Regeling, H. J., and de Waal, J. P. (2000). Wave transmission: spectral changes and its effects on run-up and overtopping. In *ASCE, Proc. 27th ICCE*, Sydney, Australia.

van Gent, M. R. A. (1999). Wave run-up and wave overtopping for double peaked wave energy spectra. Technical report, Delft Hydraulics Report H3351, Delft.

van Gent, M. R. A. (2001). Wave runup on dikes with shallow foreshores. *Journal of Waterway, Port, Coastal, and Ocean Engineering*, 127(5):254–262.

Vousdoukas, M. I., Wziatek, D., and Almeida, L. P. (2011). Coastal vulnerability assessment based on video wave run-up observations at a mesotidal, steep-sloped beach. *Ocean Dynamics*, 62(1):123–137.

Wassing, F. (1957). Model investigations of wave run-up on dikes carried out in the netherlands in the last 20 years. *Coastal Engineering Proceedings*, 1(6):42.

Zanuttigh, B. and Martinelli, L. (2008). Transmission of wave energy at permeable low crested structures. *Coastal Engineering*, 55(12):1135–1147.